Eindhoven University of Technology

MASTER

Comparative parameter studies of dynamic models for centrifugal compression systems

Mickers, R.W.

Award date:
2006

Link to publication

Disclaimer
This document contains a student thesis (bachelor's or master's), as authored by a student at Eindhoven University of Technology. Student theses are made available in the TU/e repository upon obtaining the required degree. The grade received is not published on the document as presented in the repository. The required complexity or quality of research of student theses may vary by program, and the required minimum study period may vary in duration.

General rights
Copyright and moral rights for the publications made accessible in the public portal are retained by the authors and/or other copyright owners and it is a condition of accessing publications that users recognise and abide by the legal requirements associated with these rights.

- Users may download and print one copy of any publication from the public portal for the purpose of private study or research.
- You may not further distribute the material or use it for any profit-making activity or commercial gain

Comparative parameter studies of dynamic models for centrifugal compression systems

R.W. Mickers

DCT 2006.02

Master's thesis

Coach: ir J. van Helvoirt

Supervisor: dr. ir. A.G. de Jager

Technische Universiteit Eindhoven
Department Mechanical Engineering
Dynamics and Control Technology Group

Eindhoven, Januari,2006

Abstract

The operating region of centrifugal compressors is limited by the aerodynamic flow instabilities rotation stall and surge. Both instabilities can cause damage to a compressor due to mechanical and thermal loads. This thesis starts with some introductory remarks about compressor types and compressor components. Furthermore the compressor map is elucidated and then the two compressor instabilities (i.e. rotating stall and surge) are explained as concepts with their own classifications.

In this thesis the focus is on compressor surge and more specifically on preventing surge by means of active surge control. Several surge control techniques from literature are discussed. The conclusion of this literature study is that for the design of active surge control strategies it is desirable to have an adequate model of the dynamic behavior of the compression system. The objective of this project was to investigate what model is most suitable for describing those dynamics of a centrifugal compression system that are relevant for active surge control.

A brief overview of available compressors models is given and four compressor models are then presented in more detail. The four compressor models of which the various assumptions, advantages and disadvantages are discussed are: the Greitzer model, the extended Greitzer model proposed by Meuleman and the models proposed by Spakovszky (Spakovszky I and Spakovszky II). Finally, a motivated choice is made to further investigation of the Greitzer model and the extended Greitzer model by Meuleman.

Subsequently, the analysis of the numerical models is divided into an analysis of the Greitzer model and an analysis of the extended Greitzer model. Both model analyses were initiated by an operation point analysis: the operating point is changed in order to observe eigenvalue changes of the linearized models. This operation point analysis is followed by an analysis of certain eigenvalue characteristics (stable/unstable, real/complex). This eigenvalue analysis is different for both compressor models: for the Greitzer model an analytical eigenvalue analysis is done whereas for the extended Greitzer model a numerical eigenvalue analysis is done. In order to observe the effect of model parameters on the eigenvalues, some model specific parameters (Greitzer: ratio A_c/L_c, extended Greitzer: γ) were changed. Finally, the normalized distance between zero(s) and pole(s) was investigated. On basis of the model assumptions and the normalized distances for the extended Greitzer model by Meuleman, it is concluded that the extended Greitzer model is not an improvement in compressor modeling in comparison to the Greitzer model.

In order to support the conclusions of the eigenvalue and parameter study, the Greitzer model is validated with measurement data from an experimental setup. The overall match of the Greitzer model with experimental data is good but also some remarkable differences were observed, in particular near and after instants of flow reversal. Despite these observed differences, the Greitzer model seems usable for describing the overall behavior of the compressor. Therefore, based on the results of all investigations, it is concluded that of the investigated models the Greitzer model is most suitable for describing the relevant dynamics of a centrifugal compressor system.

Nomenclature

Roman uppercase

Symbol	Description	Dimensions[1]	S.I. unit
$\mathbf{A}$	system matrix		
A	flow area	L^2	m^2
$\mathcal{AR}$	area-density ratio	–	–
$\mathbf{B}$	input matrix		
$\mathbf{C}$	output matrix		
C	constant [4]	–	–
C'	constant [4]	–	–
$\mathbf{D}$	direct feed-through matrix		
$H(s)$	transfer function in Laplace domain		
L	duct length	L	m
M	molar weight	Ψ	kg/mol
Ma	Mach number	–	–
N	compressor rotational speed	T^{-1}	rev/min
R	gas constant[2]	L^{2}T$^{-2}\Theta^{-1}$	J/(kg·K)
T	temperature	Θ	K
U	velocity	LT^{-1}	m/s
V	volume	L^3	m^3
Z	compressibility factor	–	–

Roman lowercase

Symbol	Description	Dimensions	S.I. unit
a	velocity of sound	LT^{-1}	m/s
c	constant	–	–
c_p	specific heat capacity at constant pressure	L^{2}T$^{-2}\Theta^{-1}$	J/(kg·K)
c_v	specific heat capacity at constant volume	L^{2}T$^{-2}\Theta^{-1}$	J/(kg·K)
d	diameter, distance	L	m
f	frequency	T^{-1}	Hz
h	height	L	m

---

[1] M = mass, L = length, T = time, Θ = Temperature

[2] Equal to the universal gas constant (8.3145 J/mol·K), divided by the molar weight M. Using the symbol R is a slight abuse of notation since this symbol is normally used to denote the universal gas constant.

Roman lowercase

Symbol	**Description**	**Dimensions**	**S.I. unit**
m	mass	M	kg
$\dot{m}$	mass flow	MT^{-1}	kg/s
p	pressure	$\mathrm{ML}^{-1}\mathrm{T}^{-2}$	Pa
s	Laplace variable		
u	valve opening		

Greek

Symbol	**Description**	**Dimensions**	**S.I. unit**
α	Stokes number ($\frac{h}{2}\sqrt{\frac{n}{\nu}}$)	–	–
α_r	αrelaxation determining τ (Appendix C)	–	–
γ	ratio of specific heats c_p/c_v	–	–
δ	boundary layer thickness	L	m
δ_s	steady boundary layer thickness	L	m
λ	eigenvalue	T^{-1}	rad/s
μ	dynamic viscosity	$\mathrm{ML}^{-1}\mathrm{T}^{-1}$	Pa·s
ν	kinematic viscosity μ/ρ	$\mathrm{L}^{2}\mathrm{T}^{-1}$	m^2/s
ξ	rotor blade row inertia	–	–
o	stator blade row inertia	–	–
ρ	density	ML^{-3}	$\mathrm{kg/m}^3$
τ	time constant	T	s
τ_w	wall shear stress	$\mathrm{ML}^{-1}\mathrm{T}^{-2}$	$\mathrm{kg/ms}^2$
ϕ	dimensionless mass flow	–	–
χ	difference between unsteady and the quasistatic wall shear stress (τ_w-$\tau_{w_{qs}}$)	$\mathrm{ML}^{-1}\mathrm{T}^{-2}$	$\mathrm{kg/ms}^2$
ψ	dimensionless pressure difference	–	–
ω_H	angular frequency Helmholtz resonator	T^{-1}	rad/s
Γ	partial derivative compressor curve to compressor mass flow	$\mathrm{L}^{-1}\mathrm{T}^{-1}$	Pa·s/s
Ξ	partial derivative total valve mass flow to plenum pressure	LT	kg/Pa·s

Subscripts

Symbol	**Description**
$_0$	equilibrium value
$_1$	suction
$_2$	discharge
$_a$	all
$_c$	compressor
$_{dif}$	diffuser
$_h$	hub
$_i$	test case numbers

imp	impeller
l	large throttle valve
$o.p.$	operating point
p	plenum
qs	quasistatic
s	small throttle valve
v	valve/throttle
t	tip

Superscripts

Symbol	**Description**
$*$	surge value

Operators

Symbol	**Definition**	**Description**
$\mathbf{a}$	vector	$(x, y, z) = \mathbf{i}x + \mathbf{j}y + \mathbf{k}z$
ϕ	scalar function	ϕ
$\frac{d\phi}{dt}$	time derivative	$\dot{\phi}$
$\frac{\partial\phi}{\partial x}$	partial derivative with respect to variable x	
$\lvert\lvert\mathbf{a}\rvert\rvert$	magnitude of vector	$\sqrt{x^2 + y^2 + z^2}$
$\Delta\phi$	difference	$\phi_2 - \phi_1$
$\bar{\phi}$	nondimensionalized parameter	
$\tilde{\phi}$	small deviation from equilibrium	$\phi - \phi_0$
ϕ'	adjusted variable	
$(\cdot)^{-1}$	inverse operator	
$(\cdot)^T$	transpose operator	
$\angle$	angle/phase	
$\Re(z)$	real part of z	$\Re(1 + 2i) = 1$
$\Im(z)$	imaginary part of z	$\Im(1 + 2i) = 2$

Acronym

Symbol	**Description**
LHP	Left Half of complex Plane
RHP	Right Half of complex Plane

Contents

Abstract i

Nomenclature iii

Contents vii

1 Introduction 1
- 1.1 Compressors 1
  - 1.1.1 Compressor map 3
- 1.2 Compressor instability 4
- 1.3 Surge control 6
  - 1.3.1 Models for control design 7
- 1.4 Thesis objective 8

2 Available models 9
- 2.1 Compressor models 9
- 2.2 Greitzer model 10
- 2.3 Extended Greitzer model 11
- 2.4 Models proposed by Spakovszky 13
- 2.5 Summary compressor models 15

3 Analysis of numerical models 17
- 3.1 Greitzer model and parameter experiments 17
  - 3.1.1 Greitzer model 17
  - 3.1.2 Greitzer operation point variation 19
  - 3.1.3 Greitzer analytical system pole analysis 22
  - 3.1.4 Greitzer parameter variations 28
  - 3.1.5 Greitzer normalized distance between pole and zero 31
  - 3.1.6 Conclusion Greitzer model 33
- 3.2 Extended Greitzer model and parameter experiments 35
  - 3.2.1 Extended Greitzer model 35
  - 3.2.2 Extended Greitzer operation point variation 36
  - 3.2.3 Extended Greitzer numerical system pole analysis 41
  - 3.2.4 Extended Greitzer model parameter variation 43
  - 3.2.5 Extended Greitzer normalized distance between pole and zero 48
  - 3.2.6 Conclusion extended Greitzer 51
- 3.3 Conclusion Greitzer versus extended Greitzer model 52

4 Model validation 53
- 4.1 Method of model validation 53
- 4.2 Validation data 53
  - 4.2.1 Simulation and experiment 1 54
  - 4.2.2 Simulation and experiment 2 56

4.2.3 Simulation and experiment 3 57
4.2.4 Simulation and experiment 4 58
4.2.5 Discussion of results 58
4.3 Conclusion model validation 59

5 Conclusions and Recommendations 61
5.1 Conclusions 61
5.2 Recommendations 61

Bibliography 63

Appendices 65

A Tables 67
A.1 Greitzer operation point variation table 67
A.2 Meuleman operation point variation table 68
A.3 Greitzer parameter variations; ratio $\frac{A_c}{L_c}$ 68
A.4 Greitzer parameter variations; V_1 69
A.5 Greitzer parameter variations; V_2 69
A.6 Meuleman γ variation 69

B Compressor curve and experimental setup 71
B.1 Compressor curve 71
B.2 Throttle line 71
B.3 Experimental setup 72

C Meuleman parameters C' and τ 75

D Meuleman normalized distances 77

E Model validation 81
E.1 Simulation and experiment 2 81
E.2 Simulation and experiment 3 83
E.3 Simulation and experiment 4 84

Samenvatting 87

Dankwoord 89

Chapter 1

Introduction

The stable operation range of the centrifugal compressor can be extended by stabilization of surge. Therefore dynamical compressor models are required, in order to investigate phenomena and design/test means for stabilization. An introductory review of compressor types is given in Section 1.1 followed by an elucidation of the compressor map. The phenomena stall and surge are discussed in Section 1.2 where also the existing classifications of both phenomena are described. Remarks about the existing surge control techniques can be found in Section 1.3, that is followed by a few considerations about the controller design, Section 1.3.1. Finally, in Section 1.4 the objective of this thesis is formulated.

1.1 Compressors

Compressor are used for pressurization of media (i.e. fluids/gasses), examples are gas turbines or turbochargers. When in the following chapters of this thesis a medium is mentioned, it will mean that this is a gas. Two types of compressors will be discussed in this section; the axial compressor and the centrifugal compressor. Compression in these machines is based on the conversion of kinetic energy into potential energy. The compression is achieved through acceleration of a medium to a higher velocity and the subsequent deceleration through diffusion to transform the accumulated kinetic energy into potential energy (pressure).

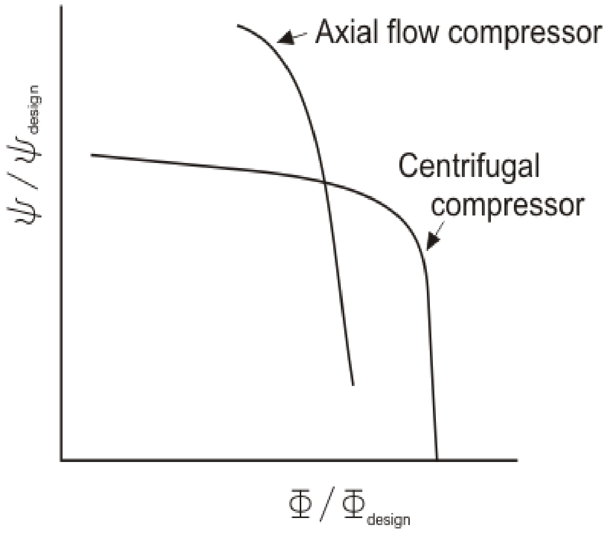

Figure 1.1: Centrifugal compressor versus axial compressor

A comparison between both compressor types is depicted in Figure 1.1 where the normalized pressure rise versus the normalized mass flow plotted. Normalization is done with respect to the nominal design values, this results in different slopes in the design points of the compressor curves.

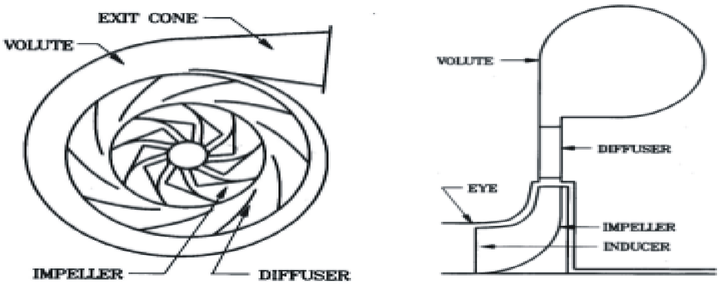

Figure 1.2: Centrifugal compressor [20].

When the compressor components are looked at in more detail, the differences between the two types become more evident. For a centrifugal compressor the main components are:

- *Inducer*: The function of the inducer is to avoid or migrate cavitation (if the medium is not a gas) on the impeller blades by raising the pressure of the approaching medium and also to give the medium a pre-swirl.
- *Impeller*: A rotating row of blades that together with a *diffuser* form a stage, depending on the compressor design this pair can be repeated to obtain a multistage compressor.
- *Diffuser*: The diffuser is for recovering kinetic energy from a medium before it enters the volute. The diffusion proces can be assisted by stationary vanes (i.e. diffuser vanes), otherwise an annular diffuser(vaneless diffuser) is applied.
- *Volute/Collector*: The volute is used to smoothly collect the flow from the diffuser exit and lead it into the discharge pipe. An alternative for the volute is a simple collector that is similar to a volute but one that has a uniform cross-sectional area in its circumferential direction.

For an axial compressor, the structure can be characterized [22] by:

- *Inlet Guide Vane (IGV)*: For the development of a swirl (tangential) velocity for the first stage an inlet guide vane (IGV) can be applied.
- *Rotor*: A rotating row of blades and a downstream stationary row (stator), which together form a stage. Similar to the centrifugal compressor, this stage can be repeated in order to obtain a multistage compressor.
- *Outlet Guide Vane (OGV)*: Optionally for the axial compressor an outlet guide vane (OGV) can be applied that typically follows after the last stage. In this component any residual swirl velocity is removed and the associated kinetic energy is converted into static pressure. Both IGV and OGV can be omitted in the compressor structure.

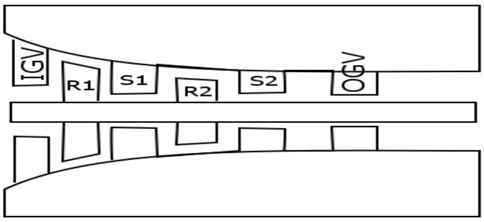

Figure 1.3: Axial compressor, [20].

1.1.1 Compressor map

A compressor map graphically shows the relation between the rotational speed, the pressure rise across the compressor and the mass flow through the compressor. The compressor map shows the quasistatic compressor characteristics at different rotational speeds, the load or throttle line(s) and usually the surge/stall and the stonewall lines, see Figure 1.4 for an example. When the rotational speed is increased the compressor characteristic is shifted into the direction of the arrow.

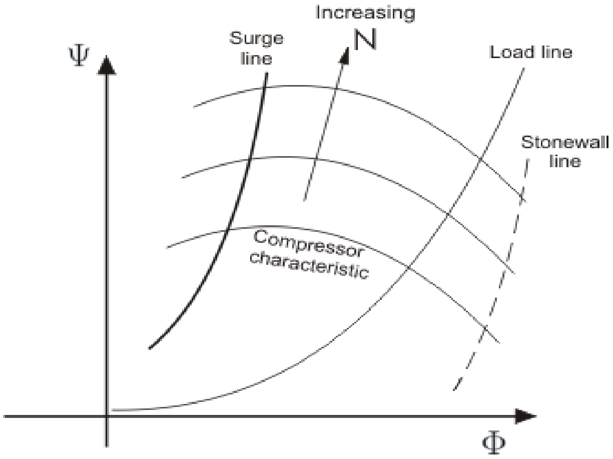

Figure 1.4: Compressor map.

The steady-state operating point(s) of the compression system are represented by the intersection between the compressor characteristic and the load line. For the unique definition of a compressor operation point, four parameters are required [9], namely:

1. **Pressure rise** Ψ
   Dimensionless total-to-static pressure rise according to:

$$\frac{\Delta p}{\frac{1}{2}\rho U_t^2}$$

   in which ρ is density and U_t is the impeller tip speed.

2. **Mass flow** ϕ

$$\frac{\dot{m}}{\rho A U_t}$$

   in which $\dot{m}$ is the mass flow, U_t is the impeller tip speed, ρ is the density and A is the impeller inlet area.

3. **Compressor speed** N.

4. An additional parameter such as **efficiency** or **temperature rise** is needed.

The mass flow operating range of the compressor is limited towards the high mass flow by a condition called choked flow. This is marked in the compressor map by the so called stonewall line. At this point the medium in the machine approaches the velocity of sound (Mach 1) and the polytropic efficiency drops rapidly. For low mass flows the restriction for the stable operating range is the *surge* (or *stall*) *line*. We will discuss the phenomena surge and rotating stall in more detail below.

1.2 Compressor instability

Rotating stall and Surge

During operation, a compressor can enter an unstable flow regime (at low flow) where two phenomena can occur: *surge* and/or *rotating stall.*

Rotating stall is a two dimensional, local instability in which one or more local regions of stagnant flow, i.e. stall cells, rotate around the circumference of the compressor. The classification for rotating stall is as follows:

- Part-span/full-span stall, referring to the size of the stalled region in terms of annulus height [8], as shown in the figure below.

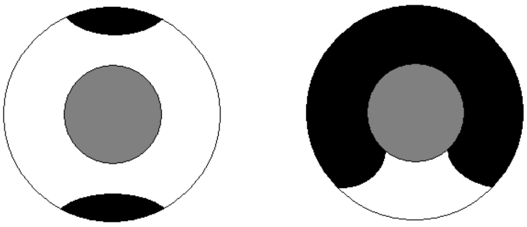

Figure 1.5: Part-span (left), and full-span stall (right).

- Short/Long length scale stall cells, describing the circumferential extent of the cell when it first forms [15]. Low and higher order rotating stall modes can be distinguished simultaneously, both classifications are based on the wavelength of spatial harmonics that describe the stall pattern.

In the left part of Figure 1.6 a stall pattern is displayed in the compressor map. At operation point 1, the compressor is operating unstalled. When the mass flow is decreased, for example by closing a throttle, the operation point shifts towards the point 2 where stall almost occurs. When the operation point shifts to point 3 on the stalled characteristic, the compressor efficiency drop.

When the compressor is stalled (point 3) and the system is required to operate in an unstalled operation point (e.g. point 5), the stall recovery traject is not the obvious traject 3-5. Instead hysteresis is present and the traject 3-4 is followed by increasing the mass flow to point 4. While the mass flow is increased to reach (point 5), the operation point shifts to point 1 and stall is eliminated. In order to reach (point 5) the mass flow has to be decreased again. Sometimes the compressor can't be recovered by increasing mass flow and the machine has

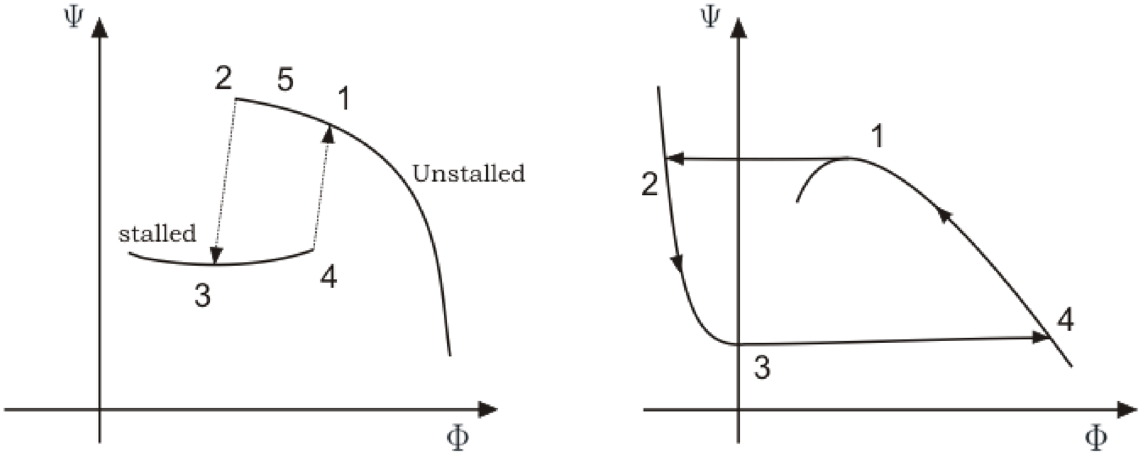

Figure 1.6: Stall and Surge patterns.

to make a full stop followed by a restart. If rotating stall occurs in isolated parts of the machine, it may cause acoustic resonances [5] and thus vibrations in the blades.

Surge is a large amplitude oscillation of the total annulus average flow through the compressor and can be classified as follows [5]:

- *Mild surge*: The frequency of the oscillation is of the order of the Helmholtz frequency and pressure fluctuations are small. No flow reversal occurs.
- *Classic surge*: Lower frequency and larger oscillations than mild surge. No flow reversal occurs.
- *Modified surge*: The entire annulus flow fluctuates in axial direction and rotating stall is superimposed, so the flow is unsteady and nonaxisymmetric. It is a mix of rotating stall and classic surge phenomena.
- *Deep surge*: A more severe version of classic surge, where even flow reversal is possible. This is an unsteady but axisymmetric limit cycle for the flow.

The fundamental difference between stall and surge is that surge is a system instability and stall is a local instability. Subsequently some physical differences between stall and surge are characterized by their frequencies and amplitudes. The rotating stall cells usually have a constant rotational speed between 20 and 80% of the rotor speed whereas the frequencies of surge oscillations are typically over an order of magnitude less than those associated with the passage of the rotating cells. Furthermore at decreasing throttle position the surge frequency increases [9]. The load line is altered and because of that the operation point shifts, on the compressor characteristic, to the left. Due to the shifted operation point, the plenum filling time increases during a surge cycle and because of that the surge frequency increases. The oscillation amplitudes of rotating stall however are smaller compared to the amplitudes of surge oscillations. Surge is a system characteristic that leads to loads, both thermal as well as mechanical, that can cause damage to the system and therefore must be suppressed.

On the right side of Figure 1.6 a deep surge cycle is plotted. The initiation at point 1 of surge causes the flow to become instable, after which a transition occurs to point 2 at which the flow becomes negative. The negative flow characteristic is followed to (approximately) zero flow at point 3, then the flow rapidly changes towards the normal characteristic at point 4. From point 4 the flow decreases along the characteristic towards point 1 and the cycle is repeated again until intervention.

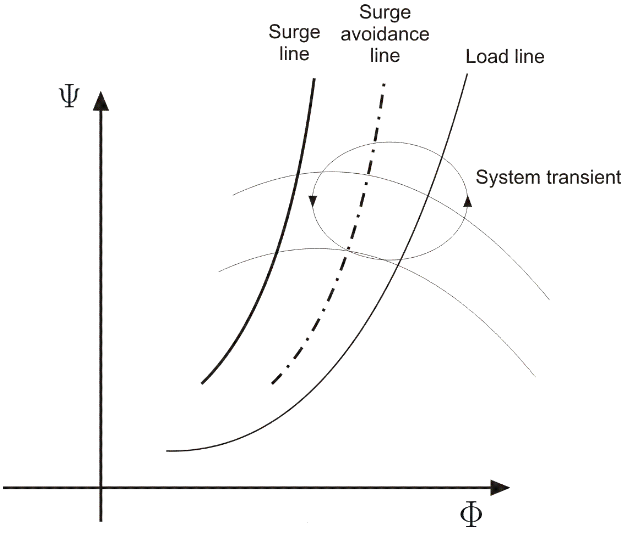

Figure 1.7: Surge avoidance.

Usually surge is prevented through defining a surge avoidance line, see Figure 1.7, this is a line defined as a percentage of the surge line (towards the stable operating region) such that a safety margin is created. When a system transient crosses the surge avoidance line and starts developing towards the surge line, an intervention takes place so that the system transient is brought back to the stable region. Surge avoidance control can be done by controlling the following variables:

- Increasing/decreasing N; this can be done by controlling motor torque through voltage or fuel.
- Increasing/decreasing ϕ or ψ; this can be done by recirculation or bleeding of the medium.

In Figure 1.8 the surge avoidance techniques *bleed off* and *recirculation* are illustrated. The difference between these techniques is that during bleed off compressed air is discharged from the system whereas during recirculation the compressed air is feed back into the system.

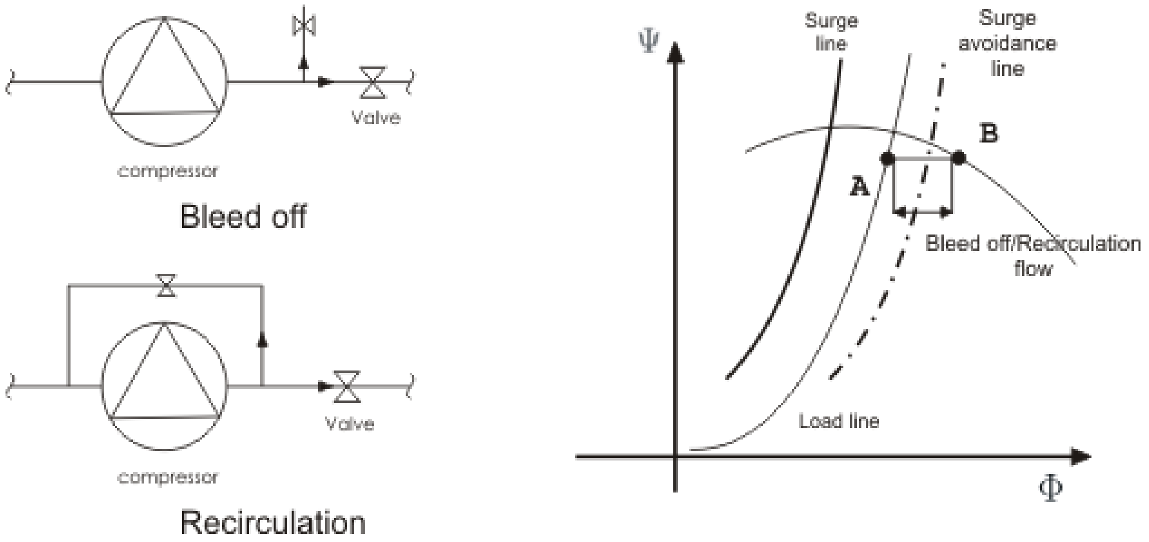

Figure 1.8: Surge avoidance techniques, [20].

The mass flow related to the bleed off or recirculation is indicated by the line A-B. Both techniques, bleed off and recirculation, are techniques that reduce the efficiency. During bleed off the potential energy (compressed air) is discharged from the system and during recirculation the potential energy is dissipated in the valve parallel to the compressor.
When hazardous or expensive gasses are used as a medium, it is preferable the use the recirculation principle, in other cases (e.g. medium is gas) the bleed off principle can be used.

1.3 Surge control

Surge avoidance is a technique to prevent surge from occurring but it limits the compressor efficiency. Therefore, another interesting/promising to prevent the occurrence of surge is active surge control. Active surge control means that controllers are used for stabilization of operating points by feedback of pressure perturbations. Probably one of the first investigations was documenten in [14] and in the following years this field evolved. Up to now, numerous studies have been conducted of rotating stall and surge behavior in compressors, both theoretical as experimental. The pioneering work in modeling surge and rotating stall in a compressor was done in [2] and [14]. The axial compressor model was expanded in [8] and some time later in [10]. The field of active surge control (feedback control) can be divided in, amongst others, Robust control, Adaptive control and Nonlinear control. The three former mentioned control techniques are looked at in the literature study, it must be remarked that other control techniques exist but not looked at in this thesis. First several feedback control studies will be discussed.

Table 1.1: Overview surge control

Reference		Compressor[a]	Sensor	Actuator	Control
Gysling *et al*	(1991)	C	Plenum Pressure	Movable wall	Structural feedback
Ffowcs Williams *et al*	(1993)	C	Plenum pressure	Loudspeaker	Proportional feedback
Arnulfi *et al*	(1999)	Cm	Plenum pressure	Movable wall	Structural feedback
	(1999)	Cm	Plenum pressure	Movable wall	Proportional feedback
Willems	(2000)	C	Plenum pressure	Plenum bleed valve	Proportional feedback
Gravdahl *et al*	(2002)	C	Mass flow rotational speed	Electrical motor	Proportional feedback
Billoud *et al*	(1991)	A	Plenum pressure	Loudspeaker	Adaptive control
van der Wal *et al*	(1997)	C	Various	Various	Robust control
Der-Cheng Liaw *et al*	(2002)	A	Plenum	Close coupled valve	Nonlinear control

---

[a] Compressor: C=Centrifugal, A=Axial, m=multistage (default is single stage)

The feedback control can be divided in passive and active control. An example of a passive control is the movable wall from [7] that was implemented in the plenum. This control approach provided a means for absorbing the unsteady energy perturbations produced by the compressor. In [13] a comparison performance study between a passive surge control (movable wall) and active surge control was presented. One of the active surge control studies was discussed in [16], where a surge controller is presented that measured and controlled any nonaxisymmetric disturbances in the flow. As can be seen in Table 1.1 this was done by applying proportional feedback through a loudspeaker in the plenum. A different kind of study is the work discussed in [25] that followed the active linear control path but investigated the optimal set of actuator(s) and sensor(s) in a robust controller. In [19] a active surge control is discussed that uses an electrical drive (actuator) and employing feedback from mass flow and rotational speed, resulting in a globally exponentially stable controller. In [9] a new control strategy was developed: *one-sided control*. In this strategy, the bleed valve is closed in the equilibrium point and, to stabilize the system in this operating point, it can only be operated to one side (opening of the valve).

One of the alternative control techniques, an adaptive controller for the control of combustion instabilities and self-sustained pressure oscillations in a flow-exited cavity is discussed in [12]. Subsequently, another alternative technique is the nonlinear control discussed in [6]. Herein a robust control for surge behavior is used but the authors did not implemented the controller in an experimental setup. The study of a nonlinear controller is, amongst others, presented in [1] that discussed a controller (globally stabilizing switching) but again did not implemented the controller on an experimental setup.

The alternative control techniques show that, apart from linear control, several alternative techniques/strategies exist and active research is continuing in these fields.

1.3.1 Models for control design

From the studies, presented in Section 1.3, it becomes clear that an adequate model (accurate, correct structure end relevant dynamics covered) for the dynamic behavior of a compressor is needed. An adequate model can be related to the results obtained in combination with a controller i.e. to what extend the performance of a controller is reached.

The models used in the studies (as discussed in Section 1.3) are non-linear models; the compressor models describe non-linear phenomena (i.e. compressor characteristic, etc.). The whole compressor is essentially a non-linear system, but for control design the non-linearities can be overcome by linearizing the model. Linearization is usually applied because of the common understanding of linear control. This linearization implies and requires that the model and controllers for this model are only valid for small perturbations around an equilibrium point.

Questions about the available control techniques in combination with the stabilization of surge arise from the discussed studies, and can be related to the compressor model:

1. What is the influence of the model structure on the controller design?
2. Which dynamic behavior of the compressor system is relevant for the controller design?

An important factor limiting the controller design is inadequate modeling of the system and its components. By assumptions and simplifications of the system, dynamics can be neglected or added to the model, making it difficult to design a stabilizing controller with the resulting model.

Furthermore the performances of a controller is determined by the choice for type and location of sensor(s) and actuator(s). The chosen sensor(s) and sensor locations can also lead to different approaches in control, because for example the chosen sensor(s) can add extra dynamics to the system or the sensor/actuator pair(s) can have strong mutual coupling. This is illustrated in [17] where the performance of different sensors in combination with different actuators was discussed. The authors of [25] investigated what actuators and sensors gave the best guaranteed surge stabilization according to their performance criterium.

The question about which dynamic behavior of the compressor system is relevant for the controller design is discussed in this paragraph. The relevant dynamic behavior of the compression system could contain the valve dynamics or the compressor characteristic. Due to practical limitations the compressor characteristic can only be measured in the stable operation area, the characteristic in the unstable area is usually approximated by a third order cubic equation as described in Appendix B. During computer simulations the dynamics of a valve are not always modeled, this means that the valve has an infinitely fast response. When the controller is implemented in the experimental setup, the system could become unstable because the valve has (unmodeled) dynamics.

1.4 Thesis objective

From the former discussion it becomes clear that for the design of active surge control strategies it is desirable to have an adequate model of the dynamic behavior of the compression system. The objective of this project is to investigate what model is most suitable for describing those dynamics of a centrifugal compression system that are relevant for active surge control.

To provide an answer to that questions, this thesis addresses the following topics. Firstly, an overview of available models for compressor dynamics is given in Chapter 2 and the selection of four promising models is discussed. These models are the so-called Greitzer model the extended Greitzer model as proposed by Meuleman and two models suggested by Spakovszky. Secondly, the benefits and advantages of these four models are discussed and a second selection is made.

For the two remaining models, the Greitzer model and the extended Greitzer model (as proposed by Meuleman) a detailed parameter study is performed of which the results are presented in Chapter 3. Special attention is paid to the effect of the added dynamics in the model by Meuleman in comparison with the Greitzer model.

To further support these conclusions from the parameter study, the Greitzer model is validated with measurement data from an experimental centrifugal compressor test rig. The results thereof are presented and discussed in Chapter 4. Finally, overall conclusions and recommendations for further research are given in Chapter 5.

Chapter 2

Available models

In this chapter a brief overview of some available compressor models is given. Furthermore, a founded choice is made for the closer investigation of four specific compressor models. These models are the basic models developed by Greitzer, the extended Greitzer model proposed by Meuleman and the two models suggested by Spakovszky. For each of these models the main model assumptions are given, followed by the model structure and a list of advantages and disadvantages. Finally, the findings are summarized and conclusions are given.

2.1 Compressor models

In the literature several compressor models exist for axial or centrifugal compressors, each with its own assumptions. These models can be categorized on basis of flow assumptions, inclusions of rotational speed, compressor type and the covered instability, see for example [9].

Table 2.1: Available compressor models

Model	Flow description	ΔN^a	Type ^{b}	Instab.^{c}
Greitzer (1976a)	1D Incompressible	-	A	S
Hansen *et al.* (1982)	1D Incompressible	-	C	S
Fink *et al.* (1992)	1D Incompressible	+	C	S
Gravdahl and Egeland (1997c)	1D Incompressible	+	C	S
Macdougal and Elder (1983)	1D Incompressible	-	A C	S
Elder and Gill (1985)	1D Incompressible	-	C	S
Botros (1994)	1D Incompressible	+	A C	S
Badmus *et al.* (1995a)	Quasi-1D Incompressible	-	A C	S
Willems (2000)	1D Incompressible	-	A	S
Meuleman (2002)	1D Incompressible	-	A	S
Moore and Greitzer (1986)	2D Incompressible	-	A	SR
Gravdahl and Egeland (1997b)	2D Incompressible	+	A	SR
Feulner *et al.*	1D/2D Compressible	-	A	SR
Ishii and Kashiwabara (1996)	2D Compressible	-	A	SR
Spakovszky I (2001)	2D Incompressible	-	A	SR
Spakovszky II (2001)	2D Incompressible	-	A	Sh

---

[a] +: speed variations included, -: speed variations not included
[b] A: Axial compressor, C: Centrifugal compressor
[c] S: Surge, R: Rotating stall, SH: Spatial harmonics

Four compressor models are investigated more closely in this thesis; the Greitzer model, the extended Greitzer model proposed by Meuleman and the Spakovszky models. One of the most used models is the Greitzer model developed by Greitzer [8]. This well-known model is usually referred to as the Greitzer model. It is evident that for comprehension of other models, the Greitzer model has to be studied. The model proposed by Meuleman is chosen because this model is an extended Greitzer model; the Greitzer model is extended with extra dynamics that physically interpret the transient system behavior. So in order to see what possibilities this extension generates for the model Meuleman this model has to be investigated. The first Spakovszky model is based on the Moore-Greitzer model but the second Spakovszky model is novel model approach, where the separate compressor parts are modeled separately. These submodels can be linked together in this modular approach. It is useful to investigate the Spakovszky I model in order to understand the second Spakovszky model and the used novel model approach. The other models in Table 2.1 were not included the following analysis because the four chosen models seemed to be most promising.

2.2 Greitzer model

The Greitzer model for the dynamic behavior of a compressor was proposed in [8]. The model is based on the analogy between surge oscillations and a Helmholtz resonator, an idea first suggested in [14]. The model equations in full dimensions are:

$$\frac{d\dot{m}_c}{dt} = \frac{A_c}{L_c}\left(\Delta p_c(\dot{m}_c) - \Delta p\right) \tag{2.1}$$

$$\frac{dp_p}{dt} = \frac{a_2^2}{V_2}\left(\dot{m}_c - \dot{m}_v(\Delta p, u_v)\right) \tag{2.2}$$

with

$$\begin{aligned} \Delta p &= p_p - p_1 \\ a_p^2 &= \gamma_p Z_p R T_{p0} \end{aligned}$$

Some remarks about the compressor curve $\Delta p_c(\dot{m}_c)$, the control valve with opening u_s (system input) and the throttle/load line $\dot{m}_v(\Delta p, u_s)$ are given in Appendix B.

Note that the above equations are usually nondimensionalized by scaling mass flow with $\rho U A_c$, pressure with $\frac{1}{2}\rho U^2$ and time with $\omega_H = a\sqrt{\frac{A_c}{V_p L_c}}$. However, in this thesis only the full dimensional equations will be used because they are more suitable for the investigations presented in subsequent chapters.

Assumptions

The flow in the ducts is assumed to be one-dimensional in this model. Pressure rises relative to ambient pressure and inlet Mach numbers are all assumed to be sufficiently low to neglect compressibility effects and hence the flow in the ducts is considered to be incompressible. For the plenum it is assumed that pressure is uniformly distributed, gas velocity is negligible and that the compression process is isentropic. Furthermore, it is assumed that the compressor and throttle respond quasi-static to changes in mass flow and that the influence of rotor speed variations in small. The overall temperature ratio $\frac{T_2}{T_1}$ is assumed to be near unity. No restrictions are placed on for example the amplitude of the oscillations in pressure rise and mass flow, compared to the steady state values of these quantities.

Model structure

The model components are as follows:

- *Ducts*: In the inlet duct as well as in the outlet duct a one dimensional, incompressible flow is assumed.
- *Compressor*: The compressor and its ducting are replaced by an actuator disk. In this actuator disk it is assumed that the impeller and diffuser can be represented by a disk with an infinitesimal thickness across which the mass flow is continuous, but pressure changes can be discontinuous.
- *Plenum*: It is assumed that the mass flow herein is negligible and that the compression process in the plenum is polytropic.

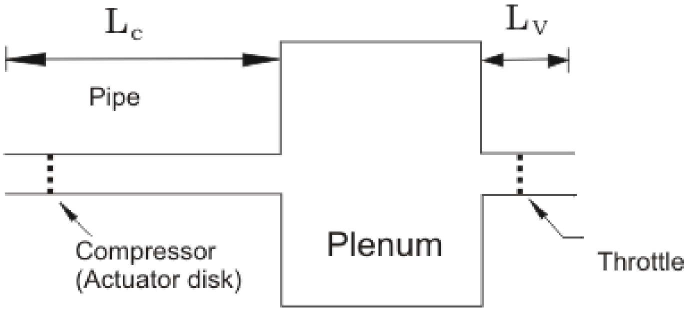

Figure 2.1: The Greitzer model.

Advantages
The Greitzer model is a straightforward model of two coupled nonlinear differential equations. The nonlinearities are introduced by the compressor and throttle characteristics. The advantage of the Greitzer model is that the model is relatively simple because the flow is assumed to be one-dimensional. Yet, with this model it is possible to investigate the dynamic behavior of a compressor during surge.

Disadvantages
A disadvantage of the Greitzer model is the fact that the model is over-parameterized. This could be solved by using the nondimensional model instead. Furthermore, the model uses the assumption that the flow in the ducts is incompressible. Finally, all the inertial effects in the compression system are lumped onto a single compressor duct and as a result tuning of the model becomes necessary. This tuning makes it difficult to give a physical interpretation of the tuned model parameter(s).

A logical extension of the Greitzer model is the model developed by Meuleman, as discussed in the following section.

2.3 Extended Greitzer model

A logical extension of the Greitzer model was suggested by Meuleman [4]. The resulting extended model consists of the following equations:

$$\frac{d\dot{m}_c}{dt} = \frac{A_c}{L_c}\left(\Delta p_c(\dot{m}_c) - \Delta p\right) + \chi \tag{2.3}$$

$$\frac{dp_p}{dt} = \frac{a_p^2}{V_p}\left(\dot{m}_c - \dot{m}_v(\Delta p, u_v)\right) \tag{2.4}$$

$$\tau\frac{d\chi}{dt} = C'\frac{h^2 A_c}{\nu L_c}\frac{\partial \Delta p_c(\dot{m}_c)}{\partial \dot{m}_c}\frac{d\dot{m}_c}{dt} - \chi \tag{2.5}$$

with

$$\begin{aligned}\Delta p &= p_p - p_1\\ a_p^2 &= \gamma_p Z_p R T_{p0}\end{aligned}$$

Assumptions

In the extended Greitzer model the same general assumptions were used as by Greitzer. The first assumptions are that the flow in the ducts is one-dimensional and incompressible. The compression process in the plenum is assumed to be isentropic, the plenum pressure is uniformly distributed and the medium velocity in the plenum is negligible. Furthermore, a quasi-static behavior of compressor and throttle is assumed and the influence of rotor speed variations is assumed to be small. The overall temperature ratio for the system is assumed to be near unity.

Model structure

The schematic representation of the model as suggested by Meuleman is identical to that of the Greitzer model in Figure 2.2. The Greitzer model is expanded with an extra state equation that accounts for the difference between the exact wall shear stress and the quasi-static wall shear stress. These extra dynamics are included to modify the quasi-static compressor characteristic during unsteady behavior of the compressor. The model components are as follows:

- *Ducts*: In the inlet duct as well as in the outlet duct a one dimensional, incompressible flow is assumed.
- *Compressor*: The compressor and its ducting are replaced by an actuator disk. In this actuator disk it is assumed that the impeller and diffuser can be represented by a disk with an infinitesimal thickness across which the mass flow is continuous, but pressure changes can be discontinuous.
- *Plenum*: It is assumed that the mass flow herein is negligible and that the compression process in the plenum is polytropic.
- *Throttle*: The length of the throttle duct is assumed to be small enough to neglect inertial effects. Therefore, the throttle is replaced by a static relation between the mass flow through and pressure difference over the throttle.

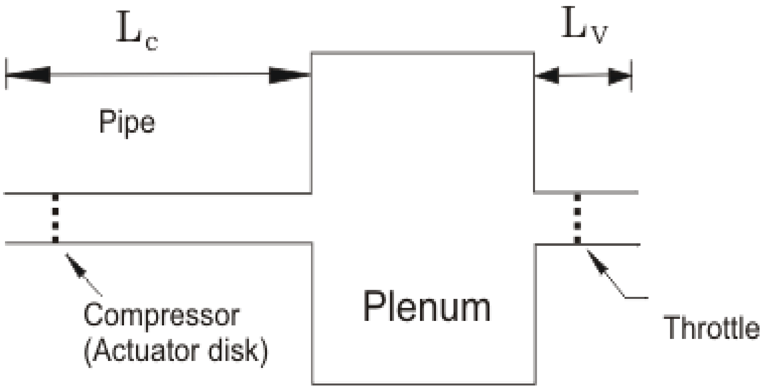

Figure 2.2: Extended Greitzer model by Meuleman.

The quasistatic model uses a compressor characteristic that is approximated by a cubic polynomial (Appendix B), this characteristic is validated for the stable operation region by experimental data. In the extended Greitzer model several time constants (τ_c=compressor passage response time, τ_T=idem for throttle, etc.) are used to account for the response times in these compressor components.

Advantages
According to [4] the dynamics of a compression system are captured well by the model. Simulations and experiments indicated that the addition of the extra state equation resulted in a better prediction of surge frequency, maximum pressure rise and the pressurization phase during a surge cycle in comparison with the Greitzer model. Despite the additional state equation, the extended Greitzer model is still a simple and straightforward dynamic model of a low order.

Disadvantages
The same disadvantages as were mentioned for the Greitzer model hold for the extended Greitzer model. Furthermore, while the extra state equation eliminates the need to tune the compressor duct length it has introduced two additional parameters that are difficult to determine for actual compression systems.

2.4 Models proposed by Spakovszky

In this section the models that were developed by Spakovszky [26] will be discussed, starting with the general assumptions that were applied in both models. Subsequently, two models proposed by Spakovszky (Model I and Model II) are described separately its advantages and disadvantages.

General assumptions

A common assumption for both models is the fact that the Reynolds number effects are ignored (for example boundary layers) and the effects of viscosity and heat transfer outside the blade rows are neglected. The flow through radial segments is assumed to be two-dimensional where both the flow in radial and circumferential direction are taken into account. Finally the blade rows are modeled as actuator disks with unsteady inertia and loss terms.

Assumptions: model I proposed by Spakovszky

The first model by Spakovszky is a model that is based on the Moore-Greitzer model, therefore the flow in the ducts is assumed to be two-dimensional and inviscid. The plenum compression process is assumed to be isentropical and the Moore-Greitzer model is expanded by unsteady blade passage fluid inertia of the impellers, ξ, and stators, o. These terms account for the unsteady blade row inertia; a part of the compressor pressure rise is devoted to accelerate the fluid in the blade passages.

Model structure: model I proposed by Spakovszky

The model structure uses a semi-actuator disk for both the compressor and the throttle. The model structure that is used in this Spakovszky model is similar to the Moore-Greitzer model.

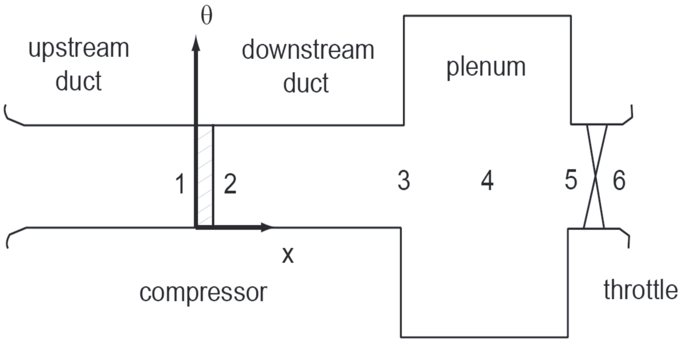

Figure 2.3: model I proposed by Spakovszky.

Advantages: model I proposed by Spakovszky
The model consists of separate equation for each component that describe two-dimensional flow and the compressor instabilities surge and rotating stall.

Disadvantages: model I proposed by Spakovszky
This model is limited to one actuator disk or multiple directly coupled actuator disks only, bounded by an upstream and a downstream duct. The compact formulation is not appropriate for modeling blade rows or compressors that are separated by ducts or inter blade-row-gaps. Furthermore the two-dimensional mass flow yields measurement problems.

Assumptions: model II proposed by Spakovszky

Because of the modeling in the second model proposed by Spakovszky, the assumptions for the different compressor system components are given separately:

- Axial duct: Incompressible flow is assumed to be inviscid.
- Radial space: A two-dimensional, unsteady linearized swirling flow is assumed.
- Impeller blade row assumptions:
  - Unsteady deviation effects for upstream and downstream flow conditions are neglected;
  - The exit flow angle is independent of inlet conditions;
  - Ideal flow in up-, and down-stream ducts are assumed;
  - Total pressure rise across the blade row is assumed to be isentropic;
  - Slip (for backsweep angles $< 45°$) and changes in area and density are taken into account. Slip is accounted for by considering the vorticity, the area and density changes are accounted by the impeller area-density ratio ($\mathcal{AR}_{imp} = \frac{\rho_2 A_2}{\rho_1 A_1}$, in which the subscript 1 is the impeller inlet and 2 is the impeller outlet).
- Diffuser;
  - Radial vaned diffuser: Changes in area and density and diffuser geometry are taken into account, included by the area-density ratio ($\mathcal{AR}_{dif} = \frac{\rho_2 A_2}{\rho_1 A_1}$, with subscript 1 for the impeller inlet and 2 for the impeller outlet);
  - Radial vaned diffuser: A diffuser time lag is assumed to be proportional to the convection time through the diffuser passage;
  - Radial vaneless diffuser: By assuming a inviscid and two-dimensional flow the mean background flow can be represented by a free vortex flow.
- Boundary conditions:
  - Infinite length ducts is assumed so that some inlet and outlet boundary conditions can be set to zero.
  - A downstream plenum.

Model structure: model II proposed by Spakovszky

The model structure for the second model proposed by Spakovszky is the same as for the first model regarding the included components. The difference between the two Spakovszky models is the fact that at the second model a modular approach was developed wherein each system component is modeled by a so called *transition matrix* that can be linked to any other system component.

Advantages: model II proposed by Spakovszky

An advantage of this approach is that each component has its own transmission matrix and these transmission matrices can be coupled in order to create a system. This is a very flexible modeling approach that is applicable to a wide variety of systems.

Disadvantages: model II proposed by Spakovszky

Compared to the other model proposed by Spakovszky or the previous models, the second model proposed by Spakovszky is difficult to solve numerically because of its solution methods (the contour plot method and the shot-gun method [26]). Another important disadvantage is the fact that some model parameters are difficult to measure.

All specific models are considered now, this leads to the conclusion.

2.5 Summary compressor models

In this section the results are summarized of the comparison between the four treated compressor models. Based on this discussion two models were selected for further investigation.

The Greitzer model is a low order nonlinear model that predicts the compressor behavior during transients and surge. Due to the lumping approach the compressor duct length must be tuned. Firstly, this tuning requires that pressure measurements during surge are available. Furthermore, the tuning makes a physical interpretation of the model parameter(s) difficult.

The Greitzer model is extended by Meuleman with an additional dynamic equation to account for the unsteady compressor behavior during transients. This extra state equation provides a correction term based on the difference between the exact wall shear stress and the quasi-static wall shear stress. The extended Greitzer model also predicts the compressor behavior during transients and surge. According to [4] the extended Greitzer model gives better results than the original Greitzer model.

In contrast to the one-dimensional Greitzer and extended Greitzer models, the first model proposed by Spakovszky describes the two-dimensional flow, similar to the model in [10]. Since it is difficult to measure mass flows, additional measurement and identification problems to set all model parameters are expected when mass flow must be measured in two dimensions.

The second model proposed by Spakovszky is a novel compressor modeling approach in which the main components (impeller, diffuser, e.g.) are modeled as separate modules. Again, flows are considered to be two-dimensional in this model. Furthermore, this model heavily focusses on the modeling of the compressor geometry. Different common compressor parameters (number of impeller blades, slip factor, impeller blade exit angle, e.g.) are taken into account to make the model generally applicable to different compressor configurations. However, the values of some model parameters are difficult to obtain with reasonable accuracy.

In selecting two compressor models for further investigation, both model accuracy (i.e. good agreement between predicted and measured dynamics) and the complexity of the model. From literature it became clear that the four investigated models all provide a reasonable accurate prediction of the compressor dynamics. However, since the two models proposed by Spakovszky both describe two-dimensional flows they are inevitably more complex than the one-dimensional Greitzer and extended Greitzer models. Although a two-dimensional model is required to study rotating stall, the added complexity is weighted stronger than the added prediction capabilities for studying the essentially one-dimensional phenomenon of surge. Therefore, in the remainder of this thesis we will focus on the one-dimensional (extended) Greitzer models.

Chapter 3

Analysis of numerical models

In order to investigate what compressor model is more suitable for predicting compressor behavior, in this chapter a comparison between the Greitzer compressor model and the extended Greitzer model proposed by Meuleman. The models are investigated separately by parameter studies (operation point analysis, model parameter analysis, analytical/numerical system pole analysis and normalized distance analysis). Conclusions are given for each model separately and this chapter is ended with overall conclusions.

3.1 Greitzer model and parameter experiments

In this section the Greitzer model is discussed, starting with its linearization in a operating point, followed by an analysis where the operating point is changed in order to observe eigenvalue changes. In addition to this, a analytical eigenvalue analysis is performed in order to check the (in)stability region. For the physical interpretation of model parameters, a parameter analysis is conducted. Finally the normalized distance between zero and poles is investigated.

3.1.1 Greitzer model

Because the experimental setup is a closed loop system (see Appendix B), the Greitzer model is somewhat altered in comparison to the open loop model described in Section 2.2. Therefore, the Greitzer equations for the closed loop compression system (Figure 3.1,[24]) are used.

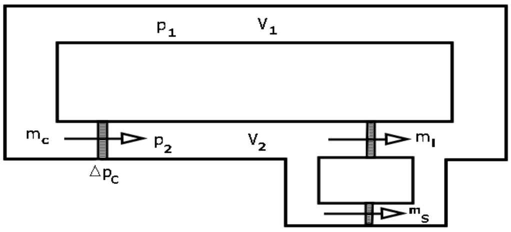

Figure 3.1: Compressor model

The Greitzer model differential equations as given below are the full dimensionalized equations as described in [24];

$$\frac{d\dot{m}_c}{dt} = \frac{A_c}{L_c}\{\Delta p_c(\dot{m}_c) + \Delta p\} \tag{3.1}$$

$$\frac{d\Delta p}{dt} = F_{lin}\{\dot{m}_c - \dot{m}_v(\Delta p, u_v)\} \tag{3.2}$$

with:

$$\begin{aligned} \Delta p &= p_2 - p_1 \\ \dot{m}_v(\Delta p, u_v) &= \dot{m}_l(\Delta p, u_l) + \dot{m}_s(\Delta p, u_s) \\ F_{lin} &= \frac{\gamma_1 Z_1 R T_{10}}{V_1} + \frac{\gamma_2 Z_2 R T_{20}}{V_2} \end{aligned}$$

Equations (3.1) and (3.2) are linearized around an operation point ($\dot{m}_{c,o.p.}, \Delta p_{c,o.p.}, u_{l,o.p.}, u_{s,o.p.}$). The closed loop system is rewritten in a state space manner to equations (3.3) and (3.4).

$$\dot{\underline{\tilde{\mathbf{x}}}} = \mathbf{A} \cdot \underline{\tilde{\mathbf{x}}} + \mathbf{B} \cdot \underline{\tilde{u}} \tag{3.3}$$

$$\underline{\tilde{\mathbf{y}}} = \mathbf{C} \cdot \underline{\tilde{\mathbf{x}}} + \mathbf{D} \cdot \underline{\tilde{u}} \tag{3.4}$$

The state vector is defined as $\mathbf{x} = \begin{bmatrix} \dot{m}_c & \Delta p \end{bmatrix}^T$ therefore the Greitzer closed loop system matrix equal to:

$$\tilde{\mathbf{x}} = \begin{bmatrix} \dot{m}_c \\ \Delta p \end{bmatrix}_{o.p.} \qquad \tilde{\mathbf{u}} = \begin{bmatrix} u \end{bmatrix}_{o.p.}$$

$$\mathbf{A} = \begin{bmatrix} \frac{A_c}{L_c}\frac{\partial \Delta p_c(\dot{m}_c)}{\partial x_1} & -\frac{A_c}{L_c} \\ F_{lin} & -F_{lin}\frac{\partial \dot{m}_v(\Delta p, u_v)}{\partial x_2} \end{bmatrix}_{\mathbf{x}=\mathbf{x}_{o.p.}} \qquad \mathbf{C} = \begin{bmatrix} 1 & 0 \\ 0 & 1 \end{bmatrix}_{\mathbf{x}=\mathbf{x}_{o.p.}}$$

$$\mathbf{B} = \begin{bmatrix} 0 \\ -F_{lin}\frac{\partial \Delta p_v}{\partial u} \end{bmatrix}_{\mathbf{x}=\mathbf{x}_{o.p.}} \qquad \mathbf{D} = \begin{bmatrix} 0 \\ 0 \end{bmatrix}_{\mathbf{x}=\mathbf{x}_{o.p.}}$$

A remark must be made about the output matrix **C**; for simulation purposes it is assumed that all states are available as outputs, though in practice it is difficult to measure a mass flow. In order to investigate changes of the **A**-matrix eigenvalues, the operation point ($\dot{m}_{c,o.p.}, \Delta p_{c,o.p.}, u_{l,o.p.}, u_{s,o.p.}$) is changed. This is done by multiplying the surge flow, $\dot{m}_c^*$ (measure on experimental setup), with a parameter, Fqs_i, for which applies:

$$Fqs \in \{0.88, 0.89, \ldots, 1.28, 1.29, 1.30, 1.40, \ldots, 2.50, 2.60\}$$

With this parameter variation a percentage of surge flow is obtained per test case:

$$\dot{m}_{c,i} = Fqs_i \cdot \dot{m}_c^*, \quad i \in \{1, 2, \ldots, 55, 56\}$$

The operation points can be seen on the compressor curve as shown in Figure 3.2.

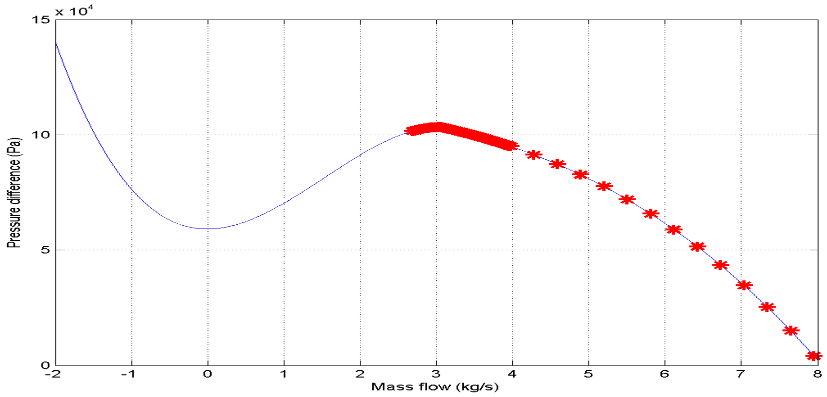

Figure 3.2: Fqs variation and compressor curve.

We now continue with a discussion on system pole changes at different operation points.

3.1.2 Greitzer operation point variation

The operation points are varied in order to see changes in system pole locations, this has to be clear in order to know the distinction between the stable and unstable operation area.

The system is linearized in an operation point and then the eigenvalues of the system matrix are computed. The real parts of the separate eigenvalues are presented in Figure 3.3 for selected test cases. The test cases are defined in Table A.1 in Appendix A. Not all test cases are presented in this figure because of the intelligibility of the figure. This principle in maintained in the rest of the thesis.

The first twelve test cases ($Fqs \in \{0.88, \ldots, 0.99\}$) show a positive real part for the both eigenvalues, marking the unstable operation region. The stable region starts at the 13th test case, where $Fqs \geq 1$ and where the real parts of the eigenvalues are negative. Figure 3.4 shows the evolution of the imaginary parts of the mass flow tests for the eigenvalues.

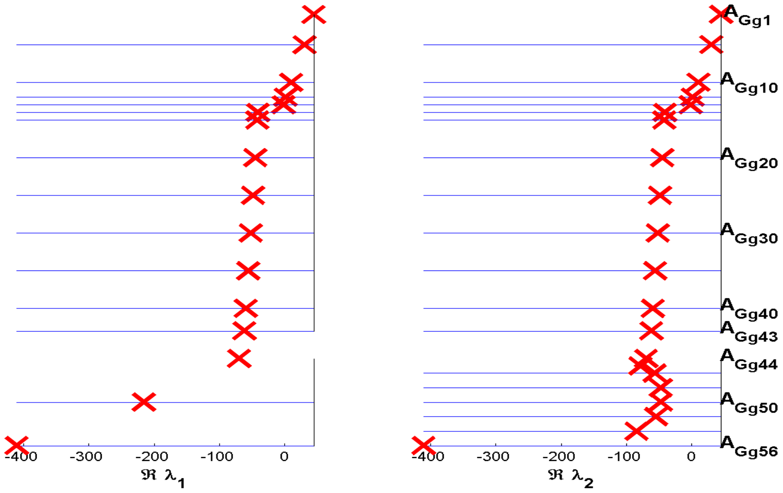

Figure 3.3: Real part Greitzer system poles for Fqs variation.

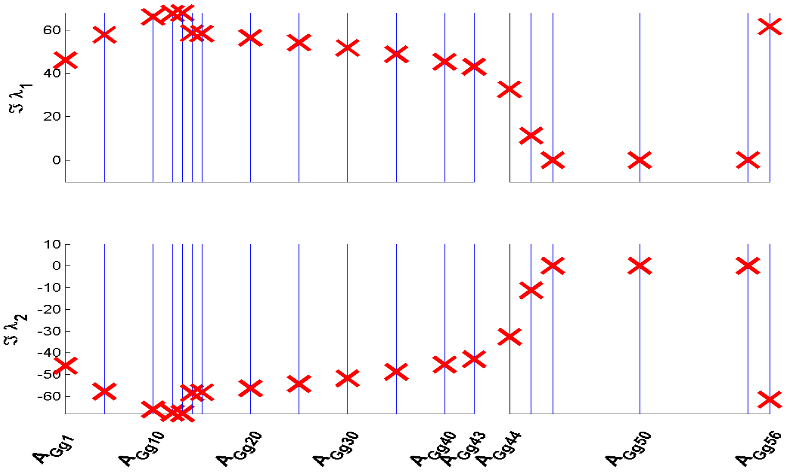

Figure 3.4: Imaginary part Greitzer system poles for Fqs variation.

When the information of Figure 3.3 and Figure 3.4 is combined the equilibrium of the linearized system is according to [23]:

- An *unstable focus* for $Fqs < 1$.
- A *stable focus* for $1 \geq Fqs \leq 1.60$ and for $Fqs = 2.60$.
- A *stable node* for $1.60 > Fqs \leq 2.50$.

The eigenvalues thus determine the path of the linearized system response around the operation point. A remark can be made about the linkage of the eigenvalues to the compressor system; λ_1 is the eigenvalue that represents flow reversal (the transition from $\dot{m}_c > 0$ to $\dot{m}_c < 0$ (and vice versa)) and λ_2 is the eigenvalue representing the filling and emptying of the plenum. When both real and imaginary parts are plotted in the complex plane for different test cases Figure 3.5 is obtained.

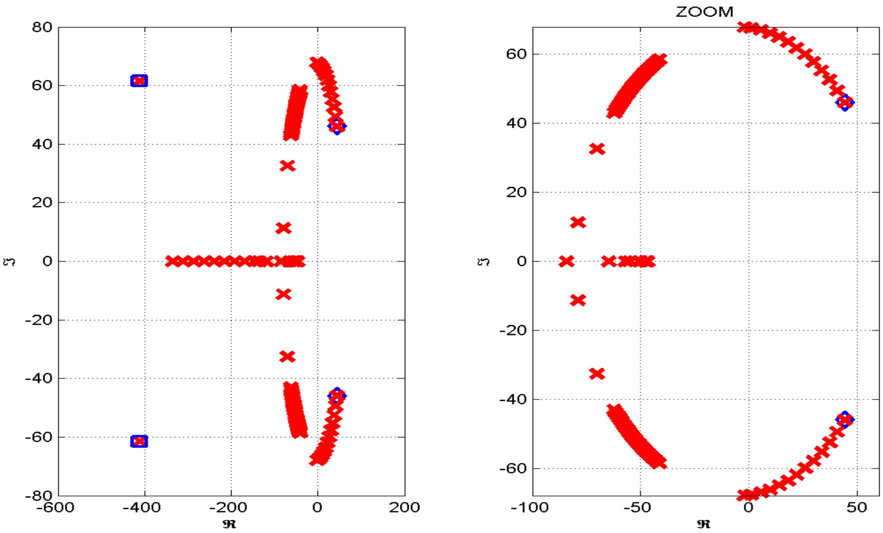

Figure 3.5: Eigenvalues Greitzer for Fqs variation (first; diamond marker, last; square marker).

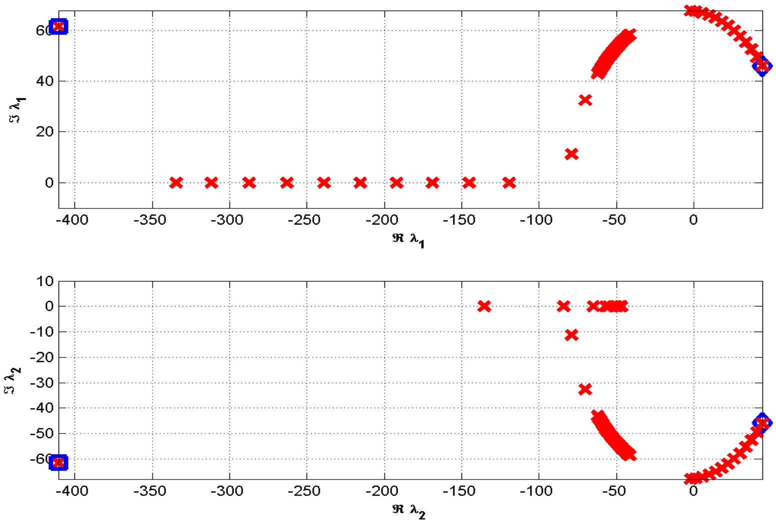

Figure 3.6: Separate eigenvalues Greitzer for Fqs variation.

In Figure 3.5 can be seen that both eigenvalues develop from the RHP into the LHP where a branchpoint, this is point where eigenvalues transfer from complex conjugate to strictly real or vice versa. From this branchpoint λ_1 develops further into the LHP whereas λ_2 initially starts shifting towards the RHP. Eventually at higher mass flows, λ_2 starts developing back into the LHP.

In Figure 3.6 the eigenvalues are plotted separately, here is shown that the two eigenvalues start as complex poles in the unstable region and for increasing mass flow these poles develop towards each other. From the eigenvalues for all test cases it can be seen that for very high mass flow i.e. $Fqs = 2.60$, the eigenvalues become complex conjugated again. Because these high mass flows are not encountered in the tests done on experimental setup, this complex conjugated pair is not investigated in the analytical eigenvalues analysis.

The next step is the description of the zero evolution, the model's transfer functions are acquired by:

$$H(s) = \mathbf{C}(s\mathbf{I} - \mathbf{A})^{-1}\mathbf{B} + \mathbf{D} \tag{3.5}$$

Take for example the first stable test case ($Fqs = 1.01$), and its corresponding linearized system matrices ((A),(B),(C) and (D)). The transfer functions are:

$$H_{11} = \frac{12.67}{s^2 + 82.83s + 5143} \tag{3.6}$$

$$H_{12} = \frac{-1230s + 9.358e004}{s^2 + 82.83s + 5143} \tag{3.7}$$

The first transfer function, H_{11}, is the transfer function from the input, position of the small (control) valve, to the first output i.e. compressor mass flow. H_{12} is therefore the transfer function from input to the plenum pressure. The Bode plots for the corresponding transfer functions are given in Figure 3.7.

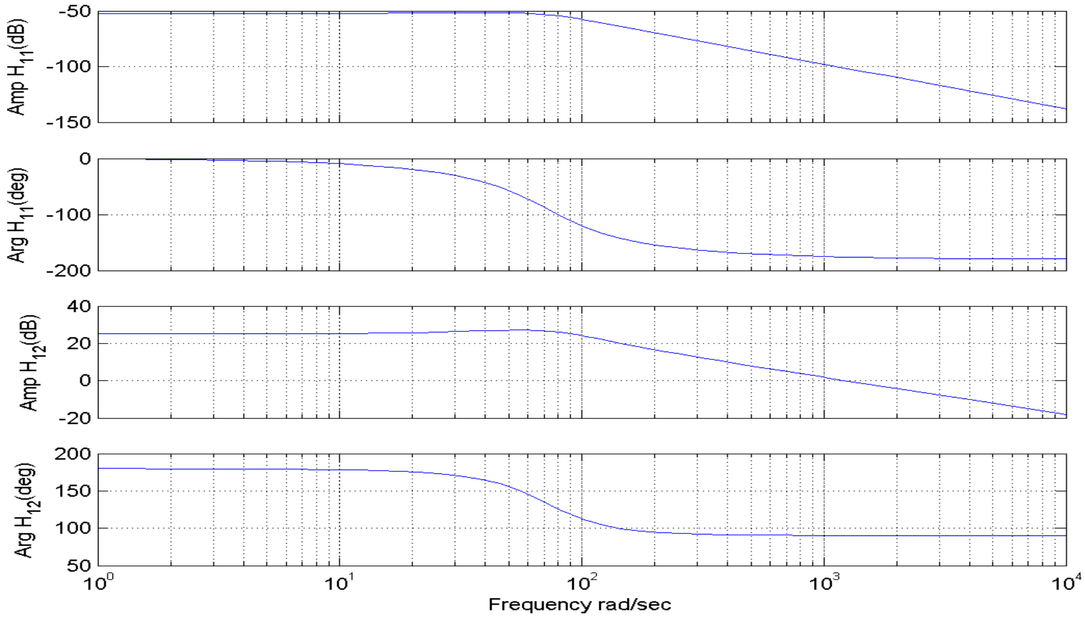

Figure 3.7: Bode plots of H_{11} and H_{12}.

The upper two subfigures in Figure 3.7 are the Bode plot from transfer function H_{11}, the lower two subfigures are the Bode plot from transfer function H_{12}. The Bode plot from transfer function H_{12} shows a resonance peak around 8(Hz). It can also be seen that the linearized system still has some phase margin, see Bode plot of transfer function H_{12}.

The zeros for all test cases are plotted in Figure 3.8. In this figure it can be seen that test case 1 till 13 ($Fqs = 0.88 - 1$) produce a nonminimum phase system, so when the mass flow is increased the zeros shift from the RHP towards the LHP.

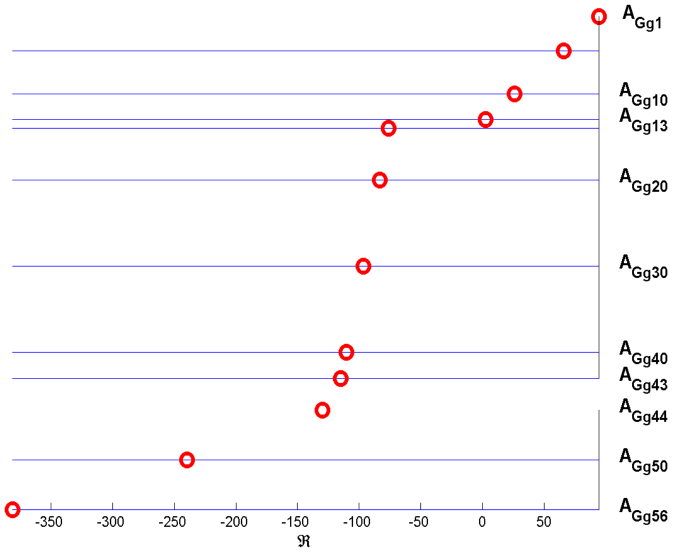

Figure 3.8: Zeros Greitzer from transfer function H_{12}

The evolution of Greitzer eigenvalues and zeros for different mass flows have been mapped; the eigenvalues are unstable from testcase 1 till 12 ($Fqs = 0.88 - 0.99$) and the zeros produce a nonminimum phase system for test case 1 to 13 ($Fqs = 0.88 - 1$). Furthermore it is clear how the root loci for this model evolve at increasing mass flow. We will now discuss analysis of the analytical Greitzer eigenvalues in the next subsection.

3.1.3 Greitzer analytical system pole analysis

The goal of this analysis is to formulate boundary conditions for analytical system poles per set of operation point(s).

Recalling the system matrix of the Greitzer model as below and rewriting it for notational simplicity as:

$$\mathbf{A} = \begin{bmatrix} \frac{A_c}{L_c}\frac{\partial \Delta p_c(\dot{m}_c)}{\partial \dot{m}_c} & -\frac{A_c}{L_c} \\ \beta & -\beta \cdot \frac{\partial \dot{m}_v(\Delta p, u_v)}{\partial p_p} \end{bmatrix}_{\mathbf{x}=\mathbf{x}_{o.p.}} \Leftrightarrow \begin{bmatrix} \frac{A_c}{L_c}\Gamma & -\frac{A_c}{L_c} \\ \beta & -\beta \cdot \Xi \end{bmatrix}_{\mathbf{x}=\mathbf{x}_{o.p.}} \tag{3.8}$$

with

$$\begin{aligned} \Gamma &= \frac{\partial \Delta p_c(\dot{m}_c)}{\partial \dot{m}_c} \\ \beta &= \frac{\gamma_1 Z_1 R T_{10}}{V_1} + \frac{\gamma_2 Z_2 R T_{20}}{V_2} \\ \Xi &= \frac{\partial \dot{m}_v(\Delta p, u_v)}{\partial \Delta p} \end{aligned}$$

The characteristic equation of matrix $\mathbf{A}$ (obtained by $\det(s\mathbf{I} - \mathbf{A})$) is equal to:

$$s^2 + (\beta\Xi - \frac{A_c}{L_c}\Gamma)s + (1 - \Gamma\Xi)\frac{A_c\beta}{L_c} = 0$$

In order to acquire the roots of this equation the ABC-formula is applied, which gives the eigenvalue solutions:

$$\begin{aligned} s_{1,2} &= -\frac{\beta\Xi}{2} + \frac{A_c\Gamma}{2L_c} \pm \frac{1}{2}\sqrt{(\beta\Xi - \frac{A_c}{L_c}\Gamma)^2 - (1 - \Xi\Gamma)4\frac{A_c\beta}{L_c}} \\ &= -\frac{\beta\Xi}{2} + \frac{A_c\Gamma}{2L_c} \pm \frac{1}{2}\sqrt{\beta^2\Xi^2 + 2\frac{A_c\Gamma\beta\Xi}{L_c} + \frac{A_c^2}{L_c^2}\Gamma^2 - 4\frac{A_c\beta}{L_c})} \\ &= -\frac{\beta\Xi}{2} + \frac{A_c\Gamma}{2L_c} \pm \frac{1}{2}\sqrt{(\beta\Xi + \frac{A_c}{L_c}\Gamma)^2 - 4\frac{A_c\beta}{L_c}} \end{aligned} \tag{3.9}$$

It can be seen that the term $4\frac{A_c\beta}{L_c}$ is numerically small compared to $(\beta\Xi + \frac{A_c}{L_c}\Gamma)^2$. This can be reasoned by the comparison of the values for compressor curve slope (Γ) and/or the valve slope (Ξ) compared to the compressor parameter values for A_c, L_c, β. The values for the slope are of an order higher than the values of the compressor parameter.

With the pole solution from (3.9) boundary conditions will be investigated in order to divide the operating region in regions where the system poles are stable/unstable or real/complex.

We start with the conditions that apply for the region where the poles are not complex. These conditions are marked in Figure 3.5 by the branchpoint in the LHP, where λ_1 moves away from λ_2. The solution for the poles becomes:

$$\begin{aligned} s_{1,2} &= -\frac{\beta\Xi}{2} + \frac{A_c\Gamma}{2L_c} \pm \frac{(\beta\Xi + \frac{A_c}{L_c}\Gamma)}{2} \\ & s_1 = \frac{A_c\Gamma}{L_c} \quad \wedge \quad s_2 = -\beta\Xi \end{aligned}$$

Parameter cases

The whole operational area of the compressor can roughly be divided into two subareas, the stable and unstable area. Furthermore, two special cases are added. these parameter cases will be investigated analytically:

① $\Gamma < 0 \quad \wedge \quad \Xi > 0 \quad \Rightarrow$ Stable operating region.

② $\Gamma > 0 \quad \wedge \quad \Xi > 0 \quad \Rightarrow$ Unstable operating region.

③ Transfer complex/real solution.

④ Transfer unstable/stable solution.

In Figure 3.9 an overview of parameter case data in combination with the compressor model is given. Operation points are varied by adjusting the valve curves. One curve is drawn for the stable operation region and one for the unstable region.
A remark can be made for all parameter cases: A_c, L_c, β and Ξ represent parameters that are always positive. Furthermore the valve curve slope, Ξ, is also positive but, the slope of the compressor curve, Γ, can be both negative as positive. In the remainder of this subsection we will discuss the outcomes of the solutions for the mentioned cases.

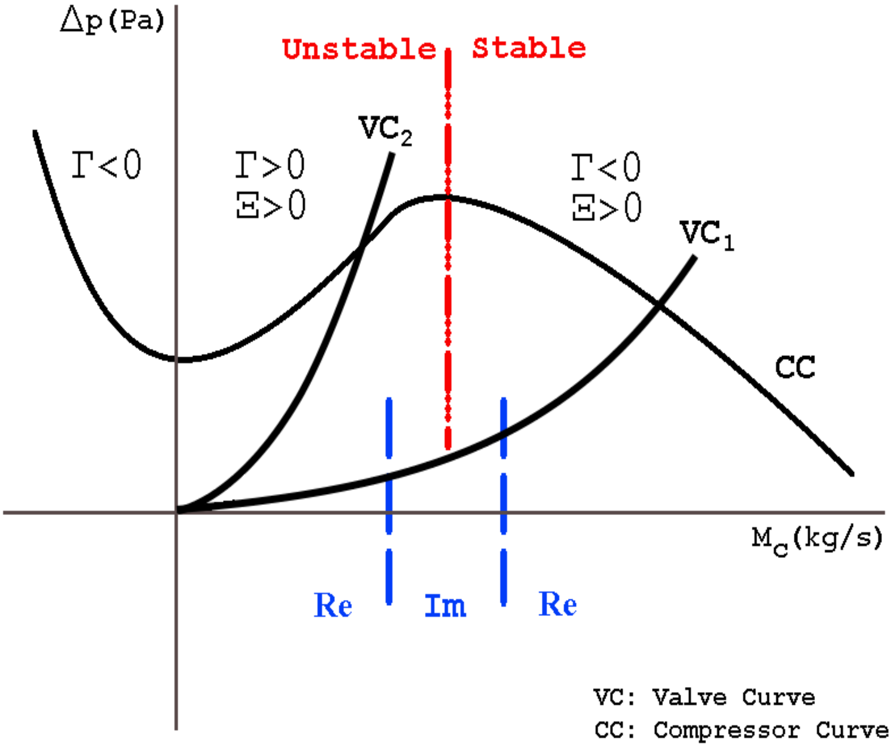

Figure 3.9: Parameter cases.

① Parameter case 1 $(\Gamma < 0 \wedge \Xi > 0)$

Taking the first parameter case into account and recalling the system matrix and poles of the system matrix:

$$
\begin{aligned}
\mathbf{A} &= \begin{bmatrix} \frac{A_c}{L_c}\Gamma & -\frac{A_c}{L_c} \\ \beta & -\beta \cdot \Xi \end{bmatrix}_{\mathbf{x}=\mathbf{x}_{o.p.}} \\
s_{1,2} &= -\frac{\beta\Xi}{2} + \frac{A_c\Gamma}{2L_c} \pm \frac{1}{2}\sqrt{(\beta\Xi + \frac{A_c}{L_c}\Gamma)^2 - 4\frac{A_c\beta}{L_c}}
\end{aligned}
$$

The subarea of the operating range that satisfies this condition is marked in Figure 3.9. Conditions for this area are derived below.

(a). When the following condition applies:

$$(\beta\Xi - \frac{A_c}{L_c}\Gamma)^2 < (1 - \Xi\Gamma)4\frac{A_c\beta}{L_c} \tag{3.10}$$

the system poles are complex, this is indicated in Figure 3.9 and in Figure 3.10 by the area enclosed by the two lower dashed vertical lines and marked as.

(b). When condition (a). is not satisfied and additionally the following condition holds:

$$\frac{A_c\Gamma}{L_c} - \beta\Xi < -\sqrt{(\beta\Xi - \frac{A_c}{L_c}\Gamma)^2 - 4\frac{A_c\beta}{L_c}} \tag{3.11}$$

the system poles are strictly real and stable. This area is indicated in Figure 3.9 and Figure 3.12 by the gray area.

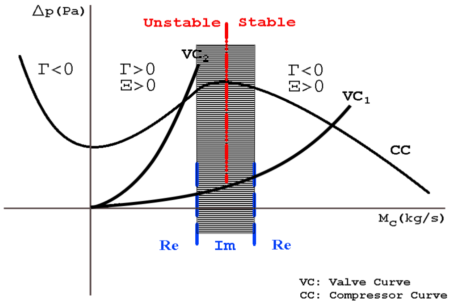
Δp (Pa)
Unstable
Stable
Γ<0
Γ>0
Ξ>0
VC₂
Γ<0
Ξ>0
VC₁
CC
M_C (kg/s)
Re
Im
Re
VC: Valve Curve
CC: Compressor Curve

Figure 3.10: Region of operating range with complex poles (where $\Im(s) \neq 0$)

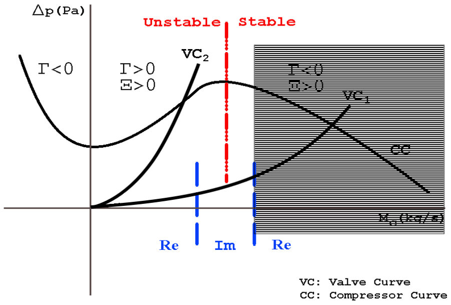
Δp (Pa)
Unstable
Stable
Γ<0
Γ>0
Ξ>0
VC₂
Γ<0
Ξ>0
VC₁
CC
M_C (kg/s)
Re
Im
Re
VC: Valve Curve
CC: Compressor Curve

Figure 3.11: Region of operating range with strictly real stable poles

(c). When condition (a). is satisfied and additionally the following condition applies:

$$\frac{A_c \Gamma}{L_c} > \beta \Xi \tag{3.12}$$

the system poles are strictly complex and stable. This area is indicated in Figure 3.9 and Figure 3.13 by the gray area.

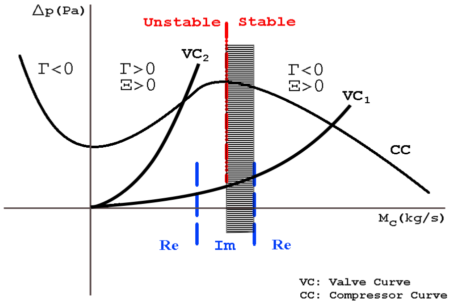
Δp (Pa)
Unstable
Stable
Γ<0
Γ>0
Ξ>0
VC₂
Γ<0
Ξ>0
VC₁
CC
M_C (kg/s)
Re
Im
Re
VC: Valve Curve
CC: Compressor Curve

Figure 3.12: Region of operating range with complex stable poles (where $\Im(s) \neq 0$)

② Parameter case 2 ($\Gamma > 0 \wedge \Xi > 0$)

Taking the second parameter case into account marked in Figure 3.9 by the unstable area, the conditions for this area are derived below.

(d). When condition (a). is satisfied and additionally the following condition holds:

$$\frac{A_c \Gamma}{L_c} < \beta \Xi \tag{3.13}$$

the system poles are strictly complex and unstable. This area is indicated in Figure 3.9 and Figure 3.13 by the gray area.

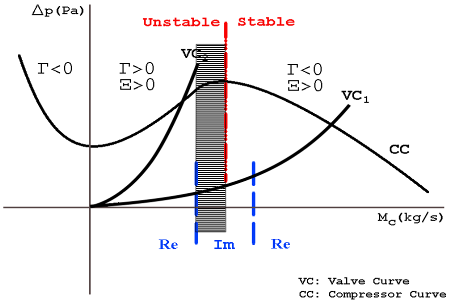
Δp (Pa)
Unstable
Stable
Γ<0
Γ>0
Ξ>0
VC2
Γ<0
Ξ>0
VC1
CC
Mc(kg/s)
Re
Im
Re
VC: Valve Curve
CC: Compressor Curve

Figure 3.13: Region of operating range with complex unstable poles (where $\Im(s) \neq 0$)

(e). When condition (a). is not satisfied and additionally the following condition holds:

$$\frac{A_c\Gamma}{L_c} - \beta\Xi > -\sqrt{(\beta\Xi - \frac{A_c}{L_c}\Gamma)^2 - 4\frac{A_c\beta}{L_c}} \tag{3.14}$$

$$\beta\Xi - \frac{A_c\Gamma}{L_c} > \sqrt{(\beta\Xi - \frac{A_c}{L_c}\Gamma)^2 - 4\frac{A_c\beta}{L_c}} \tag{3.15}$$

the system poles are strictly real and unstable. This area is indicated in Figure 3.9 and Figure 3.14 by the gray area.

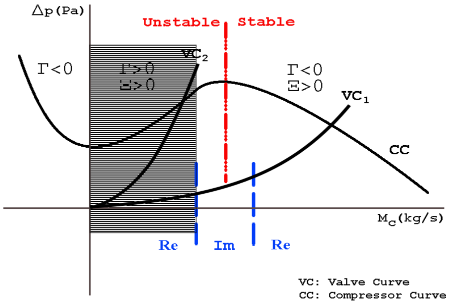
Δp (Pa)
Unstable
Stable
Γ<0
Γ>0
Ξ>0
VC2
Γ<0
Ξ>0
VC1
CC
Mc(kg/s)
Re
Im
Re
VC: Valve Curve
CC: Compressor Curve

Figure 3.14: Region of operating range with strictly real unstable poles

The system pole conditions for whole compressor operation region are derived, two specific points are investigated in the following subsection.

③ Transfer complex/real solution

In this section the derivation of conditions for the points where system poles transfer from complex to strictly real and vice versa. Recalling the pole solution for the Greitzer model:

$$s_{1,2} \;=\; -\frac{\beta\Xi}{2} + \frac{A_c\Gamma}{2L_c} \pm \frac{1}{2}\sqrt{(\beta\Xi + \frac{A_c}{L_c}\Gamma)^2 - 4\frac{A_c\beta}{L_c}}$$

Therefore the solutions of equating the discriminant to zero, gives:

$$\Gamma_1 = \frac{-\Xi\beta L_c - 2\sqrt{A_c L_c \beta}}{A_c} \quad\wedge\quad \Gamma_2 = \frac{-\Xi\beta L_c + 2\sqrt{A_c L_c \beta}}{A_c}$$

For Γ_1 no additional condition is required, Γ_2 needs the following condition to be positive:

$$-\Xi\beta L_c < 2\sqrt{A_c L_c \beta}$$

The transfer points belonging to the solutions Γ_1 and Γ_2 are presented in Figure 3.15.

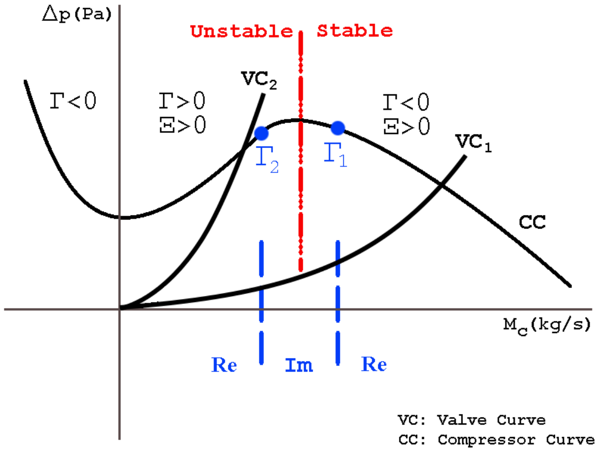

Figure 3.15: Transfer points complex/real

The last parameter case is the transfer point of the system poles stable/unstable solution.

④ Transfer unstable/stable solution

Finding the point where the system poles transfer from stable to unstable (or vice versa) requires the usage of Routh's stability criterion. Bearing this in mind and recalling the characteristic polynomial for this system:

$$s^2 + (\beta\Xi - \frac{A_c}{L_c}\Gamma)s + (1 - \Gamma\Xi)\frac{A_c\beta}{L_c}$$

Equating the polynomial coefficients with zero gives two solutions for Γ as a function of Ξ, β, L_c and A_c:

$$\Gamma_1 = \frac{\Xi\beta L_c}{A_c} \quad \vee \quad \Gamma_2 = \frac{1}{\Xi} \tag{3.16}$$

Substituting the Γ solutions into the analytical system pole solutions, equation (3.9), results into:

$$\Gamma = \Gamma_1 \quad \rightarrow \quad s_{1,2} = \pm\sqrt{(\beta\Xi^2 L_c - A_c)\frac{\beta}{L_c}} \tag{3.17}$$

$$\Gamma = \Gamma_2 \quad \rightarrow \quad s_1 = -\frac{1}{2}(-\beta\Xi + \frac{A_c}{L_c\Xi}) \quad \wedge \quad s_2 = \frac{3}{2}(-\beta\Xi + \frac{A_c}{L_c\Xi}) \tag{3.18}$$

When the following condition holds:

$$\beta\Xi^2 L_c < A_c \tag{3.19}$$

and the solution of (3.17) is used, the system poles are complex. From the operation point analysis it is known that the system poles are complex at the unstable/stable transfer point. Therefore the unstable/stable transfer point solution is equal to (3.17) under assumption that (3.19) holds. For the operating region around the stable/unstable operation point (Figure 3.9) the values for Γ, Ξ, A_c and L_c are greater than zero hence the ubstable/stable operation point must lie left of the compressor curve maximum. The solution of (3.18) is a trivial solution that is not investigated.

The analytical eigenvalue analysis has resulted in system pole conditions linked to the operation region in the compressor map, in the next section model parameters are varied in order to see the effects of these variations on the eigenvalues.

3.1.4 Greitzer parameter variations

The next step is now to investigate the effect of parameter variations on the Greitzer model, three adjustments are considered, namely:

① the ratio $\frac{A_c}{L_c}$; this ratio is varied on a empirical basis.

② V_1; this parameter is increased to see the effect of a greater plenum.

③ V_2; this parameter is varied by the same ratio's of $\frac{V_1}{V_2}$, as used in the variations in V_1.

① Ratio $\frac{A_c}{L_c}$

First we investigate the effect of variations in the rise and fall time and on the poles and zeros of two model parameters namely A_c and L_c. The rise time is defined as the time needed for filling the plenum, the fall time is defined as the time needed for emptying the plenum. This is visualized in Figure 3.16.

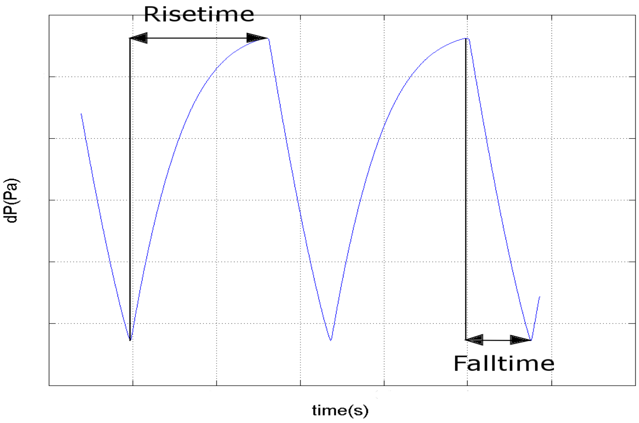

Figure 3.16: Rise time and fall time definition.

The initial parameter values ($A_c = 3.393 \cdot 10^3$ (m^2) and $L_c = 0.386$ (m^2)) were acquired from the experimental setup, see Table B.1 in Appendix B. Trends that were investigated are; the trend of rise and fall times of pressure differences and the trend of the corresponding poles and zero locations.

The variations of ratio $\frac{A_c}{L_c}$ are summarized in Table A.3, during the tests this ratio is increased. The ratio variations are visible in the upper part of Figure 3.17, the lower left part of this figure shows the rise times and the lower right part shows the fall times. The trends show that an increasing ratio $\frac{A_c}{L_c}$ leads to decreasing rise and fall times. The rise time decreases slightly because the medium is accelerated over a shorter period i.e. the compressor duct length, L_c, decreases but simultaneously A_c increases. Because of an increasing A_c, the medium will experience less resistance during flow. However during backflow the medium travels from the plenum through the compressor in the reversed direction and therefore it takes longer to empty the plenum, hence the fall time decreases.

The influence of variations of ratio $\frac{A_c}{L_c}$ on the system poles is visualized in Figure 3.18 and Figure 3.19. where the left part is a zoom of the figure's right part. When looked at the trends of the eigenvalues by increasing ratio $\frac{A_c}{L_c}$ it can be seen that the slow, dominant, pole first shifts into the RHP and (from test **A4**) it starts shifting towards the LHP. The second pole only shift into the RHP.

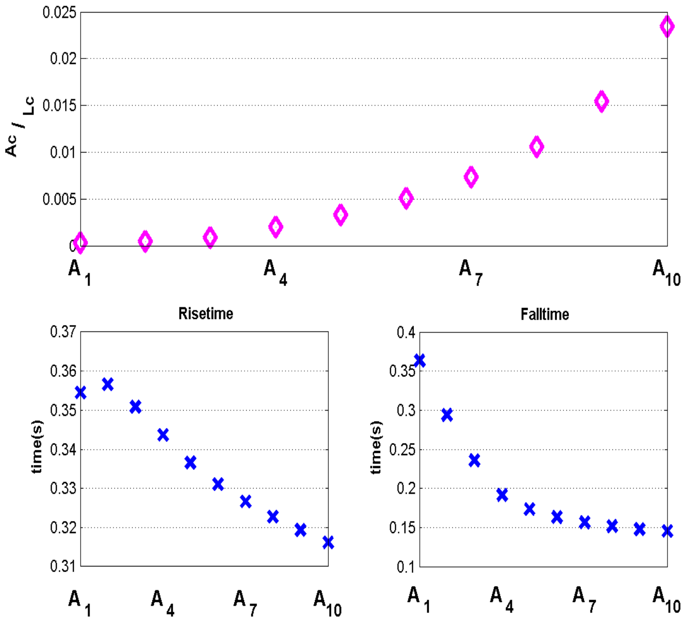

Figure 3.17: Ratio $\frac{A_c}{L_c}$, rise and fall times

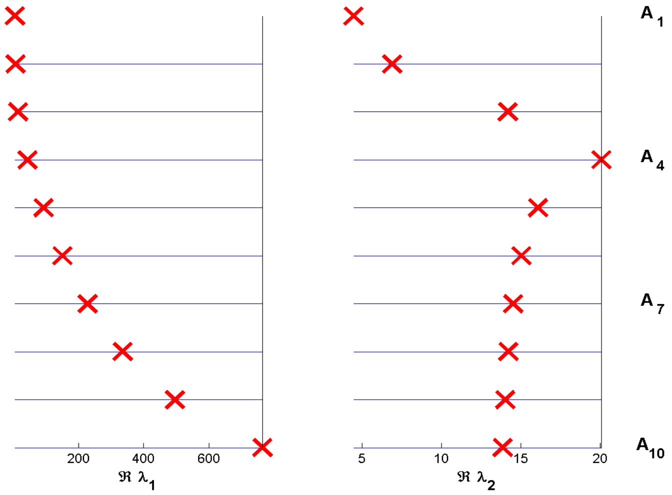

Figure 3.18: Real part poles for $\frac{A_c}{L_c}$ variations

For low ratios of $\frac{A_c}{L_c}$, the poles have an imaginary part that disappears for higher ratio values, see Figure 3.19.The zero only shifts further into the RHP for increasing ratio $\frac{A_c}{L_c}$.

② Parameter V_1

We now discuss the effect of variation in V_1. The trends that are investigated are; trends of rise and fall times and trends poles and zeros. The initial value for the V_1 was $3.0693(m^3)$, and the different test values are given in Table A.4 in Appendix A.

As can be seen in the upper parts of Figure 3.20 an increasing piping volume leads to increasing rise and fall

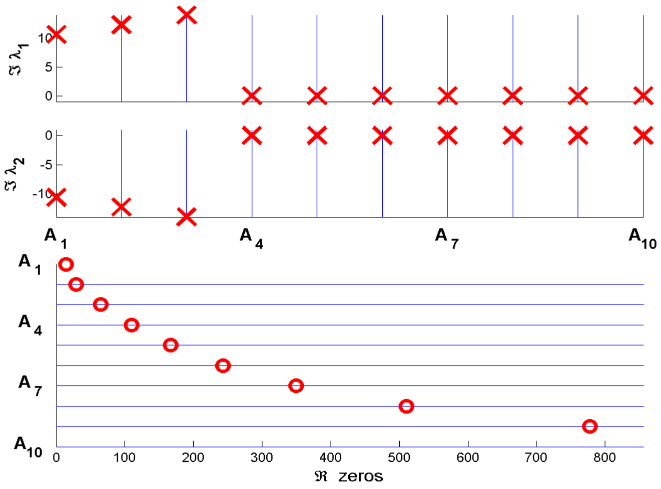

Figure 3.19: Imaginary part poles and zeros for $\frac{A_c}{L_c}$ variations

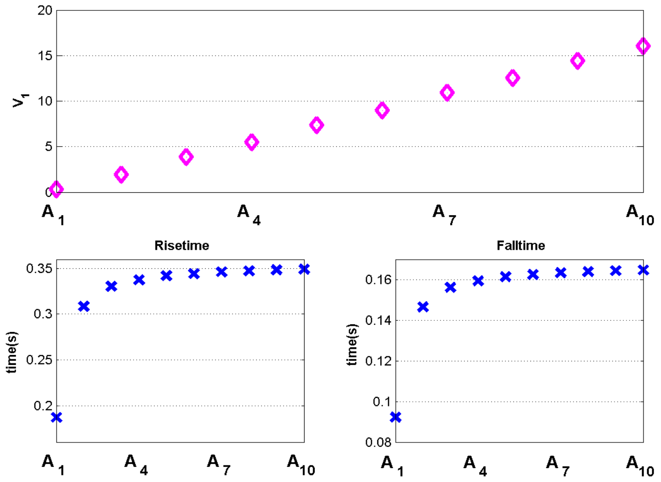

Figure 3.20: V_1, rise and fall times for V_1 variations

times. It is evident that an increased volume takes longer to fill/empty.
For variation in system volumes (V_1 and V_2) a similar ratio $\frac{V_1}{V_2}$ is maintained in order to make fair comparisons between the two system volume tests. In Figure 3.21 can be seen that increasing parameter V_1 does not influence the poles much for higher $\frac{V_1}{V_2}$ ratio (i.e. test 10).

A shift of the left pole, towards the LHP can be seen, whereas the right pole shows a similar shift into the RHP. The poles of all tests are strictly real, and all tests have a zero at 291.60. An explanation about the effect of varying V_1 on the rise/ fall times and on pole/zero locations has been given, in the next paragraph changes of the plenum volume will be discussed.

③ Parameter V_2

In this paragraph the plenum volume, V_2, is varied, the initial values of the plenum volume V_2 is $0.3204(m^3)$. The same ratio $\frac{V_1}{V_2}$ as in the V_1 variation tests is used in this section, see Table A.5 in Appendix A. The decrease of parameter V_2 (decrease of the plenum volume) results in decreasing rise and fall times, see Figure 3.22 , .

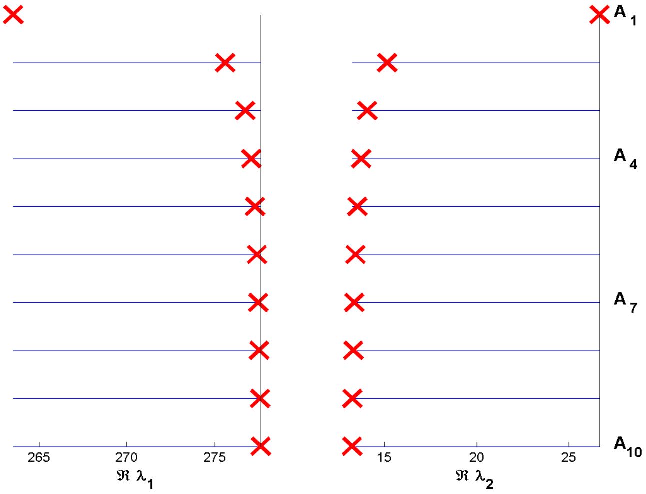

Figure 3.21: Real part poles for V_1 variations

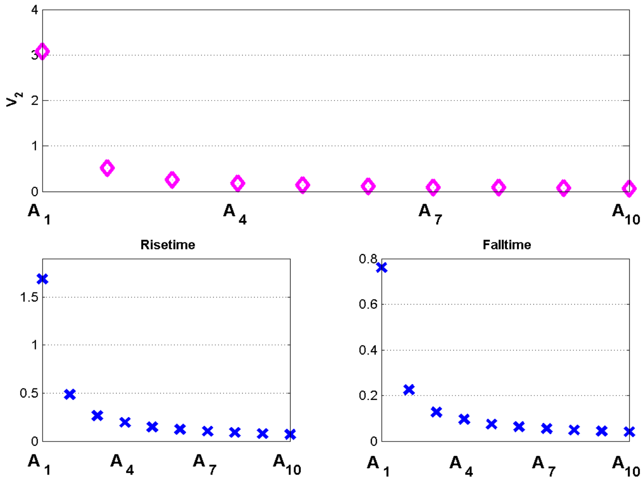

Figure 3.22: V_2, rise and fall times for V_2 variations

The system poles seem to shift towards each other for decreasing plenum volume. The trends for these volume changes shows a left pole that evolves towards the right pole. The linearized system had system poles that were strictly real with a zero at 291.60.

In the previous subsections some eigenvalue and zero trends were observed by different when varying various model parameters. In the following subsection an explanation about the normalized distance between zero(s) and pole(s) will be given.

3.1.5 Greitzer normalized distance between pole and zero

In order to see what the distance between the zero and poles is, a criterion is formulated (normalized distance) that is computed for selected compressor operation points. The normalized distance normalizes the absolute distance between the real parts of pole and zero:

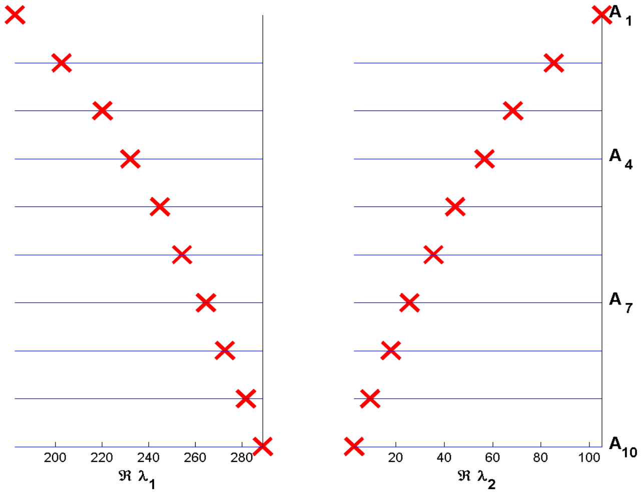

Figure 3.23: Real parts poles and zeros for V_1 variations

$$d_{nor} = \frac{|\Re(s)| - |\Re(z)|}{|\Re(z)|} \tag{3.20}$$

For the Greitzer model, a box is plotted in the compressor map (see Figure 3.24) that marks the area where the poles are strictly real. The two star signs in this figure mark the investigated operation points.

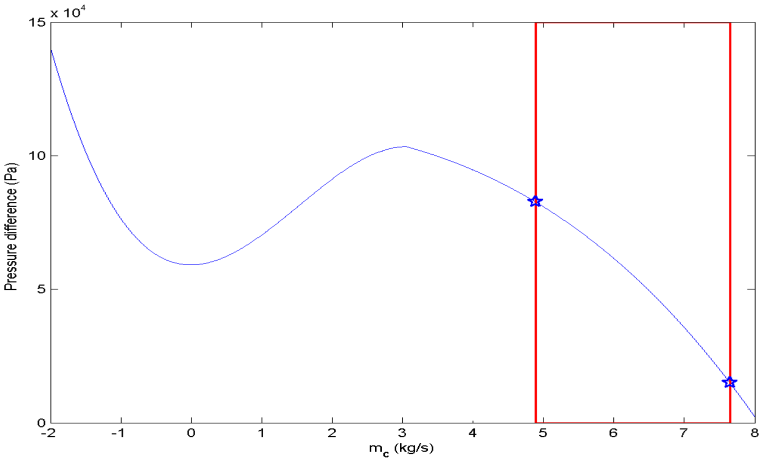

Figure 3.24: Division compressor map for normalized distance

The normalized distances are only looked at for strictly real poles (Im(s)=0) and zeros (Im(z)=0), because the normalized distance from complex poles (Im(s)≠0) and zeros (Im(z)≠0) is difficult to interpret.

The poles and zeros belonging to the operation points marked by the star signs are separately plotted in Figure 3.25 in subfigures. The upper left subfigure of Figure 3.25 shows the normalized distance of the first pole (pole related to the transition from $\dot{m}_c > 0$ to $\dot{m}_c < 0$ (and vice versa)) and zero at the first star sign in Figure 3.24. The upper right subfigure of Figure 3.25 shows the normalized distance of the first pole and zero at the second star sign in Figure 3.24, etc. Judging by Figure 3.24 and Figure 3.25 it can be seen that for increasing mass flow, the normalized distance decreases for both poles.

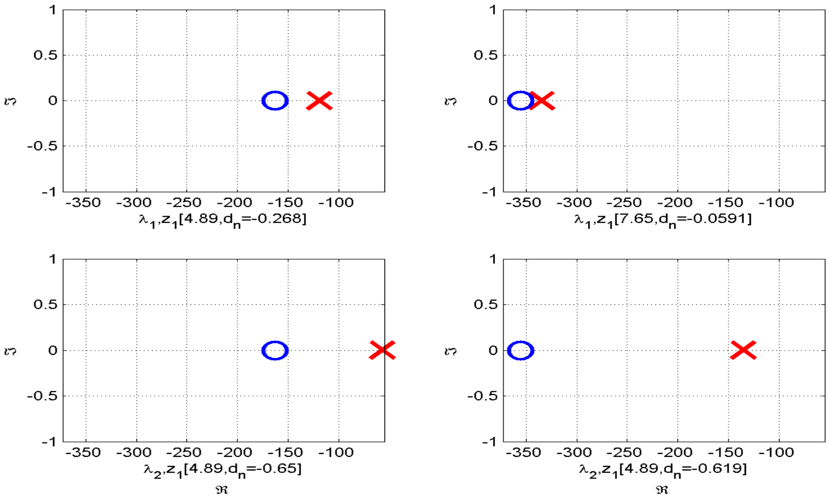

Figure 3.25: Normalized distances for system poles and zero

It can be concluded that in the area of interest the poles are complex and that for higher mass flows (≥ 4.8(kg/s)) the normalized distance for the first system pole and zero is smaller then the normalized distance for the first system pole and zero. The normalized distances from the Greitzer model will be compared to the normalized distances of the extended Greitzer model in the next section.

3.1.6 Conclusion Greitzer model

Regarding the tests done for the Greitzer model, the following conclusions can be drawn.

Greitzer operation point variations

The system poles are complex around the operation point that is marginally stable (i.e. $\Re(s) = 0 \wedge \Im(s) \neq 0$ with $s =$ system poles). The area where the system poles are complex, is equal to 80% of the total chosen operation area ($\dot{m}_c \in \{2.6914 \ldots 7.9517\}$). The area where the system poles are complex can be divided into:

- the area where the system poles are complex and unstable, equal to 21% of the total chosen operation area.
- the area where the system poles are complex and stable, equal to 59% of the total chosen operation area.

The operation area where the system poles are stable ($\Re(s) < 0$, $s =$ system poles) is equal to 79% of the total chosen operation area.

Greitzer analytical system pole analysis

The conclusion from the analytical system pole analysis is that the system poles from the marginally stable solution are complex, and that the total compressor operation region can be divided into four subregions:

- A stable subarea where the system poles are strictly real.
- A stable subarea where the system poles are complex conjugate pairs.
- An unstable subarea where the system poles are complex conjugate pairs.
- An unstable subarea where the system poles are strictly real.

Greitzer parameter variation

From the Greitzer parameter variations we conclude the following, about the pressure difference rise and fall times:

- When the ratio $\frac{A_c}{L_c}$ is exponential increased, the rise time shows a slight decrease (-11%). This is due to the fact that because the compressor duct area (A_c) increases, the medium will experience less resistance therefore the plenum will be filled faster.
- The increase of ratio $\frac{A_c}{L_c}$ causes an exponential decrease (-61%) in fall time. Increasing ratio $\frac{A_c}{L_c}$ i.e. increasing A_c causes the plenum to empty faster (=backflow) despite of the reversed design flow direction.
- When the piping volume (V_1) is exponentially increased, it takes longer to fill or empty the plenum. Both rise and fall time increase exponentially; the rise time increases with 84%, the fall time increases with 83%.
- When the plenum volume (V_2) is exponentially decreased, it causes the plenum to fill and empty faster. Both rise and fall time decrease exponentially; the rise time decreases by 35%, the fall time decreases by 91%.

The parameter variations show that variation of the ratio $\frac{A_c}{L_c}$ and V_1 do not affect the rise and fall time much, in contrast with the effect of parameter V_2.

Regarding the system poles we can conclude that:

- When the ratio $\frac{A_c}{L_c}$ is exponentially increased, it realizes a huge increase (1.68e4%) of the real part of the first pole. This means that, during surge, the transition from the quasistatic compressor curve in the positive mass flow region ($\dot{m}_c > 0$) to the compressor curve in the backflow region ($\dot{m}_c < 0$), is accelerated.
- When the volumes are changed separately, the real parts of the system poles drift away from each other. The volumes V_1 and V_2 were changed separately, when V_1 was changed V_2 was held constant and vice versa. The scheme of ratio $\frac{V_1}{V_2}$ during changes in V_1 was similar to the scheme of ratio $\frac{V_1}{V_2}$ during changes in V_2.

Greitzer normalized distance

We can conclude that normalized distances for a mass flow less then 4.8 kg/s do not exist since the normalized distance is defined for strictly real poles (Im(s)=0) and zeros (Im(z)=0), see Figure 3.24.

3.2 Extended Greitzer model and parameter experiments

The extended Greitzer model and its linearization are described in this section followed by the same operation point analysis as done by the Greitzer model in the previous section. In contrast with the Greitzer model, the operation point analysis is succeeded here by a numerical eigenvalue analysis. This is done because of the complex analytical solution of the extended Greitzer model. The parameter study of the extended Greitzer model is comprehended by the variation of the parameter values in order to see changes in eigenvalues. The parameter study is followed by a normalized distance analysis and finally conclusions about this model are given.

3.2.1 Extended Greitzer model

Recalling the extended Greitzer model differential equations and adjusting them for a closed loop system yields;

$$\begin{aligned}
\frac{d\dot{m}_c}{dt} &= \frac{A_c}{L_c}\{\Delta p_c(\dot{m}_c) + \Delta p\} + \chi && (3.21)\\
\frac{d\Delta p}{dt} &= F_{lin} \cdot \{\dot{m}_c - \dot{m}_v(\Delta p, u_v)\} && (3.22)\\
\tau\frac{d\chi}{dt} &= C' \frac{h^2 A_c}{\nu L_c} \frac{\partial \Delta p_c(\dot{m}_c)}{\partial \dot{m}_c} \frac{d\dot{m}_c}{dt} - \chi && (3.23)
\end{aligned}$$

with:

$$\begin{aligned}
\Delta p &= p_2 - p_1\\
\dot{m}_v(\Delta p, u_v) &= \dot{m}_l(\Delta p, u_l) + \dot{m}_s(\Delta p, u_s)\\
F_{lin} &= \frac{\gamma_1 Z_1 R T_{10}}{V_1} + \frac{\gamma_2 Z_2 R T_{20}}{V_2}
\end{aligned}$$

The explanation of the extended Greitzer model parameters C' and τ is given in Appendix C. Equations (3.21), (3.22) and (3.23) are linearized around an operation point ($\dot{m}_{c,o.p.}, \Delta p_{c,o.p.}, u_{l,o.p.}, u_{s,o.p.}$). The closed loop system is rewritten in a state space manner to equations (3.24) and (3.25).

$$\begin{aligned}
\dot{\underline{\tilde{\mathbf{x}}}} &= \mathbf{A} \cdot \underline{\tilde{\mathbf{x}}} + \mathbf{B} \cdot \underline{\tilde{u}} && (3.24)\\
\underline{\tilde{\mathbf{y}}} &= \mathbf{C} \cdot \underline{\tilde{\mathbf{x}}} + \mathbf{D} \cdot \underline{\tilde{u}} && (3.25)
\end{aligned}$$

The state vector is defined as: $\mathbf{x} = \begin{bmatrix}\dot{m}_c & \Delta p & \chi\end{bmatrix}^T$ therefore the extended Greitzer closed loop system matrices are equal to:

$$\tilde{\mathbf{x}} = \begin{bmatrix}\dot{m}_c\\ \Delta p\\ \chi\end{bmatrix}_{\mathbf{x}=\mathbf{x}_{o.p.}} \quad (3.26) \qquad \tilde{\mathbf{u}} = \begin{bmatrix}u\end{bmatrix}_{\mathbf{x}=\mathbf{x}_{o.p.}} \quad (3.27)$$

$$\mathbf{A} = \begin{bmatrix}
\alpha\frac{\partial \Delta p_c(\dot{m}_c)}{\partial x_1} & -\alpha & 1\\
F_{lin} & -F_{lin} \cdot \frac{\partial \dot{m}_v(\Delta p, u_v)}{\partial x_2} & 0\\
\frac{\alpha^2\gamma}{\tau}\frac{\partial^2 \Delta p_c(\dot{m}_c)}{\partial x_1^2}(\Delta p_c(\dot{m}_c) - x_2 + \frac{x_3}{\alpha}) & -\frac{\alpha^2\gamma}{\tau}\frac{\partial \Delta p_c(\dot{m}_c)}{\partial x_1} & \frac{1}{\tau}(\alpha\gamma\frac{\partial \Delta p_c(\dot{m}_c)}{\partial x_1} - 1)\\
+\frac{\alpha^2\gamma}{\tau}\frac{\partial \Delta p_c(\dot{m}_c)}{\partial x_1}\frac{\partial \Delta p_c(\dot{m}_c)}{\partial x_1} & &
\end{bmatrix}_{\mathbf{x}=\mathbf{x}_{o.p.}} \quad (3.28)$$

$$\mathbf{B} = \begin{bmatrix}0\\ -F_{lin} \cdot \frac{\partial \Delta p_v}{\partial u}\\ 0\end{bmatrix}_{\mathbf{x}=\mathbf{x}_{o.p.}} \quad (3.29) \qquad \mathbf{C} = \begin{bmatrix}1 & 0 & 0\\ 0 & 1 & 0\\ 0 & 0 & 0\end{bmatrix}_{\mathbf{x}=\mathbf{x}_{o.p.}} \quad (3.30) \qquad \mathbf{D} = \begin{bmatrix}0\\ 0\\ 0\end{bmatrix}_{\mathbf{x}=\mathbf{x}_{o.p.}} \quad (3.31)$$

A remark must be made about the output matrix **C**; for a fair comparison between the Greitzer model and the extended Greitzer model we chose the output matrix to be similar to the Greitzer output matrix instead of a full state feedback matrix. It must be noted that it is difficult to measure mass flows.

In order to investigate changes of the **A**-matrix eigenvalues, the operation point $(\dot{m}_{c,o.p.}, \Delta p_{c,o.p.}, u_{l,o.p.}, u_{s,o.p.})$ is changed. This is done by multiplying the surge flow, $\dot{m}_c^*$ (measure on experimental setup), with a parameter, Fqs_i, for which applies:

$$Fqs \in \{0.88, 0.89, \ldots, 1.28, 1.29, 1.30, 1.40, \ldots, 2.50, 2.60\}$$

With this parameter variation a percentage of surge flow is obtained per test case:

$$\dot{m}_{c,i} \quad = \quad Fqs_i \cdot \dot{m}_c^*, \quad i \in \{1, 2, \ldots, 55, 56\}$$

The operation points can be seen on the compressor curve as shown in Figure 3.26.

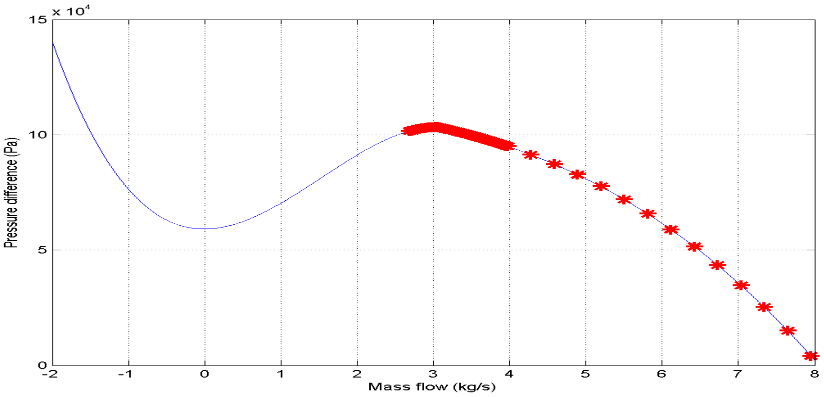

Figure 3.26: Fqs variation and compressor curve.

We now continue with a discussion on system pole changes at different operation points.

3.2.2 Extended Greitzer operation point variation

The operation points are varied in order to see changes in system pole locations, this has to be clear in order to know the distinction between the stable and unstable operation area.

In Figure 3.27 the real parts of the separate eigenvalues are plotted versus the mass flows. When the operation point approaches the surge point from within the unstable flow regime ($Fqs \in \{0.88, \ldots, 1\}$), it can be seen that the real parts eigenvalue λ_1, evolve towards the stable region. In contrast with λ_1, the real parts of λ_2 shift towards the LHP when the mass flow is increased. Since λ_1 and λ_2 can be linked to the compressor system as follows; the first eigenvalue, λ_1, represents flow reversal (the transition from $\dot{m}_c > 0$ to $\dot{m}_c < 0$ (and vice versa)) and the second eigenvalue, λ_2, is the eigenvalue representing the filling and emptying of the plenum. The changes from λ_1 and λ_2 for increasing mass flow can be related to; the surge cycle (shape) in the unstable operating area or in the stable operating area the transition of a arbitrary point towards the quasistatic compressor curve.

The third extended Greitzer eigenvalue, λ_3, is zero for $Fqs \in \{0.88, \ldots, 1\}$ and for higher Fqs values this eigenvalue shifts into the LHP. This eigenvalue accounts for the compressor transition time from unsteady to quasi-static behavior.

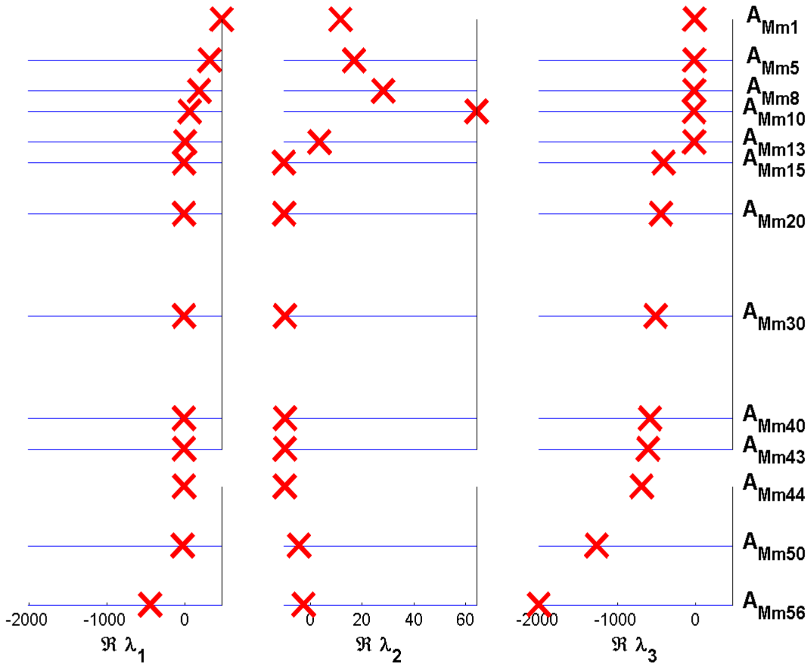

Figure 3.27: Real part extended Greitzer system poles for Fqs variation.

When we look at the behavior of the imaginary parts (Figure 3.28) of the different eigenvalues, it becomes clear that the third eigenvalue is strictly real. The first and second eigenvalue show a imaginary part for mass flows between 2.94(kg/s) and 4.59(kg/s), or $Fqs = 0.96 - 1.50$.

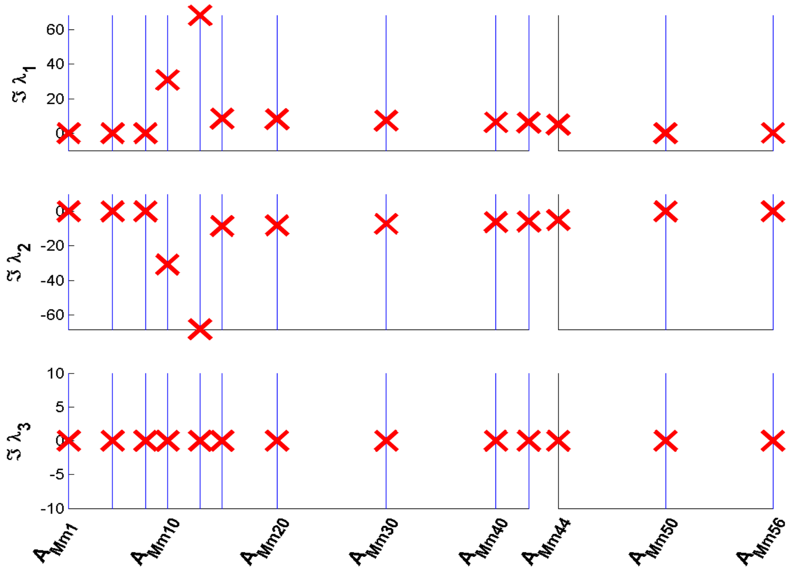

Figure 3.28: Imaginary part extended Greitzer system poles for Fqs variation.

When the eigenvalue data is plotted in the complex plane, Figure 3.29 and Figure 3.30 are obtained.

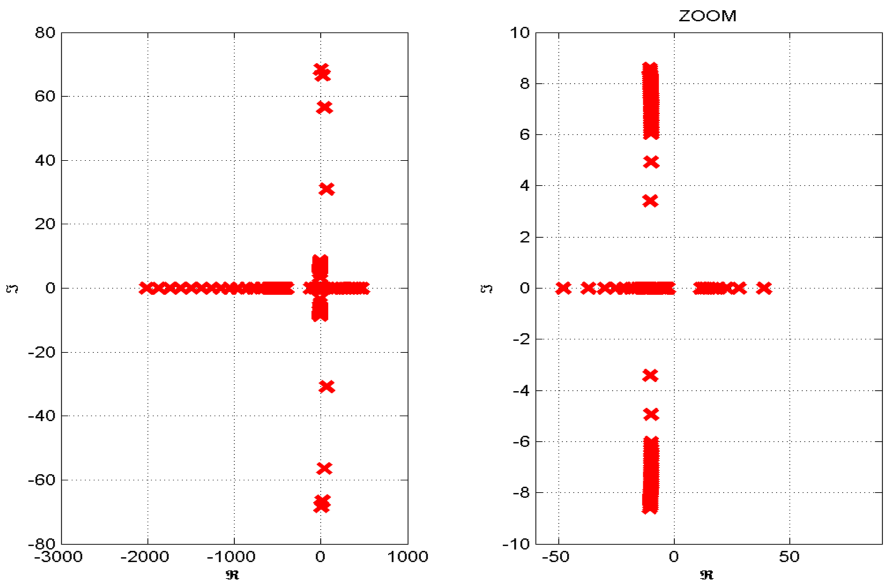

Figure 3.29: Extended Greitzer system poles for Fqs variation.

In the right part of Figure 3.29 the eigenvalues of the linearized extended Greitzer model are plotted for various operation points. In the left part of this figure we zoomed in to visualize the evolution of the eigenvalues around the imaginary axis. In Figure 3.30 the eigenvalues are plotted separately.

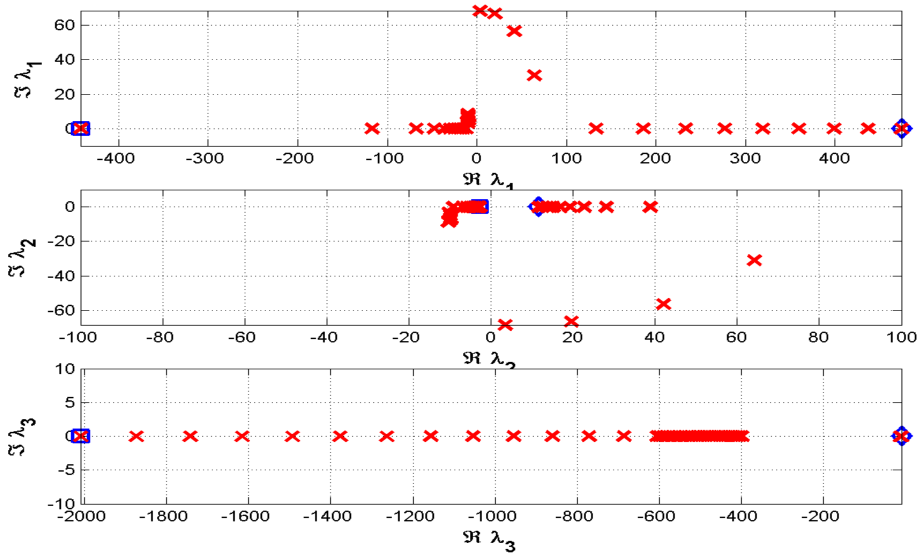

Figure 3.30: Separately extended Greitzer system poles for Fqs variation.

The diamond shows the eigenvalue at the first test case, whereas the square shows the eigenvalue at the last test case. The evolution of the first and third eigenvalue (upper respectively lower part of Figure 3.30) consist of evolutions from the RHP towards the LHP. As with the Greitzer model, the second eigenvalue evolves in a clockwise motion from the RHP into the LHP and then back towards the RHP. The next step is description of the zero evolution, therefore the linearized system's transfer functions are computed by:

$$H(s) \quad = \quad \mathbf{C}(s\mathbf{I} - \mathbf{A})^{-1}\mathbf{B} + \mathbf{D} \tag{3.32}$$

Take for example the first stable test case ($Fqs = 1.01$), the transfer functions for the full state output are given pro forma followed by the reduced state output transfer function. The transfer functions are given for:

- **Full state output**

  The first transfer function, H_{11}, is the transfer function from the input (position control valve) to the first output i.e. compressor mass flow. H_{12} is therefore the transfer function from input to the plenum pressure, and H_{13} is the transfer function from input to χ.

$$H_{11} \quad = \quad \frac{12.67s + 989.7}{s^3 + 241.9s^2 + 1.216e004s + 4.018e005} \tag{3.33}$$

$$H_{12} \quad = \quad \frac{-1230s^2 - 2.892e005s - 7.311e006}{s^3 + 241.9s^2 + 1.216e004s + 4.018e005} \tag{3.34}$$

$$H_{12} \quad = \quad \frac{-1025s}{s^3 + 241.9s^2 + 1.216e004s + 4.018e005} \tag{3.35}$$

  Because output feedback is applied the other transfer function is equal to zero, as can be visualized in the Bode plots; Figure 3.31.

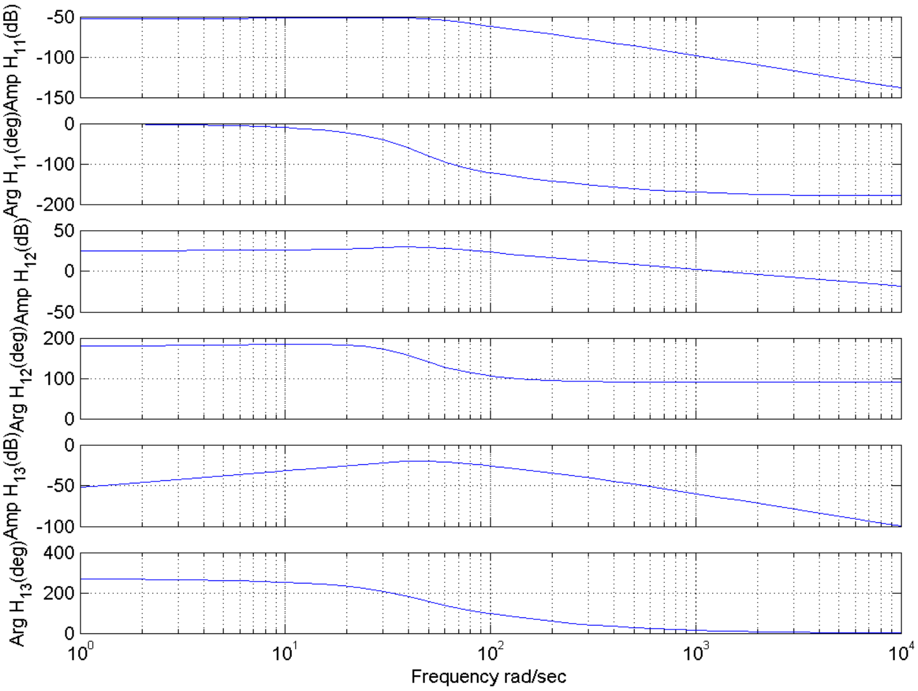

Figure 3.31: Extended Greitzer Bode plot.

- **Reduced state output**

  The first transfer function, H_{11}, is the transfer function from the input (position control valve) to the first output i.e. compressor mass flow. The transfer function H_{12} is the transfer function from input to the plenum pressure.

$$H_{11} = \frac{12.67s + 989.7}{s^3 + 241.9s^2 + 1.216e004s + 4.018e005} \tag{3.36}$$

$$H_{12} = \frac{-1230s^2 - 2.892e005s - 7.311e006}{s^3 + 241.9s^2 + 1.216e004s + 4.018e005} \tag{3.37}$$

The Bode plots of the transfer functions are given in Figure 3.31.

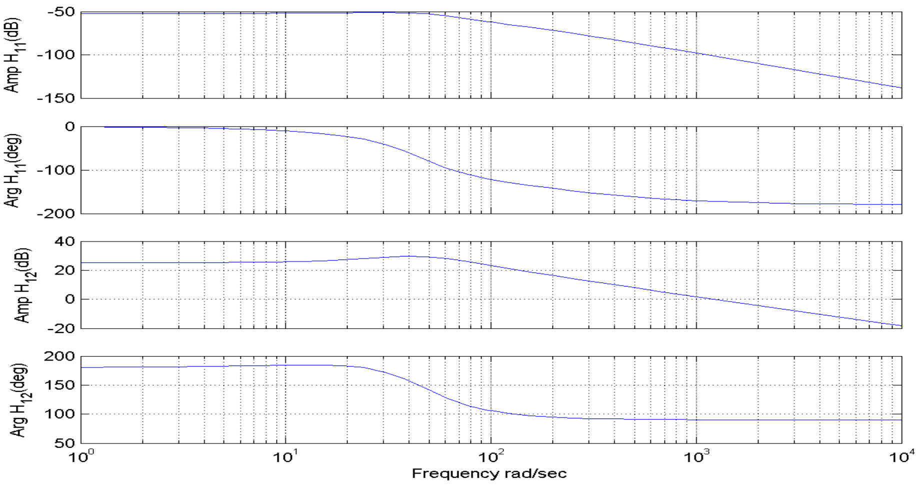

Figure 3.32: Extended Greitzer Bode plot.

The Bode plots of the extended Greitzer models, Figure 3.32, are similar to those of the Greitzer model, Figure 3.7. From this moment on, the reduces state output is used to, as stated before, make a fair comparison with the Greitzer model.

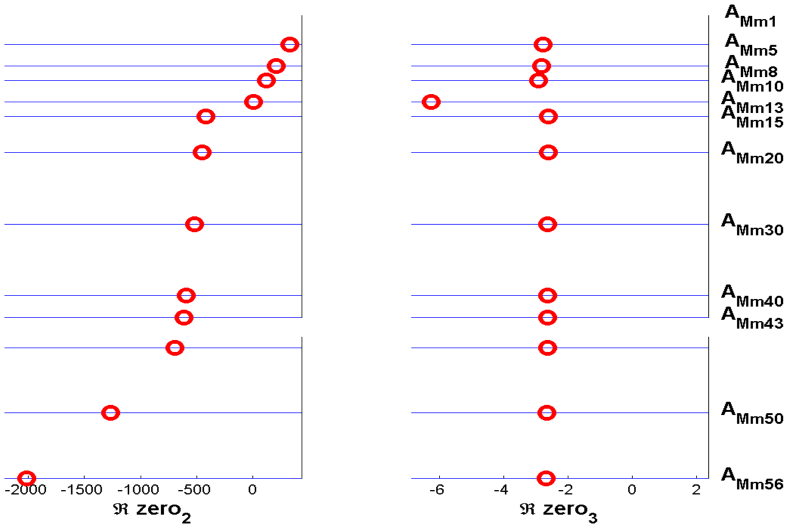

Figure 3.33: Zeros extended Greitzer

In Figure 3.33 the evolution of the zeros from the second transfer function (3.37) is shown, the first transfer function (3.36) has a zero at -14.13. The zero evolution of the second transfer function (left part of Figure 3.33) shows that the linearized extended Greitzer model is a non-minimum phase system for $Fqs \in \{0.88, \ldots, 1\}$. From $Fqs = 1.01$ the zero shifts into the LHP, the other zero is stable and plotted in the right part of Figure 3.33.

The changes of eigenvalues for the extended Greitzer model have been elucidated in this subsection. It can be concluded from the operation point variations that the linearized extended Greitzer model is stable form $Fqs \geqq 1.01$.

3.2.3 Extended Greitzer numerical system pole analysis

The analytical solution of the extended Greitzer model gives a solution that is complex to interpret, therefore we chose to perform a numerical eigenvalue analysis of the extended Greitzer model. In the area of interest operation points, that are similar to those of the Greitzer eigenvalue analysis (i.e. the transfer points of the complex/real solution and the stable/unstable operation point) are computed for the Extended Greitzer model.

Transfer imaginary/real solution

We define the term γ and recall the third equation of the extended Greitzer model:

$$\gamma = C' \frac{h^2}{\nu}$$

and:

$$\tau \frac{d\chi}{dt} = \gamma \frac{A_c}{L_c} \frac{\partial \Delta p_c(\dot{m}_c)}{\partial \dot{m}_c} \frac{d\dot{m}_c}{dt} - \chi \qquad (3.38)$$

In Table 3.1, the transfer points (complex to real solution and vice versa) are given as well as the marginally stable mass flow for the extended Greitzer model.

Table 3.1: Value for Fqs and $\dot{m}_{c,o.p.}$

GREITZER						
	real→complex (Instable area)		complex (Marginally stable)		complex→real (Stable area)	
	Fqs	$\dot{m}_c$	Fqs	$\dot{m}_c$	Fqs	$\dot{m}_c$
	0.8227	2.5162	0.9925	3.0331	1.5124	4.6254

MEULEMAN						
	real→complex (Instable area)		complex (Marginally stable)		complex→real (Stable area)	
γ	Fqs	$\dot{m}_c$	Fqs	$\dot{m}_c$	Fqs	$\dot{m}_c$
0.3	0.9667	2.9557	1	3.0493	1.5841	4.8448
0.337	0.9671	2.9577	1	3.0493	1.5145	4.6319
0.01	0.9017	2.7577	1	3.0493	2.5076	7.6691

The solution for the Greitzer model, as described in Section 3.1, is given in the first row of Table 3.1. When $\gamma = 0.3$, the solution for the extended Greitzer model differs significantly from the Greitzer solutions. Therefore the γ-parameter of the extended Greitzer model is altered to match the Greitzer results. For $\gamma = 0.337$, the marginally stable and complex/real solution of both model seem to match, however the complex/real solution does not because of difference in size of the area where the system poles are complex. Therefore the γ-parameter value is decreased for the extended Greitzer model in order to match the Greitzer model complex/real transfer point. Even for $\gamma = 0.01$ the Greitzer complex/real solution do not seem to match the extended Greitzer complex/real solution.

The real/complex (unstable area) and complex/real (stable area) transfer points for the extended Greitzer γ-parameter solution of 0.337 are plotted in Figure 3.34 and Figure 3.35 respectively. In Figure 3.34 the operating point is marked on the compressor curve in the upper part. The lower part of this figure, shows the eigenvalues for the operation point.

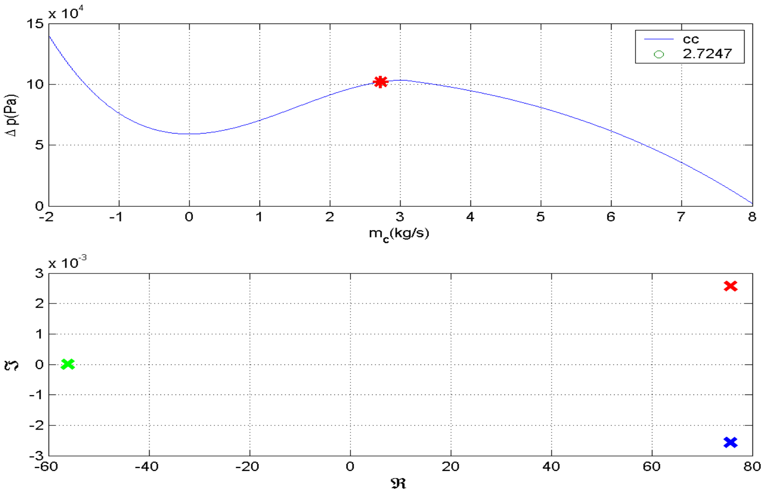

Figure 3.34: Extended Greitzer system poles; real to complex solution.

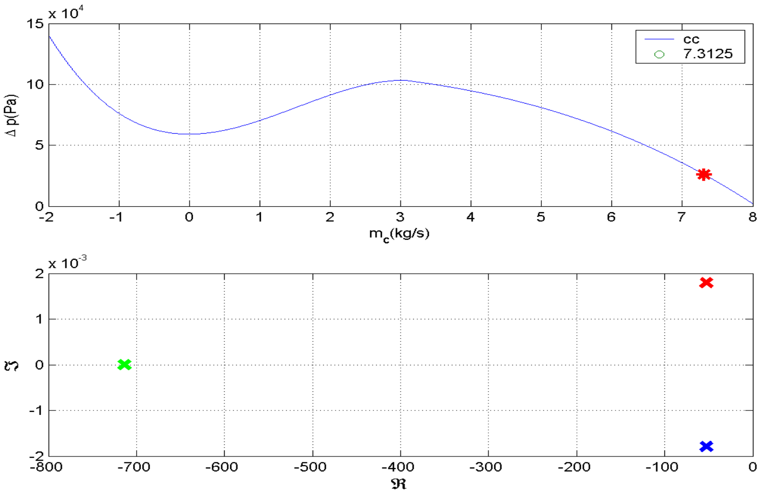

Figure 3.35: Extended Greitzer system poles; complex to real solution.

It can be concluded from the former results that the operating area where the system poles are complex ($\Im(s) \neq 0$) is for the extended Greitzer model smaller then for the Greitzer model. It must be noted when comparing the above results of Greitzer and extended Greitzer, that the Greitzer model does have a γ parameter. For a fair comparison all similar model parameters were kept similar in both the Greitzer model and the extended Greitzer model. The former results also show that the operating area where the system poles are complex ($\Im(s) \neq 0$) is function of the γ-parameter.

The third extended Greitzer system pole is a strictly real pole. Therefore the complex poles of the extended Greitzer model must be coupled to the first two extended Greitzer equations. Since the first extended Greitzer equation (3.21) is similar to the first Greitzer equation (3.1), except for the additional state (χ), and the fact that the model equations (Greitzer model and extended Greitzer model separately) are mutually coupled, the additional state influences the complex system poles. Therefore the difference in complex area's of the compressor models can be ascribed to the influence of the third extended Greitzer equation.

Marginally stable solution

The marginally stable solution is obtained when the mass flow coefficient, Fqs, is equal to 1. This causes the first two eigenvalues to become unstable and therefore the system to become unstable, see Figure 3.36.

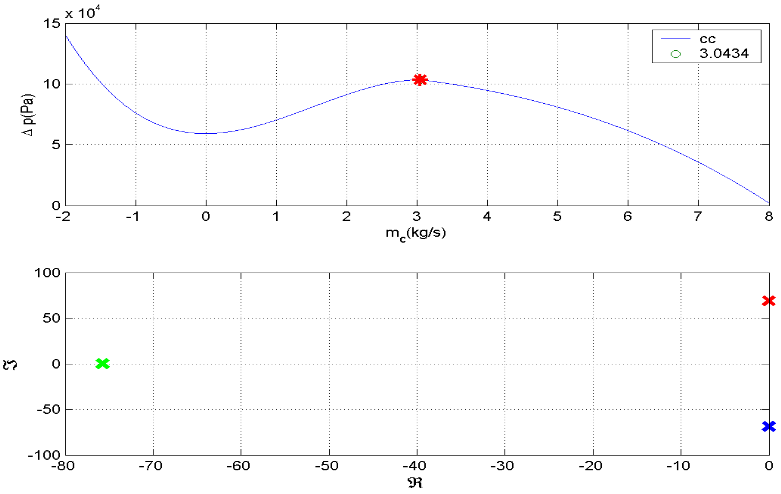

Figure 3.36: Extended Greitzer numerical marginally stable solution.

In contrast with the analytical solution of the Greitzer model, where the marginally stable solution lies left of the surge line, the marginally stable of the extended Greitzer model lies on the surge line (see Appendix Appendix C).

3.2.4 Extended Greitzer model parameter variation

In this section we look at the influence of γ-parameter variations on the eigenvalues. We recall the third equation of the extended Greitzer model and define the terms γ and τ:

$$\tau\frac{d\chi}{dt} = C'\frac{h^2 A_c}{\nu L_c}\frac{\partial \Delta p_c(\dot{m}_c)}{\partial \dot{m}_c}\frac{d\dot{m}_c}{dt} - \chi \tag{3.39}$$

with:

$$\gamma = C'\frac{h^2}{\nu} \text{ and } \tau = \frac{2\pi\delta_s^2}{\alpha_r \nu}$$

The γ-parameter is changed as follows; $\gamma \in \{0.01, 0.02, \ldots, 0.05, 0.10, 0.20, \ldots, 0.50, 0.55\}$. For the compressor under investigation the γ is equal to 0.30, the other parameters are discussed in Appendix C. The operation point analysis, as described in Section 3.2.2, is performed for all separate γ-test (Table A.6 in Appendix A), resulting in Figure 3.37, Figure 3.38, Figure 3.39 and Figure 3.40. The left part of each figure displays the eigenvalues at a certain value of the γ-parameter and the right part of each figure is a zoomed plot around the origin.

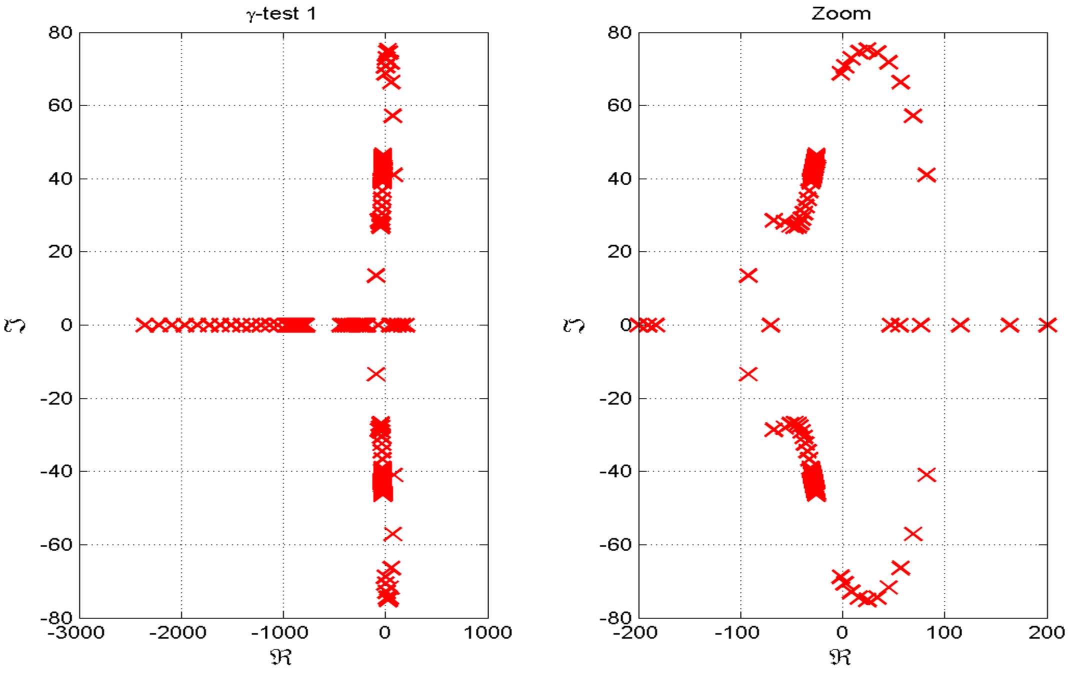

Figure 3.37: Eigenvalues γ-test 1 ($\gamma = 0.01$).

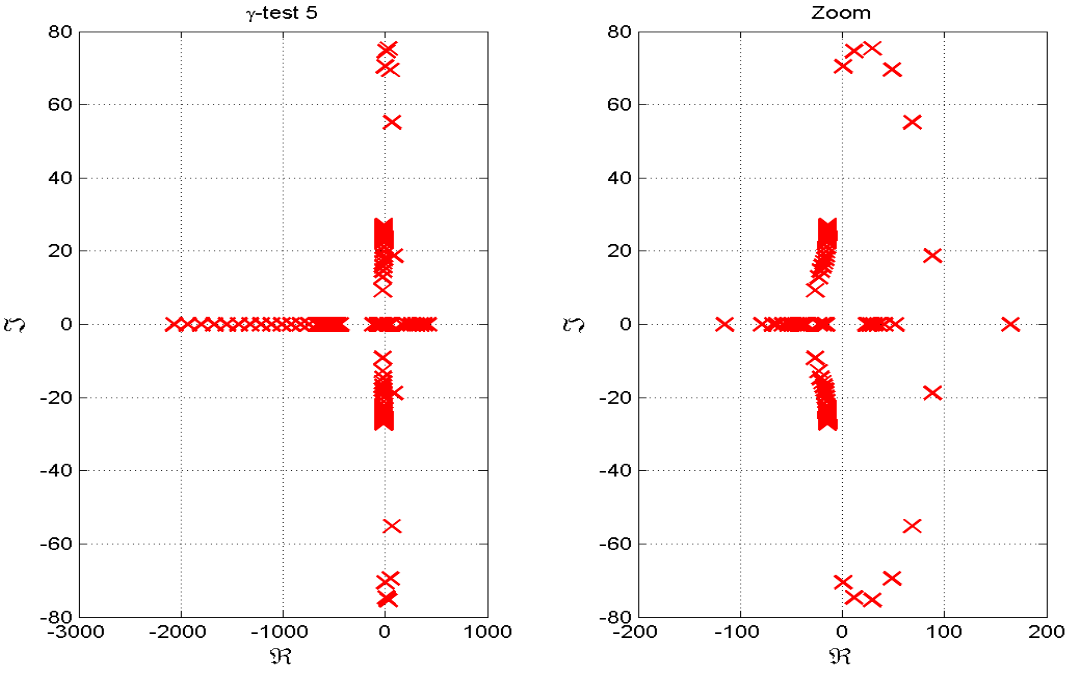

Figure 3.38: Eigenvalues γ-test 5 ($\gamma = 0.05$).

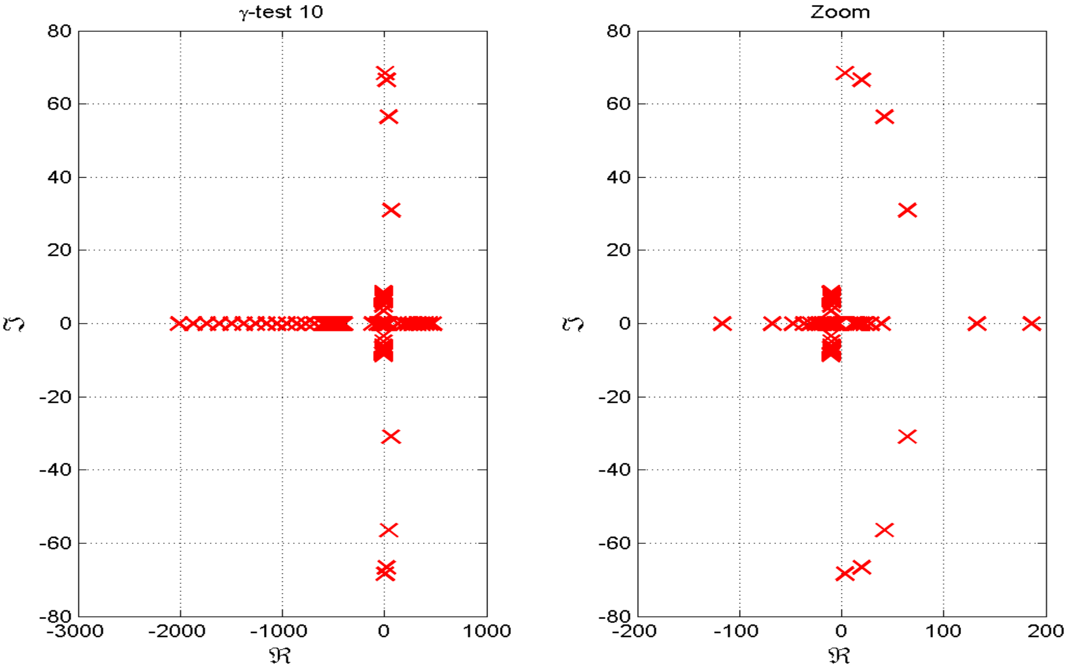

Figure 3.39: Eigenvalues γ-test 10 ($\gamma = 0.30$).

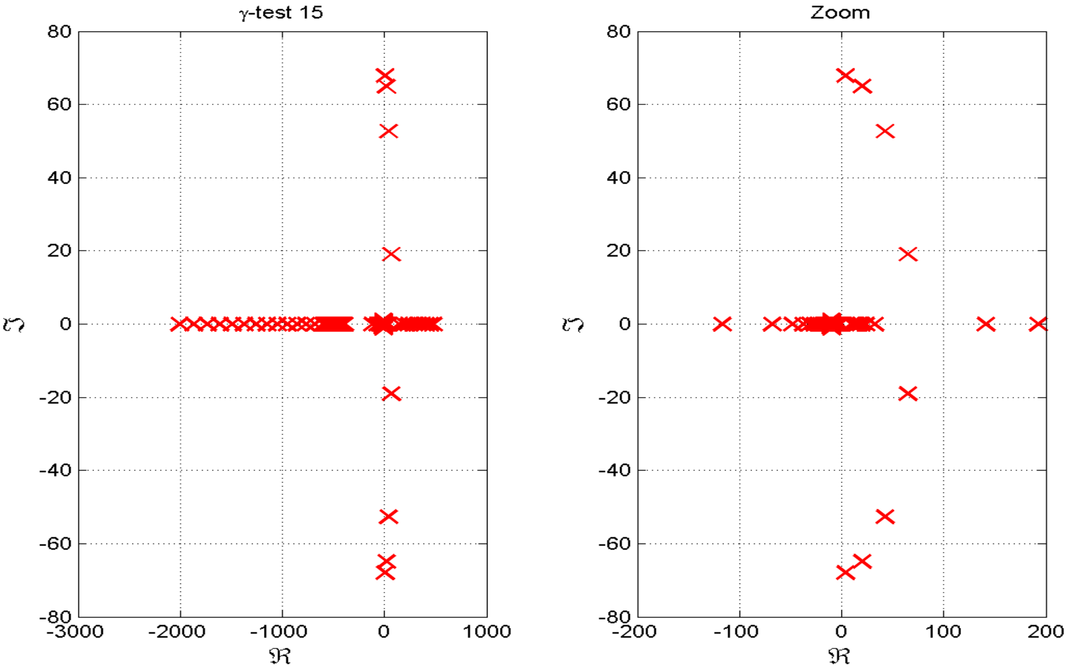

Figure 3.40: Eigenvalues γ-test 15 ($\gamma = 0.55$).

Two trends can be observed from Figures Figure 3.37-Figure 3.40;

① At increasing value of γ the operating area where the system poles are complex ($\Im(s) \neq 0$) decreases.

② At increasing value of γ all eigenvalues shift towards the RHP.

For all variations of the γ-parameter the ratio $\frac{h^2}{\nu}$ stays similar, since this ratio is present in both γ and τ. As can be seen in Table A.6 in Appendix A a linear increase for γ also shows a linear increase in ratio $\frac{h^2}{\nu}$. Growth of the ratio $\frac{h^2}{\nu}$ means that, when the kinematic viscosity is held constant, h must increase. When this is the case, the assumption that the boundary layer is equal to half the width of the compressor outlet becomes questionable. When instead of ν, h is held constant at increasing ratio $\frac{h^2}{\nu}$ it means that the kinematic viscosity is decreased.

$$\nu = \frac{\mu}{\rho},$$

When the above definition for ν is used, decreasing kinematic viscosity is obtained by increasing the density or decreasing the dynamic viscosity. Growth of density, i.e. increasing mass at an equal volume, seems unlikely for this compressor system since it is an closed system e.g. the total mass in the system is constant (still large density variations can occur locally). The only option for decreasing the kinematic viscosity is to decrease the dynamic viscosity. Because of this the damping of the compressed medium decreases, resulting in a decrease of imaginary parts of the system poles.

The decrease of dynamic viscosity could also be the explanation for the shift of all eigenvalues towards the RHP. Since the damping of the system decreases, the system stability decreases and therefore the eigenvalues have to shift towards the RHP.

When the same data is plotted for each eigenvalue individually, the Figure 3.41, Figure 3.42, Figure 3.43, and Figure 3.44 are obtained.

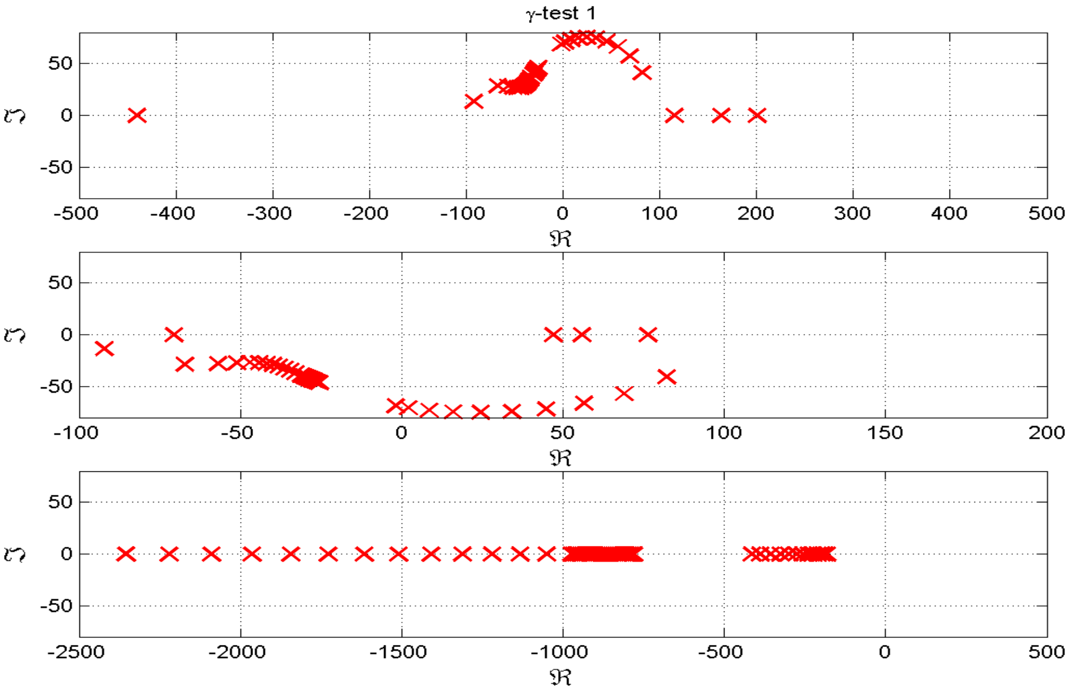

Figure 3.41: Eigenvalues γ-test 1 ($\gamma = 0.01$).

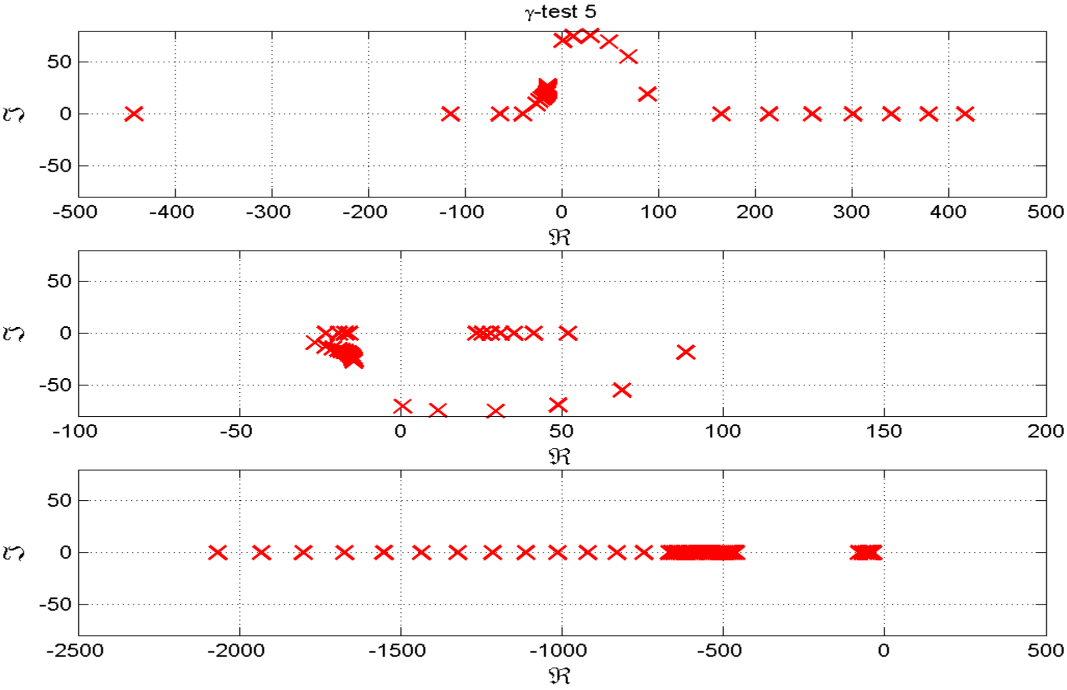

Figure 3.42: Eigenvalues γ-test 5 ($\gamma = 0.05$).

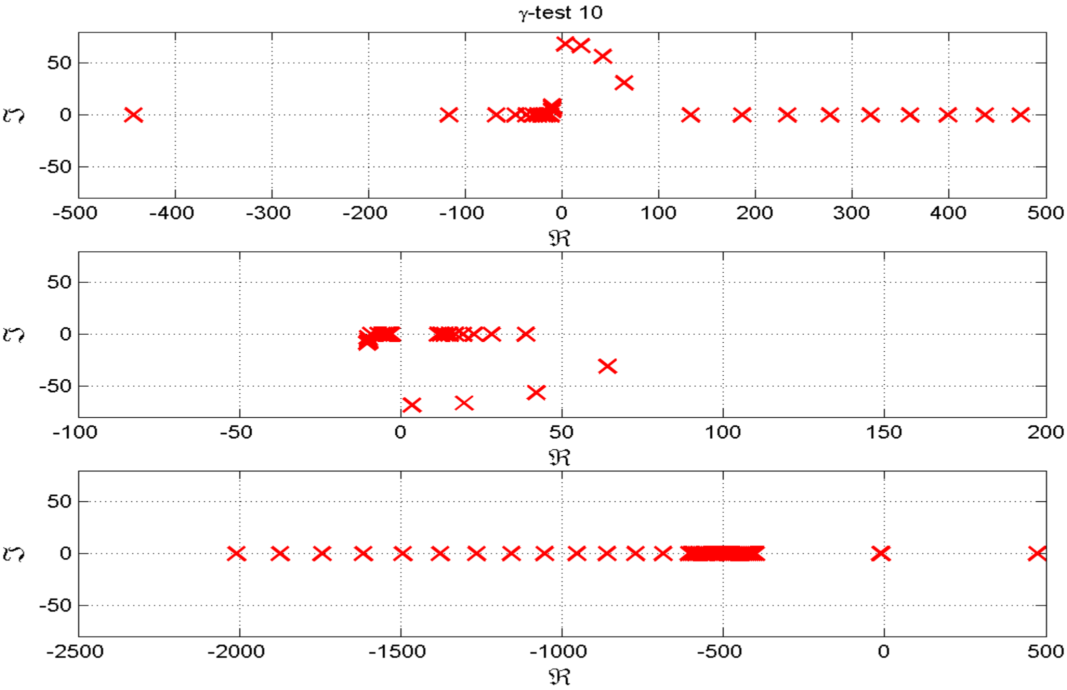

Figure 3.43: Eigenvalues γ-test 10 ($\gamma = 0.30$).

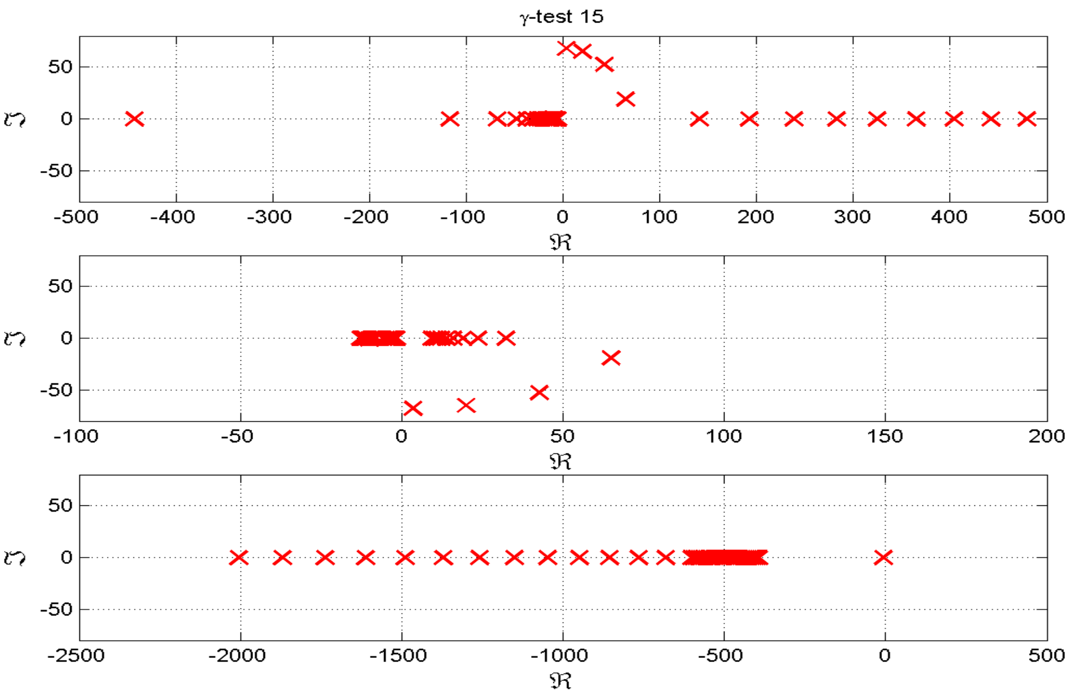

Figure 3.44: Eigenvalues γ-test 15 ($\gamma = 0.55$).

From Figures Figure 3.41-Figure 3.44 the following conclusions can be drawn:

❶ At increasing value of γ the first eigenvalue, λ_1, evolves further into the RHP.

❷ At increasing value of γ the operating area where λ_2 is complex ($\Im(s) \neq 0$), decreases.

The lower part of Figure 3.44 shows a positive value for the third eigenvalue. A positive third eigenvalue is also noticed in other γ-tests, for $\gamma \in \{0.1, 0.2, \ldots, 0.45\}$. These positive third eigenvalues can be explained by the chosen operation point range where the first operation points of this operation range are deep into the unstable area, therefore causing the third eigenvalue to become positive.

The γ variation resulted in more insight into the eigenvalue evolution of the extended Greitzer model. We now have to investigate the pole-zero interaction.

3.2.5 Extended Greitzer normalized distance between pole and zero

In order to quantify the distance between poles and zero(s) for the extended Greitzer model, the normalized distances between poles and zeros are computed. The same criterion as at the Greitzer model is used; the normalized distance normalizes the absolute distance between the real parts of pole and zero:

$$d_{nor} = \frac{|\Re(s)| - |\Re(z)|}{|\Re(z)|} \tag{3.40}$$

The extended Greitzer normalized distance investigation is divided into two parts:

① The normalized distance for the first two poles.

② The normalized distance for the third (strictly real) pole.

① extended Greitzer normalized distance; first pole and second pole

For the first two extended Greitzer system poles, the compressor map is divided by two subarea's indicated by the vertical lines, see Figure 3.45.

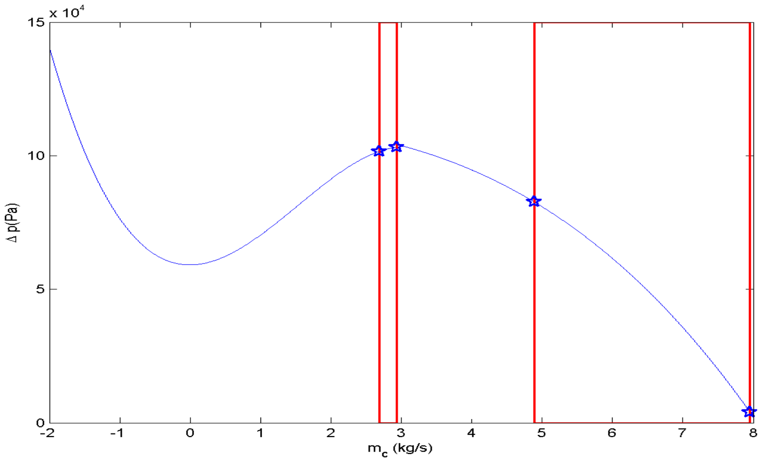

Figure 3.45: Compressor map for d_{nor}

The solid line boxes in Figure 3.45 mark the area's where the poles are strictly real and the four star signs mark the investigated operation points. The normalized distances for the investigated operation points (see Figure 3.45) are summarized in Table 3.2. In this table can be seen that e.g. the normalized distance between the first pole (p_1) and the first zero (z_1) at the first operation point ($Fqs = 0.88$) is equal to 32.531, the normalized distance between the first pole (p_1) and the second zero (z_2)

Table 3.2: Extended Greitzer pole1,2-zeros normalized distances

z_1 [a]		Fqs		Fqs	
	pole	0.88	0.96	1.60	2.60
	p_1 [b]	32.531	8.393	-0.136	30.327
	p_2	-0.178	1.750	-0.353	-0.806

z_1		Fqs		Fqs	
	pole	0.88	0.96	1.60	2.60
	p_1	-0.020	-0.214	-0.986	-0.780
	p_2	-0.976	-0.770	-0.989	-0.999

z_1		Fqs		Fqs	
	pole	0.88	0.96	1.60	2.60
	p_1	170.800	45.178	3.593	164.221
	p_2	3.211	12.518	2.437	0.022

---

[a] z1: first zero

[b] p1: first pole

In Appendix D the normalized distances at different operation points is presented for the first two poles and the first zero in the upper two rows of Figure D.1. The normalized distances for the same poles and operation points but for the second zero are plotted in the upper two rows of Figure D.2, and the first two poles with the third pole in the upper two rows of Figure D.3.

We can conclude from Table 3.2 that for low mass flows ($Fqs \in \{0.88, \ldots, 0.96\}$) the normalized distances between the first and second pole in combination with the second zero, are small. Furthermore, for these mass flows the normalized distance between the first pole and the second zero is small.

② extended Greitzer normalized distance; third pole

For the third extended Greitzer system poles, the compressor map is divided by one subarea, see Figure 3.46

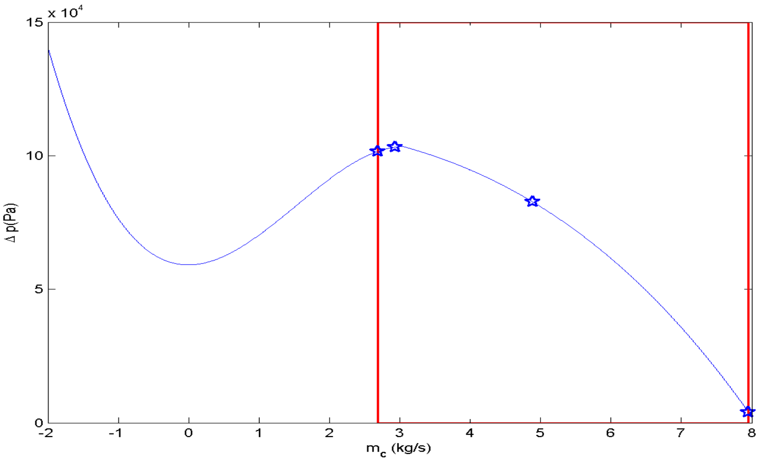

Figure 3.46: Compressor map for d_{nor}

The third pole is strictly real, this is indicated in the compressor map by solid lines that mark the area where the poles are strictly real. The investigated operation points from the area where the first and second pole are strictly real, are maintained for the third pole and marked by the star signs in Figure 3.46. The normalized distances for the third pole and all zeros are summarized in Table 3.3.

Table 3.3: Extended Greitzer normalized distance third pole and zeros.

z_1		Fqs		Fqs	
	pole	0.88	0.96	1.60	2.60
	p_3	-0.261	-0.145	59.898	141.208
z_2		Fqs		Fqs	
	pole	0.88	0.96	1.60	2.60
	p_3	-0.978	-0.928	-0.006	-0.001
z_3		Fqs		Fqs	
	pole	0.88	0.96	1.60	2.60
	p_3	2.787	3.204	322.647	749.024

In Appendix D, the data from Table 3.3 is also shown; in the third row of Figure D.1, Figure D.2 and Figure D.3. It can be concluded from Table 3.3 that in the low mass flow area ($Fqs \in \{0.88, \ldots, 0.96\}$) small normalized distances exist between for the third pole in combination with the first and second zero.

The normalized distances between the poles and zeros have been quantified. We can conclude from these normalized distances that, in the low mass flow area ($Fqs \in \{0.88, \ldots, 0.96\}$), small normalized distances exists between the first two extended Greitzer system poles and the second zero. Furthermore, the normalized distance between the third pole and first zero and the normalized distance between the third pole and second zero are small.

3.2.6 Conclusion extended Greitzer

Regarding the test done for the extended Greitzer model we conclude the following.

Extended Greitzer operation point variations

It can be concluded from the operation point variations that the system poles are complex around the operation point that is marginally stable (i.e. $Re(z) = 0 \wedge Im(z) \neq 0$). The area where the system poles are complex, is equal to 64% of the total chosen operation area ($\dot{m}_c \in \{2.6914 \ldots 7.9517\}$). The area where the system poles are complex can be divided into;

- the area where the system poles are complex and unstable, equal to 7% of the total chosen operation area.
- the area where the system poles are complex and stable, equal to 57% of the total chosen operation area.

The operation area where the system poles are stable, $Re(z) < 0$ is equal to 77% of the total chosen operation area.

Extended Greitzer numerical system pole analysis

From the numerical extended Greitzer system pole analysis can be concluded that the operation point is marginally stable (i.e. $Re(z) = 0 \wedge Im(z) \neq 0$) on the surge line.

Extended Greitzer model parameter variation

It can be concluded from the γ-parameter variations that when the dynamic viscosity decreases (as a result of a decrease of the kinematic viscosity), the damping of the compressed medium decreases, resulting in a decrease of imaginary parts of the system poles. The size of the area where the system poles are complex (Im(z)≠0) is dependant of the γ-parameter value. Furthermore for the investigated operation points, the γ-parameter value influences the location of the real part of the system poles, i.e. at increasing value of γ all eigenvalues shift towards the RHP.

Extended Greitzer normalized distance between pole and zero

We can conclude from these normalized distances that, in the low mass flow area ($Fqs \in \{0.88, \ldots, 0.96\}$), small normalized distances exists between the first two extended Greitzer system poles and the second zero. A smal normalized distance could mean that the dynamical behavior of the pole can be canceled by the zero. Furthermore, the normalized distance between the third pole and first zero and the normalized distance between the third pole and second zero are small.

3.3 Conclusion Greitzer versus extended Greitzer model

From all analyses done for the Greitzer model and for the extended Greitzer model the following can be concluded.

(1). The operation area where the system poles are stable (Re(z)<0) is equal to 79% of the total chosen operation area ($Fqs \in \{0.88, \ldots, 2.60\}$) for the Greitzer model, the operation area where the extended Greitzer system poles are stable is equal to 77% of the total chosen operation area.

We conclude that the operation area where the system poles are stable is larger for the Greitzer model then for the extended Greitzer model. The difference in stable area's can be explained by the differences in marginally stable operation point (i.e. $\Re(z) = 0 \wedge \Im(z) \neq 0$). The Greitzer marginally stable operation point differs 0.75% compared to the extended Greitzer marginally stable solution, this can be the result of inaccurate modeling. The extended Greitzer model uses several assumptions for parameter values ($C, \delta_s, \alpha_r, \tau$) that may not be accurate.

(2). The area where the Greitzer system poles are complex (i.e. $Im(z) \neq 0$) and unstable is equal to 21% of the total chosen operation area ($\dot{m}_c \in \{2.6914 \ldots 7.9517\}$), the area where the extended Greitzer system poles are complex and unstable is equal to 7% of the total chosen operation area.

We can conclude that the area where the system poles are complex and unstable is larger for the Greitzer model then for the extended Greitzer model. This can be explained by the fact that in the third equation of the extended Greitzer model (3.23), the kinematic viscosity is modeled. Because of this damping of the compressed medium is modeled, resulting in a decrease of imaginary parts of the system poles.

(3). We can conclude from the normalized distances between pole(s) and zero(s) in the compressor operation area for low mass flows ($Fqs \in \{0.88, \ldots, 0.96\}$) that the normalized distances for the Greitzer model do not exist. For the extended Greitzer model some normalized distances (i.e. between third pole in combination with the first and second zero, and the first two extended Greitzer system poles and the second zero) are small and therefore the dynamical behavior of the pole(s) can be canceled by a zero.

The third equation of the extended Greitzer model is a physical interpretation of the difference between the exact wall shear stress and the quasi-static wall shear stress. Two parameters C and τ used is this equation are difficult to determine for the compression system and a significant deviation occurs between the simulated and analytically derived parameters [4]. This difference can be brought about by some assumptions (such as the assumption for the boundary thickness, the fluid viscosity and the relaxation time) that were made by Meuleman. From the analyses done in this chapter, it becomes clear that the dynamics of the extended Greitzer model differ in comparison to the dynamics of the Greitzer model. Furthermore, from the extended Greitzer normalized distance analysis it becomes clear that the third extended Greitzer system pole is largely canceled by the system zeros.

On basis of the model assumptions and the normalized distances we conclude that the extended Greitzer model does not seem to be an improvement in comparison to the Greitzer model for a compressor model. Therefore the Greitzer model will be chosen as the compressor model for the remainder of this thesis.

Chapter 4

Model validation

In this chapter we discuss the validation of the Greitzer model with measurement data from an experimental setup. First, we briefly discuss the method of model validation and the used approach for matching simulation results with experimental data. Then we present the validation results from four different experiments. After summarizing these results we end with some conclusions.

4.1 Method of model validation

The validation of the Greitzer model is done by investigating its capability to predict the surge behavior of the experimental setup (Appendix B). Because reliable mass flow measurements are not available during surge, we will focus on the pressure difference only. Graphs are plotted of both measured and simulated pressure difference signals to make a qualitative comparison between both signals. Furthermore, a residu between the two signals is calculated to give a more quantitative indication of the similarity between measurement and model prediction. Finally, the measured, simulated and residu signals are compared in the frequency domain by calculating the power spectral densities of the various signals.

The validation approach consists of the following steps:

- measure and simulate the pressure difference signal during surge
- match signals by tuning compressor duct length and shifting time base
- compare measured and simulated signals in time domain
- analyse residu signal in time and frequency domain
- compare surge amplitude and frequency in measured and simulated signals

4.2 Validation data

The experimental setup for which the Greitzer model is validated, is described in Appendix B. The setup is equipped with numerous temperature probes and static pressure transducers. A dedicated data-acquisition and control system is used for operating the installation, converting and recording sensor outputs, and for online monitoring. The sample time for all static measurements is 6 seconds. Additional dynamic pressure transducers were installed in the suction and discharge pipes to measure the pressure rise fluctuations during experiments. All dynamic pressure signals were measured at a sampling rate of 1.28 kHz [24].

Measurements are done on the setup to determine the steady-state compressor map of the compressor, see Figure B.3. The throttle characteristics are obtained from [?] where appropriate data from the valve manufacturers is used. The various model parameters are obtained from construction drawings where possible. However, some model parameters cannot be determined from the geometry of the compression system directly, e.g. the compressor duct length. This compressor duct length is chosen to be the length that the flow travels from the inlet of the compressor to the inlet of the volute. The former choice is done under the assumption that this is the length in which the largest part of the pressure build-up takes place. The contribution to the pressure rise from the inlet to the outlet of the volute only measures 0.5% of the total pressure rise [4]. In literature the compressor duct length L_c is used as a tuning parameter to match the simulation results with measurements, see for example [13, 4, 16].

For the investigated experimental setup, the compressor duct length was estimated to be 1.45 m. This value is used as an initial value in the iterative method to match simulation results with actual measurements by tuning L_c. Furthermore, the time base of the simulation is adjusted to the experimental data to compensate for phase differences between measured and simulated data. The tuning scheme minimizes the Integral Squared Residu (IQR) of the residu signal $e(kTs) = \Delta p(kT_s) - \Delta p_{\text{sim}}(kT_s)$ with $k = 0, 1, 2, \ldots, N$, according to

$$\arg\min \sum_{k=0}^{N} \left(\Delta p(kT_s) - \Delta p_{\text{sim}}(kT_s, L_c)\right)^2 \tag{4.1}$$

Minimization is achieved by adjusting the value of L_c:

- when $IQR_{m+1} > IQR_m$ then L_c is enlarged
- when $IQR_{m+1} < IQR_m$ then L_c is reduced

where $m = 1, 2, \ldots$ is the iteration number. The enlargement/reduction step is initially coarse (±0.1) for each iteration when IQR_{m+1} is equal to IQR_m, the enlargement/reduction step is refined by a factor ten. The iteration is stopped when tolerance (1e-5) is met between the difference of IQR_{m+1} and IQR_m.

In the following subsection we compare simulated and measured results for four different experiments. The first two experiments were conducted at a compressor speed of 9,000 rpm while the third and fourth measurements were done at 12,000 rpm.

4.2.1 Simulation and experiment 1

In the upper part of Figure 4.1 both simulation and experimental results, for an experiment at 9,000 rpm, are shown.

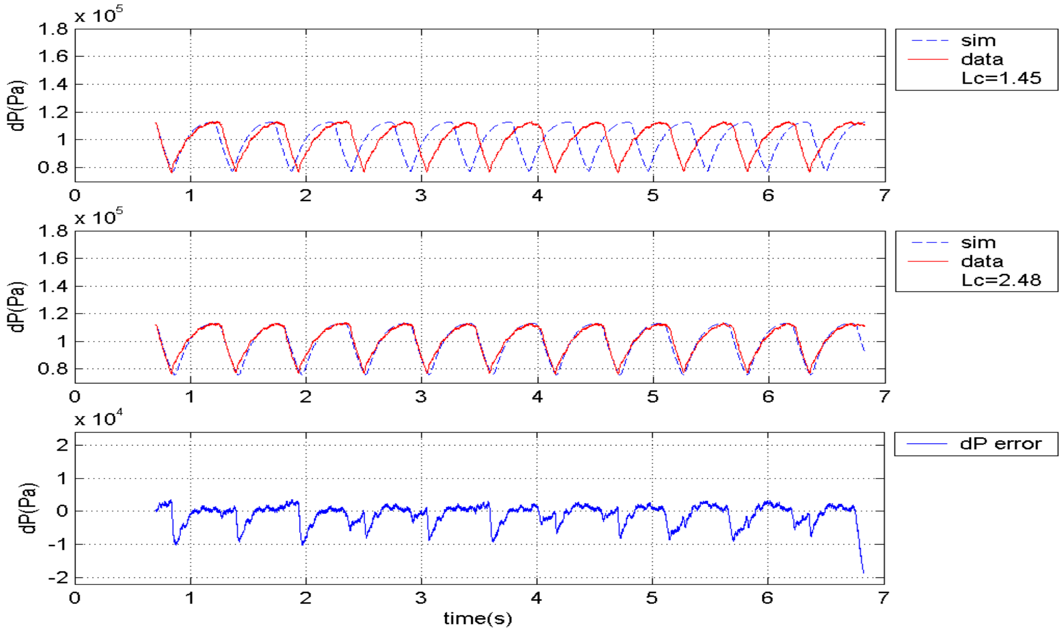

Figure 4.1: Simulated and experimental results, experiment 1

The simulated pressure difference is obtained by using the initial value $L_c = 1.45$ m and the period time difference between the simulated and measured signals is evidently present. The IQR is equal to $1.38 \cdot 10^9$ for this case. After tuning L_c to get a better match between simulated and measured data the middle plot of Figure 4.1 is obtained. From this plot we can see that with the corresponding $L_c = 2.479$ m the simulated and measured signals match, yielding an IQR of $4.51 \cdot 10^7$.

The lower plot of Figure 4.1 shows the residual signal $e(kT_s)$. From this plot we can see that the largest error manifest around the points where the pressure difference is minimal. In Figure 4.2 this observation is illustrated in more detail. This figure shows the simulated mass flow and pressure rise, the matched experimental and simulated pressure rise, and the quadratic residue $e^2(kT_s)$. The vertical lines indicate the instants where flow reversal occurs during the simulation. We now see that the quadratic residue shows distinct peaks around the time instants where the mass flow changes from back flow to normal flow. When we again look at the middle plot of Figure 4.2 we see around the instants of flow reversal:

a). the simulated pressure rise is less steep than the measured pressure rise;

b). in the simulation the minimum Δp during the experiment is lower than the minimum Δp.

These observation will be explained at the end of this chapter.

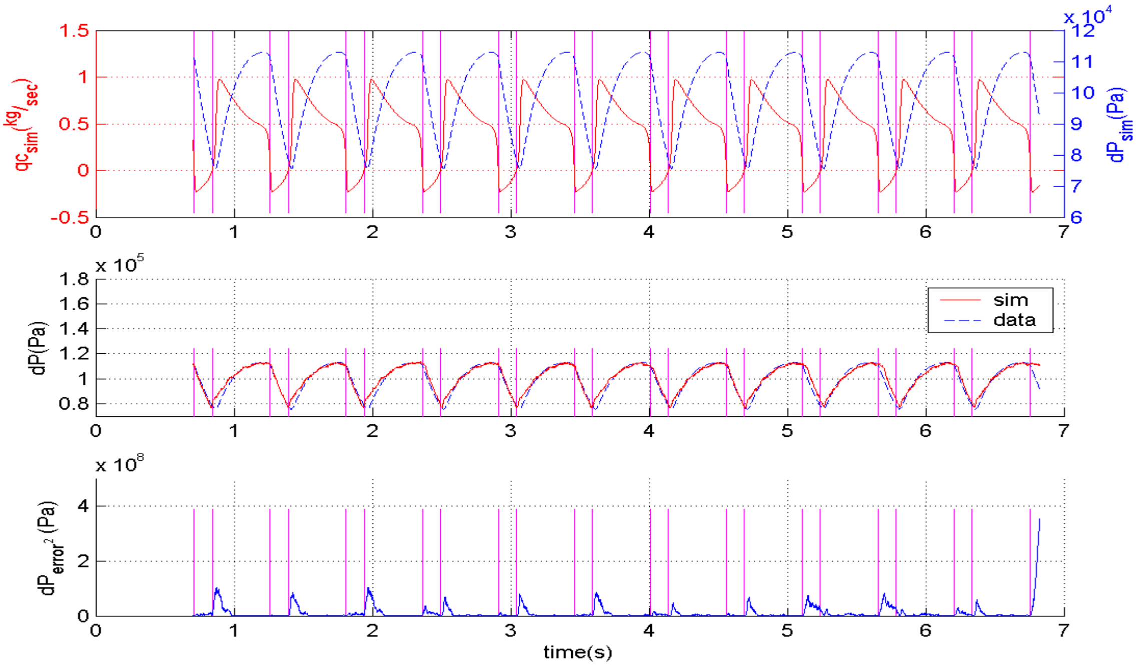

Figure 4.2: Simulated and experimental results ($L_c = 2.479$)

The residue from the simulated and experimental results can contain information that is not immediately visible. Therefore, to extract this information the power spectral density (PSD) of the residue is investigated, see Figure 4.3. From this figure we see a distinct peak at 39 Hz and the higher harmonics 78, 117, ... Hz.

In order to evaluate how good the model predicts the surge frequency, the power spectral density of both the simulated and measured pressure difference is computed. From Figure 4.4 we see that the simulated and measured surge frequencies are similar, namely 1.46 Hz. However, the spectral density amplitudes of the simulated and measured signal differ by 27%. Furthermore, we point out that above the second harmonic of the surge frequency the two spectral densities start to deviate significantly.

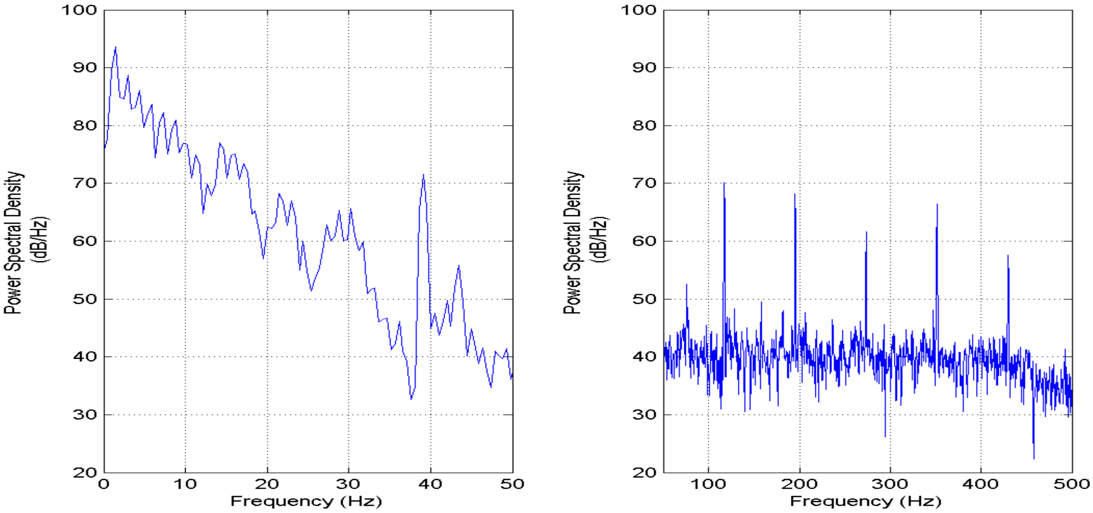

Figure 4.3: Residu Power Spectrum analysis, experiment 1

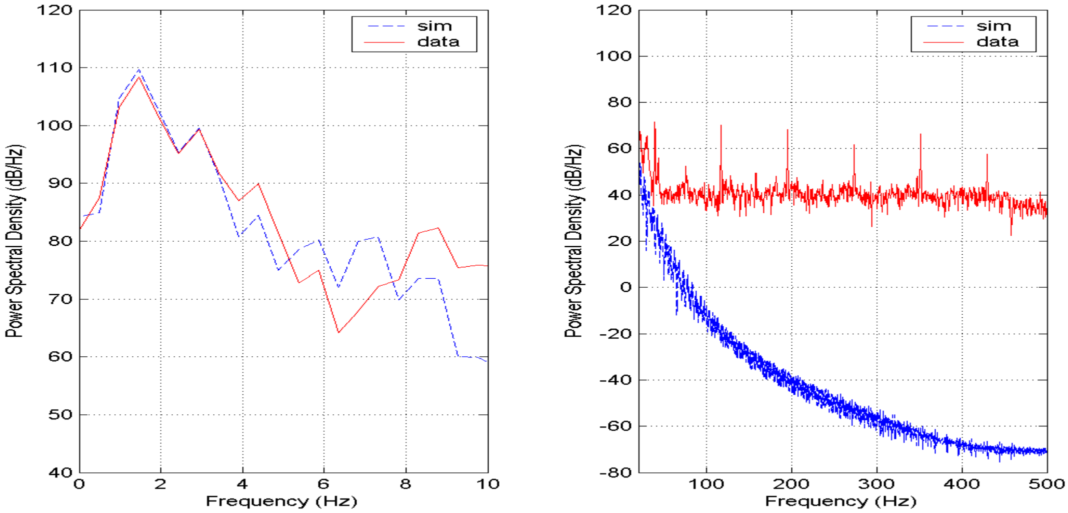

Figure 4.4: Power Spectrum analysis, experiment 1

4.2.2 Simulation and experiment 2

A similar analysis was done for another experiment at the same rotational speed of 9,000 rpm to investigate if the observed phenomena are repeatable. For the initial value $L_c = 1.45$ m the IQR value was $6.97\dot{1}0^8$ while tuning resulted in an $L_c = 2.134$ m and a corresponding IQR of $9.93 \cdot 10^7$. The surge frequency is again equal to 1.46 Hz in both the simulation and the experiment. Figures of the various results are given in Appendix E.

Compared with the first experiment we observe a slightly worse match between simulation and experiment after tuning L_c. The amplitude difference in the spectral densities is equal to 23%. In order to investigate whether the observed phenomena are speed dependant, the analysis is repeated for two experiments at $12,000$ rpm.

4.2.3 Simulation and experiment 3

In Figure 4.5 the results are shown for an experiment at a rotational speed of $12,000$ rpm. With the initial value for L_c an IQR of $4.92 \cdot 10^8$ was obtained. After tuning L_c to 1.755 m the IQR became $1.31 \cdot 10^8$. The following remarks can be made about the results for this particular measurement:

a). the simulated pressure rise is less steep than the measured pressure rise;

b). the minimum Δp during the experiment is lower than the minimum Δp in the simulation;

c). the maximum Δp during the experiment is lower than the maximum Δp in the simulation.

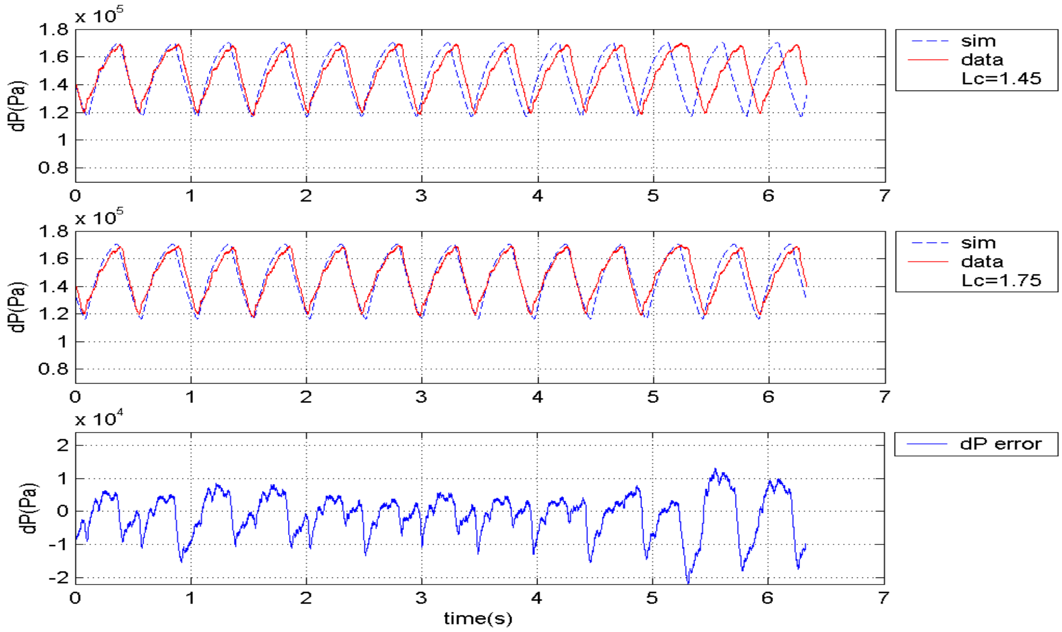

Figure 4.5: Simulated and experimental results, experiment 3

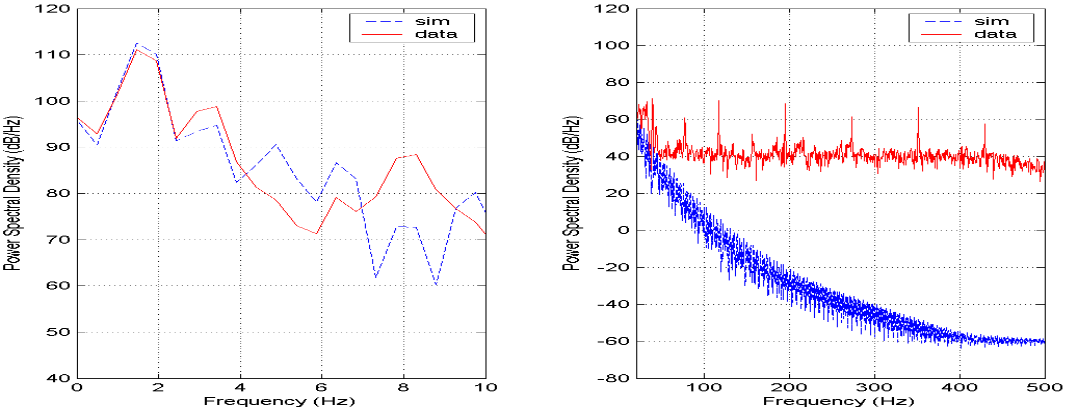

Figure 4.6: Power Spectrum analysis, experiment 3

We point out that the match between simulation and experiment is good during the parts where the pressure difference decreases. From the spectral density plots in Figure 4.6 we observe that the peaks at 39 Hz and its higher harmonics are also present in the measured signal for this experiment. The surge frequency is again equal to 1.46 Hz in both the simulation and experiment. The amplitude difference in the spectral densities is equal to 29%.

4.2.4 Simulation and experiment 4

Again another experiment at the same rotational speed of 12, 000 rpm is done here to investigate if the observed phenomena are repeatable. Figures of the various results are given in Appendix E. With the initial value for L_c an IQR of $3.36 \cdot 10^8$ was obtained. After tuning L_c to 1.45 m the IQR became $8.90 \cdot 10^7$. A good match is obtained for the pressure rise decreases for the simulated and experimental data. The same remarks about pressure rise, minimum Δp and maximum Δp differences between simulation and experiment as given in Section 4.2.3 apply to test 4.

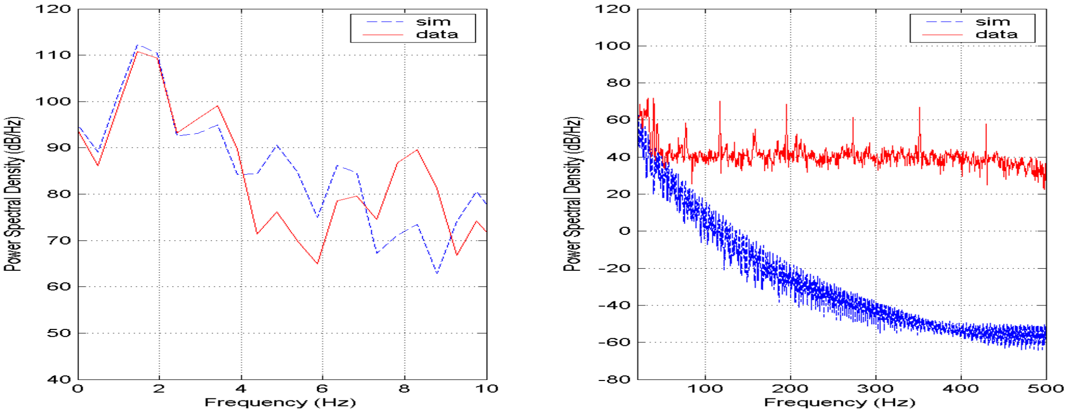

Figure 4.7: Power Spectrum analysis, experiment 4

As with the other experiments, the peaks at 39 Hz and its higher harmonics are present in the residual signal as shown in Figure 4.7. The surge frequency is again equal to 1.46 Hz in both the simulation and experiment. The amplitude difference in the spectral densities is equal to 29%.

4.2.5 Discussion of results

The model validation is done using four different experiments, at two rotational speeds. Subsequently, we compared the separately experiments with simulation results and used an iterative algorithm to match the simulated and experimental data, using L_c as a tuning parameter. The results of these experiments are summarized in Table 4.1.

Table 4.1: Model validation summary

Experiment	N (rpm)	Original		Matched	
		L_c (m)	IQR	L_c (m)	IQR
1	9,000	1.45	$1.38 \cdot 10^9$	2.479	$4.51 \cdot 10^7$
2		1.45	$6.97 \cdot 10^8$	2.134	$9.93 \cdot 10^7$
3	12,000	1.45	$4.92 \cdot 10^8$	1.755	$1.31 \cdot 10^8$
4		1.45	$3.36 \cdot 10^8$	1.585	$8.90 \cdot 10^7$

The results of surge frequencies and magnitudes, arranged per experiment and simulation are summarized in Table 4.2.

Table 4.2: Surge model validation summary

Experiment	N (rpm)	Experimental		Simulated		Difference experiment and simulation
		f*[a]	A*[b]	f*	A*	
1	9,000	1.46	$6.80 \cdot 10^{10}$	1.46	$9.33 \cdot 10^{10}$	27%
2		1.46	$6.97 \cdot 10^{10}$	1.46	$9.09 \cdot 10^{10}$	23%
3	12,000	1.46	$1.28 \cdot 10^{11}$	1.46	$1.80 \cdot 10^{11}$	29%
4		1.46	$1.21 \cdot 10^{11}$	1.46	$1.70 \cdot 10^{11}$	29%

---

[a] f*: surge frequency

[b] A*: surge amplitude

The compressor duct length is chosen to be the length that the flow travels from the inlet of the compressor to the inlet of the volute. The four experiments show that the matched L_c values are different for both rotational speeds, therefore assuming $L_c = L_c(N)$. If this is true, the chosen concept for L_c must be reformulated.

Form results it is evident that the largest deviation between the simulated and experimental signals originates around the reversal from backflow to normal flow. For the greater part these deviations originate after the reversal back to normal flow, but also some occur during backflow [21]. These deviations are caused by the fact that the simulated and experimental results of the pressure rise decrease match good but the simulated pressure rise is less steep than the measured pressure rise.

During surge the pressure rise differences between simulation and measurement for the transition from the compressor characteristic in the positive mass flow region to the compressor characteristic in the negative mass flow region is small. The pressure rise differences between simulation and measurement for the transition from the compressor characteristic in the negative mass flow region to the compressor characteristic in the positive mass flow region are large.

These differences can be caused by the assumption of incompressible flow in the ducts. This assumption has little influence on the first transition as described above (transition from compressor curve in positive mass flow region to compressor curve in negative mass flow region) because of the high pressure involved at this transition. The incompressibility assumption seems to manifest itself at the other transition (negative to positive mass flow) where the deviation between simulation and experiment is great. The area of interest however, is around the surge line so therefore the great deviation linked to this transition is of less significance.

Furthermore, the 39 Hz peaks (and the higher harmonics 78, 117, ... Hz) shown in the residu signals, do not to be dependent on rotational speed. The rotational independency of these peaks suggests that it is a phenomenon that is not caused by the compressor. Therefore, it could be related to the piping system, i.e. acoustical effects in the suction or discharge piping.

Finally the simulations seem predict the surge frequency very well. However, the amplitude of the plenum pressure oscillations do not seem to match for simulations and experiments. For higher harmonics the amplitude match of the plenum pressure oscillations becomes even worse. According to [9] the amplitude of the plenum pressure oscillations is strongly depend on the shape of the compressor characteristic and the occurring surge type ; plenum pressure oscillations during classic surge are seen to be smaller than for deep surge. An improvement of simulated and measured amplitude of the plenum pressure rise oscillations can be achieved by moving the valley point $\Psi_c(0)$ (Appendix B) without changing the measured part of the compressor characteristics $\Psi(\phi_c)$. Of course the whole unstable part of the compressor curve is a wild guess, a possible solution can be found in [18].

4.3 Conclusion model validation

The overall match of the Greitzer model with experimental data is good, indicating that the model is usable for describing the surge behavior of the experimental setup. From Table 4.2 it can be concluded that the surge frequency is correctly predicted by the model when L_c is tuned properly. However, some differences between simulated and measured data was observed, in particular around the time instances where flow reversal occurred. The difference between simulated and measured minimum pressure difference explains the differences in the surge amplitudes, see Table 4.2.

A possible explanation for the differences during flow reversal is the questionable incompressibility assumption for the medium in the compressor duct. The ignored terms involving the time-rate-of-change of mass in the ducting may amount to significantly to the terms retained. However, the time periods, during which the ignored terms are significant, are short and this may explain why the model results are still useful [21]. Another explanation for the differences between simulations and measurements may be the assumed shape of the quasi-static compressor curve [3].

From the spectral analysis of the residu signals, distinct peaks were found that appear to be independent of compressor rotational speed. Possibly, these peaks are caused by acoustic phenomena in the compressor pipe system but the effect of acoustics on the dynamic behavior is still unknown. Given their relatively high frequencies with respect to the surge frequency, neglecting acoustic effects may not cause large problems for active surge control but further investigations are recommendable. We point out that the observed peaks occur at frequencies of the same order as those of rotating stall.

The Greitzer model is suitable for usage in the design of active surge controllers because the amplitudes of the pressure difference and the surge frequency are predicted with sufficient accuracy. From our analysis it has become evident that the huge simplifications (incompressible flow, no effect of connected piping) cannot be entirely neglected and require future attention.

Chapter 5

Conclusions and Recommendations

The objective of this research was to investigate what type of compressor model is most suitable for describing the dynamics of a centrifugal compressor system for active surge control. From literature various models are available and a motivated selection of four specific models (the Greitzer model, the extended Greitzer model, Spakovszky model I and Spakovszky model II) was made. The benefits and advantages of these models were described, followed by a detailed parameter study for the Greitzer model and the extended Greitzer model. Finally, the Greitzer model was validated with measurement data from an experimental centrifugal compressor setup.

5.1 Conclusions

Based on the findings reported in this thesis, the following conclusions can be made:

- the models proposed by Spakovszky are sophisticated two-dimensional flow models for describing both surge and rotating stall in centrifugal compressors;
- some assumptions made in the derivation of the extended Greitzer model are questionable and the added dynamics have a very limited influence due to pole-zero cancelation;
- the overall match of the Greitzer model and experimental data is good, although differences are observed, in particular during and after the occurrence of flow reversal;
- of the investigated models the Greitzer model is most suitable for describing the dynamics of a centrifugal compressor.

5.2 Recommendations

Based on the research presented in this thesis, the following recommendations for future research can be given:

- implement dynamic mass flow measurements for model identification and validation since in all investigated models the compressor mass flow appears as a separate state;
- investigate the effect of model uncertainties, for example the shape of the compressor curve and the incompressible flow assumption for the compressor duct, on the achievable extension of the stable operating region by means of active surge control;
- investigate the effect of acoustics on the dynamic behavior of a centrifugal compression system;
- investigate the benefits of two-dimensional flow models, for example the models proposed by Spakovszky, in particular when the effect of rotating stall on active surge stabilization is considered.

Bibliography

[1] Leonessa A. and Li H. Haddad, W. Globally stabilizing switching controllers for a centrifugal compressor model with spool dynamics. *Transactions on control systems technology*, 8:474–482, May 2000.

[2] Stenning A.H. Rotating stall and surge. *Chapter 15 in ASME Lecture course in fluid dynamics of turbomachinery*, August 1973. Iowa State University.

[3] R. de Lange C. Meuleman and A. van Steenhoven. Surge dynamics in a centrifugal compressor system. In *Proc. 3rd European Conference on Turbomachinery Fluid Dynamics and Thermodynamics*, pages 895–904, Manchester, United Kingdom, March 1999.

[4] Meuleman C.H.J. *Measurement and unsteady flow modelling of centrifugal compressor surge.* Phd thesis, Technische Universiteit Eindhoven, Eindhoven, the Netherlands, October 2002.

[5] Jager. B. de. Rotating stall and surge control: A survey. In *Poceedings 34th conf. on Decision&Control*, pages 1857–1862, New Orleans, LA, December 1995.

[6] Liaw Der-Cherng, Ren Sing-Ming, Chung Wen-Ching, and Abed H. Eyad. Surge control of axial flow compression systems via linear and nonlinear designs. In *Proceedings of the American Control Conference*, pages 4347–4352, Anchorage, AK, May 2002.

[7] Gysling D.L., Dugundji J, Greitzer E.M., and A.H. Epstein. Dynamic control of centrifugal compressor surge using tailored structures. *Transactions of the ASME*, 113:710–722, October 1991. Cambrigde, MA.

[8] Greitzer E.M. Surge and rotating stall in axial flow compressors. *Transactions of the ASME*, pages 190–198, April 1976.

[9] Willems F. *Modeling and bounded feedback stabilization of centrifugal compressor surge.* Phd thesis, Technische Universiteit Eindhoven, Eindhoven, the Netherlands, April April. pag 2,6,31.

[10] Moore F.K. A theory of rotating stall of multistage axial compressors. *ASME Journal of Engineering for Gas Turbines and Power*, 106:313–320, April 1984.

[11] Moore F.K. and Greitzer E.M. A theory of post stall transients in axial compression systems: Part i - development of equations. *Transactions of the ASME*, pages 68–75, January 1986. Cambridge, MA.

[12] Billoud G. and Galland M.A. Adaptive active control of instabilities. *Journal of intelligence materials,systems and structures*, 2:457–471, October 1991.

[13] Arnulfi G.L., Giannattasio P., Giusto C., Massardo A.F., Micheli D., and Pinamonti P. Multistage centrifugal compressor surge analysis part ii - numerical simulation and dynamic control parameters evaluation. *Journal of turbomachinery*, 121:312–320, April 1999.

[14] Emmons H.W., Pearson C.E., and H.P. Grant. Compressor surge and stall propagation. *Transactions of the ASME*, 77:455–469, April 1995.

[15] Day I. Stall inception in axial flow compressors. *ASME Journal of Turbomachinery*, 115(1):1–9, January 1993.

[16] Ffowcs Williams J.E., Harper M.F.L., and Allwright D.J. Active stabilization of compressor instability and surge in a working engine. *Transactions of the ASME*, 115:68–75, January 1993. Cambridge, United Kingdom.

[17] Simon J.S., Valavani L., Epstein A.H., and Greitzer E.M. Evaluation of approches to active compressor surge stabilization. *Journal of turbomachinery*, 115:57–67, January 1993.

[18] Gravdahl J.T. Modeling of surge in free-spool centrifugal compressor: experimental validation. *Journal of propulsion and power*, 20(5):849–857, September-October 2004.

[19] Gravdahl J.T., Egeland O., and Vatland S.O. Drive torque actuation in active surge control of centrifugal compressor. *Automatica*, 38(38):1881–1893, January 2002.

[20] I.J. Karassik. *Pump handbook*. McGraw-Hill, London, 1976.

[21] Hansen K.E. Experimental and theoretical study of surge in a small centrifugal compressor. *Journal of Fluids Engineering*, 103:391–395, September 1981.

[22] Aungier R.H. *Axial flow compressors - A strategy for aerodynamic design and analysis*. ASME Press and Professional Engineering Publishing Limited, New York, NY and Bury St. Edmunds, Suffolk, 2003.

[23] Sastry S. *Nonlinear systems - Analysis,Stability, and Control*. Springer, New York, USA, 1999.

[24] Helvoirt. J. van. Modeling and identification of centrifugal compressor dynamics with approximate realizations. In *Poceedings of the 2005 IEEE Conference on Control Applications*, pages 1441–1447, Toronto, Canada, August 2005.

[25] Wal M. van der, Willems F., and Jager B. de. Selection of actuators and sensors for active surge control. In *Poceedings of the 1997 IEEE International Conference on Control Applications*, pages 121–126, Hanford, CT, October 1997.

[26] Spakovszky Z.S. *Application of axial and radial compressor dynamic system modeling*. Phd thesis, Massachusetts Institute of Technology, Cambrigde, United States, February 2001.

Appendices

Appendix A

Tables

A.1 Greitzer operation point variation table

Table A.1: Greitzer Fqs and mass flow variation

Test case	Fqs	Mass flow [$^{kg}/_{s}$]
A_{Gz1}	0.88	2.6914
A_{Gz2}	0.89	2.7219
A_{Gz3}	0.90	2.7525
A_{Gz4}	0.91	2.7831
A_{Gz5}	0.92	2.8137
A_{Gz6}	0.93	2.8443
A_{Gz7}	0.94	2.8749
A_{Gz8}	0.95	2.9054
A_{Gz9}	0.96	2.9360
A_{Gz10}	0.97	2.9666
A_{Gz11}	0.98	2.9972
A_{Gz12}	0.99	3.0278
A_{Gz13}	1	3.0493
A_{Gz14}	1.01	3.0889
A_{Gz15}	1.02	3.1195
A_{Gz16}	1.03	3.1501
A_{Gz17}	1.04	3.1807
A_{Gz18}	1.05	3.2113
A_{Gz19}	1.06	3.2419
A_{Gz20}	1.07	3.2724
A_{Gz21}	1.08	3.3030
A_{Gz22}	1.09	3.3336
A_{Gz23}	1.10	3.3642
A_{Gz24}	1.11	3.3948
A_{Gz25}	1.12	3.4254
A_{Gz26}	1.13	3.4559
A_{Gz27}	1.14	3.4865
A_{Gz28}	1.15	3.5171
A_{Gz29}	1.16	3.5477
A_{Gz30}	1.17	3.5783
A_{Gz31}	1.18	3.6089
A_{Gz32}	1.19	3.6394
A_{Gz33}	1.20	3.6700
A_{Gz34}	1.21	3.7006
A_{Gz35}	1.22	3.7312
A_{Gz36}	1.23	3.7618
A_{Gz37}	1.24	3.7924
A_{Gz38}	1.25	3.8230
A_{Gz39}	1.26	3.8535
A_{Gz40}	1.27	3.8841
A_{Gz41}	1.28	3.9147
A_{Gz42}	1.29	3.9453
A_{Gz43}	1.30	3.9759
A_{Gz44}	1.40	4.2817
A_{Gz45}	1.50	4.5875
A_{Gz46}	1.60	4.8934
A_{Gz47}	1.70	5.1992
A_{Gz48}	1.80	5.5050
A_{Gz49}	1.90	5.8109
A_{Gz50}	2.00	6.1167
A_{Gz51}	2.10	6.4226
A_{Gz52}	2.20	6.7284
A_{Gz53}	2.30	7.0342
A_{Gz54}	2.40	7.3401
A_{Gz55}	2.50	7.6459
A_{Gz56}	2.60	7.9517

A.2 Meuleman operation point variation table

Table A.2: Meuleman Fqs and mass flow variation

Test case	Fqs	Mass flow $[^{kg}/_{s}]$	Test case	Fqs	Mass flow$[^{kg}/_{s}]$	Test case	Fqs	Mass flow$[^{kg}/_{s}]$
A_{Mm1}	0.88	2.6914	A_{Mm21}	1.08	3.3030	A_{Mm41}	1.28	3.9147
A_{Mm2}	0.89	2.7219	A_{Mm22}	1.09	3.3336	A_{Mm42}	1.29	3.9453
A_{Mm3}	0.90	2.7525	A_{Mm23}	1.10	3.3642	A_{Mm43}	1.30	3.9759
A_{Mm4}	0.91	2.7831	A_{Mm24}	1.11	3.3948	A_{Mm44}	1.40	4.2817
A_{Mm5}	0.92	2.8137	A_{Mm25}	1.12	3.4254	A_{Mm45}	1.50	4.5875
A_{Mm6}	0.93	2.8443	A_{Mm26}	1.13	3.4559	A_{Mm46}	1.60	4.8934
A_{Mm7}	0.94	2.8749	A_{Mm27}	1.14	3.4865	A_{Mm47}	1.70	5.1992
A_{Mm8}	0.95	2.9054	A_{Mm28}	1.15	3.5171	A_{Mm48}	1.80	5.5050
A_{Mm9}	0.96	2.9360	A_{Mm29}	1.16	3.5477	A_{Mm49}	1.90	5.8109
A_{Mm10}	0.97	2.9666	A_{Mm30}	1.17	3.5783	A_{Mm50}	2.00	6.1167
A_{Mm11}	0.98	2.9972	A_{Mm31}	1.18	3.6089	A_{Mm51}	2.10	6.4226
A_{Mm12}	0.99	3.0278	A_{Mm32}	1.19	3.6394	A_{Mm52}	2.20	6.7284
A_{Mm13}	1	3.0493	A_{Mm33}	1.20	3.6700	A_{Mm53}	2.30	7.0342
A_{Mm14}	1.01	3.0889	A_{Mm34}	1.21	3.7006	A_{Mm54}	2.40	7.3401
A_{Mm15}	1.02	3.1195	A_{Mm35}	1.22	3.7312	A_{Mm55}	2.50	7.6459
A_{Mm16}	1.03	3.1501	A_{Mm36}	1.23	3.7618	A_{Mm56}	2.60	7.9517
A_{Mm17}	1.04	3.1807	A_{Mm37}	1.24	3.7924			
A_{Mm18}	1.05	3.2113	A_{Mm38}	1.25	3.8230			
A_{Mm19}	1.06	3.2419	A_{Mm39}	1.26	3.8535			
A_{Mm20}	1.07	3.2724	A_{Mm40}	1.27	3.8841			

A.3 Greitzer parameter variations; ratio $\frac{A_c}{L_c}$

Table A.3: Parameter experiment, ratio $\frac{A_c}{L_c}$

Test	A_c	L_c	$\frac{A_c}{L_c}$
1	$0.2 \cdot A_c$	$6 \cdot L_c$	2.93e-004
2	$0.2 \cdot A_c$	$4 \cdot L_c$	4.39e-004
2	$0.2 \cdot A_c$	$2 \cdot L_c$	8.79e-004
4	$0.4 \cdot A_c$	$1.8 \cdot L_c$	1.95e-003
5	$0.6 \cdot A_c$	$1.6 \cdot L_c$	3.30e-003
6	$0.8 \cdot A_c$	$1.4 \cdot L_c$	5.02e-003
7	A_c	$1.2 \cdot L_c$	7.32e-003
8	$1.2 \cdot A_c$	L_c	1.05e-002
9	$1.4 \cdot A_c$	$0.8 \cdot L_c$	1.54e-002
10	$1.6 \cdot A_c$	$0.6 \cdot L_c$	2.34e-002

A.4 Greitzer parameter variations; V_1

Table A.4: Parameter experiment, V_1

Test	V_1	$\frac{V_1}{V_2}$	Test	V_1	$\frac{V_1}{V_2}$
1	3.2039e-001	1	6	8.9709e+000	28
2	1.9223e+000	6	7	1.0893e+001	34
3	3.8447e+000	12	8	1.2495e+001	39
4	5.4466e+000	17	9	1.4418e+001	45
5	7.3690e+000	23	10	1.6019e+001	50

A.5 Greitzer parameter variations; V_2

Table A.5: Parameter experiment, V_2

Test	V_2	$\frac{V_1}{V_2}$	Test	V_2	$\frac{V_1}{V_2}$
1	3.0693e+000	1	6	1.0962e-001	28
2	5.1155e-001	6	7	9.0273e-002	34
3	2.5577e-001	12	8	7.8699e-002	39
4	1.8055e-001	17	9	6.8206e-002	45
5	1.3345e-001	23	10	6.1386e-002	50

A.6 Meuleman γ variation

Table A.6: Meuleman γ variations

Test	γ	τ	$\frac{h^2}{\nu}$	$\frac{\gamma}{\tau}$
1	0.01	0.0023562	0.6	4.2441
2	0.02	0.0047124	1.2	4.2441
3	0.03	0.0070686	1.8	4.2441
4	0.04	0.0094248	2.4	4.2441
5	0.05	0.011781	3	4.2441
6	0.10	0.023562	6	4.2441
7	0.15	0.035343	9	4.2441
8	0.20	0.047124	12	4.2441
9	0.25	0.058905	15	4.2441
10	0.30	0.070686	18	4.2441
11	0.35	0.082467	21	4.2441
12	0.40	0.094248	24	4.2441
13	0.45	0.10603	27	4.2441
14	0.50	0.11781	30	4.2441
15	0.55	0.12959	33	4.2441

Appendix B

Compressor curve and experimental setup

B.1 Compressor curve

The steady-state compressor curve can be described by the cubic polynomial:

$$\Psi_c(\Phi) = \Psi_{c0} + H\{1 + \frac{3}{2}(\frac{\Phi}{W} - 1) - \frac{1}{2}(\frac{\Phi}{W} - 1)^3\} \tag{B.1}$$

This polynomial is founded in [11] and the notation used in the definition can be visualized in Figure B.1.

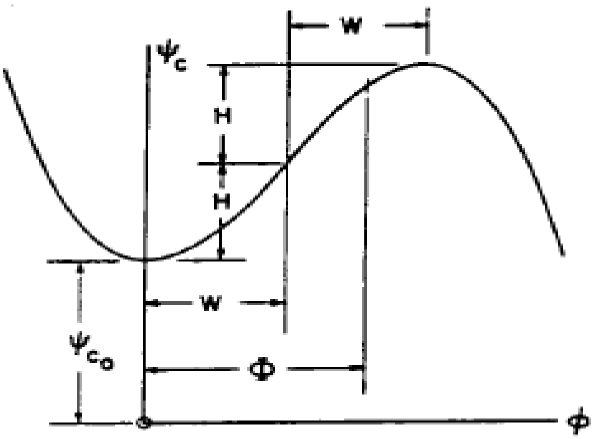

Figure B.1: Compressor curve

According to Figure B.1, e.g. the distance between the valley point Ψ_{c0} and the top of the curve is equal to $2W$. This representation is used in axial compressors by e.g. [11], [19] and in centrifugal compressors by [4]. The parameters Ψ_{c0}, H and W are determined from the steady-state measurements of the compressor curve and from transient data.

B.2 Throttle line

The compression system is modeled as a closed loop system, shown in Figure B.2, can be seen that two valves exist in the system; one large valve and a small (control) valve. The large valve is stationary during simulations and experiment only the small valve is used as an system input.

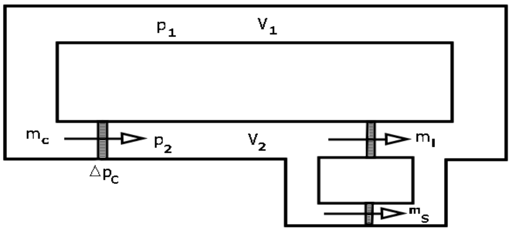

Figure B.2: Compressor model

The model of the compression system contains the throttle characteristics $\dot{m}_l(\Delta p, u_l)$ and $\dot{m}_s(\Delta p, u_s)$. For subsonic flow conditions the small compressor valve mass flow is assumed to be given by (B.2) and (B.3) for the large compressor valve mass flow :

$$\dot{m}_s = c_s u \sqrt{\Delta p} \tag{B.2}$$

$$\dot{m}_l = c_l u \sqrt{\Delta p} \tag{B.3}$$

The constants c_s and c_l are valve specific constants.

B.3 Experimental setup

Experiments were done on an single stage compressor test rig that is normally used to test industrial compressors. The centrifugal compressor is driven by an electric motor that is connected to the shaft through a gearbox. rotational speed can be varied between 8000 and 16000 rpm. Surge experiments are performed for rotational speeds of 9000, 11000, 13000, and 15000 rpm, see Figure B.3.

The compressor operates in a closed circuit that makes it possible to use different pure gases or gas mixtures. Furthermore, this configuration allows for varying the average pressure in the system between 1 and 15 bar. All results presented in this paper were obtained from presented in this paper were obtained from experiments with $\mathcal{N}_2$ gas ($28.0134 \cdot 10^{-3}$ (kg/mol)) and an average suction pressure of 10 bar.

Table B.1: Parameters of the compression system

Element	Parameter	Value	Unit
Impeller	number of blades	17	-
	inlet diam. at casing $d_{1,c}$	0.1592	m
	inlet diam, at hub $d_{1,h}$	0.1450	m
	exit diameter d_2	0.2840	m
	exit width	0.0043	m
Vaned diffuser	number of vanes	10	-
	inlet diameter	0.2870	m
	outlet diameter	0.4409	m
	width	0.0036	m
System	piping volume V_1	3.0693	m^3
	discharge volume V_2	0.3204	m^3
	compressor duct area A_c	0.0034	m^2
	compressor duct length L_c	0.1970	m

Throttling of the compressor is done by means of a butterfly valve. A parallel control valve is used for more precise adjustments of the mass flow rate. The return piping contains a measurement section with a flow straightener, an orifice flow meter, and a gas cooler. With the combination of the throttle, return piping, and cooler, the

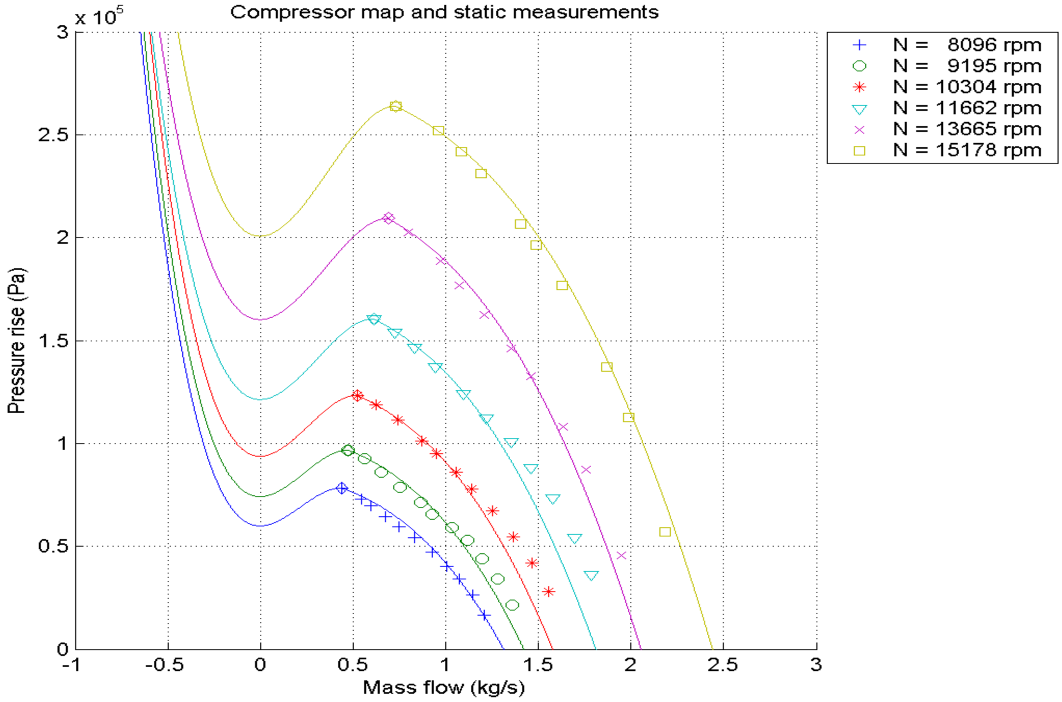

Figure B.3: Compressor curves at different N

conditions of the gas at the compressor inlet, are kept approximately constant. Some characteristics of the installation are summarized in Table B.1. We remark that V2 represents the combined volume of the discharge pipe and the compressor volute. The compression installation is equipped with numerous temperature probes and static pressure transducers to determine the steady-state performance of the compressor. A dedicated data-acquisition and control system is used for operating the installation, converting and recording sensor outputs, and for online monitoring. Additional pressure transducers were installed in the suction and discharge pipes to measure the pressure rise fluctuations during surge. For data-acquisition a SIGLAB system with anti-aliasing filters and AID convertors was used. All dynamic pressure signals were measured at a sampling rate of 5.12 kHz.

Appendix C

Meuleman parameters C' and τ

The Meuleman parameters are acquired out of [4], see Table C.1

Table C.1: Meuleman parameters of the compression system

Parameter	Description	Value	Unit
h	compressor exit width	16.44e-3	m
ν	kinematic viscosity	1.5e-5	m^2/s
α_r	relaxed stokes number	20	

The geometry of the centrifugal compressor produces a complex flow field. Since the parameters C' and τ depend on boundary-layer thickness of the compressor they are difficult to determine in such a flow field. The growth of the boundary-layer in the compressor depends on the flow path through the compressor. First, the flow path through the compressor changes from one frame of reference to another. Second, the flow is curved from axial to radial direction, which introduces secondary flow movement of fluid. Third, there exists an adverse pressure gradient, which quickens the growth of the boundary-layer thickness. Starting from the idea that the compressor can be modeled as a rectangular duct, and a turbulent boundarylayer growth as on a flat plate can be applied, the thickness would increase from zero at the inlet to $\delta_{L_c=0.16}$(m) at the outlet of the compressor. This thickness exceeds the smallest half width at the outlet of the compressor $\frac{h}{2} = 3.5 \cdot 10^{-3}$(m). Therefore, it is assumed that the boundary-layer fluid occupies the whole width at the compressor outlet, i.e., $\delta = \frac{h}{2}$.

The parameters C' and τ depend on the relevant boundary-layer thickness, assuming that the relevant boundary-layer thickness equals the half width of the smallest passage in the compressor the parameters become:

$$
\begin{aligned}
C' &= C{\frac{\delta_s^2}{h/2}}^{2} = 1/60 \\
\delta_s &= \frac{h}{2} \\
\tau &= \frac{2\pi\delta_s^2}{\alpha_r^2\nu} \\
\alpha &= \frac{h}{2}\sqrt{\frac{2\pi f_s}{\nu}}
\end{aligned}
$$

A remark can be made about the modeling difference between the Greitzer model and the extended Greitzer model in combination with the assumptions done for the extended Greitzer model. The marginally stable operation point (i.e. $\Re(z) = 0 \wedge \Im(z) \neq 0$) is slightly different for both model; the operation point where the extended Greitzer system poles are marginally stable is equal to $\dot{m}_c = 3.0331$ kg/s, whereas the operation point where the Greitzer system poles are marginally stable is equal to $\dot{m}_c = 3.0493$ kg/s.

The operation point where the Greitzer system poles are marginally stable differs 0.75% compared to the extended Greitzer marginally stable solution. This difference can be the result of the inaccurate modeling i.e. the extended Greitzer model uses several assumptions for parameter values $(C, \delta_s, \alpha_r, \tau)$ that may not be accurate.

Appendix D

Meuleman normalized distances

The normalized distances of the Meuleman model, as described in Section 3.2.5, for the different system poles in combination with the zeros are given in the figures on the following pages. For all figures in this appendix accounts that the first column of the subfigure array shows relevant system pole/zero data for an $\dot{m}_c = 2.69$(kg/s), the second column for $\dot{m}_c = 2.94$(kg/s), etc. The first row in the subfigure array shows the first system pole (λ_1) and the first zero (z_1) for different operation points, the second row shows the second system pole and the first zero for different operation points, etc.

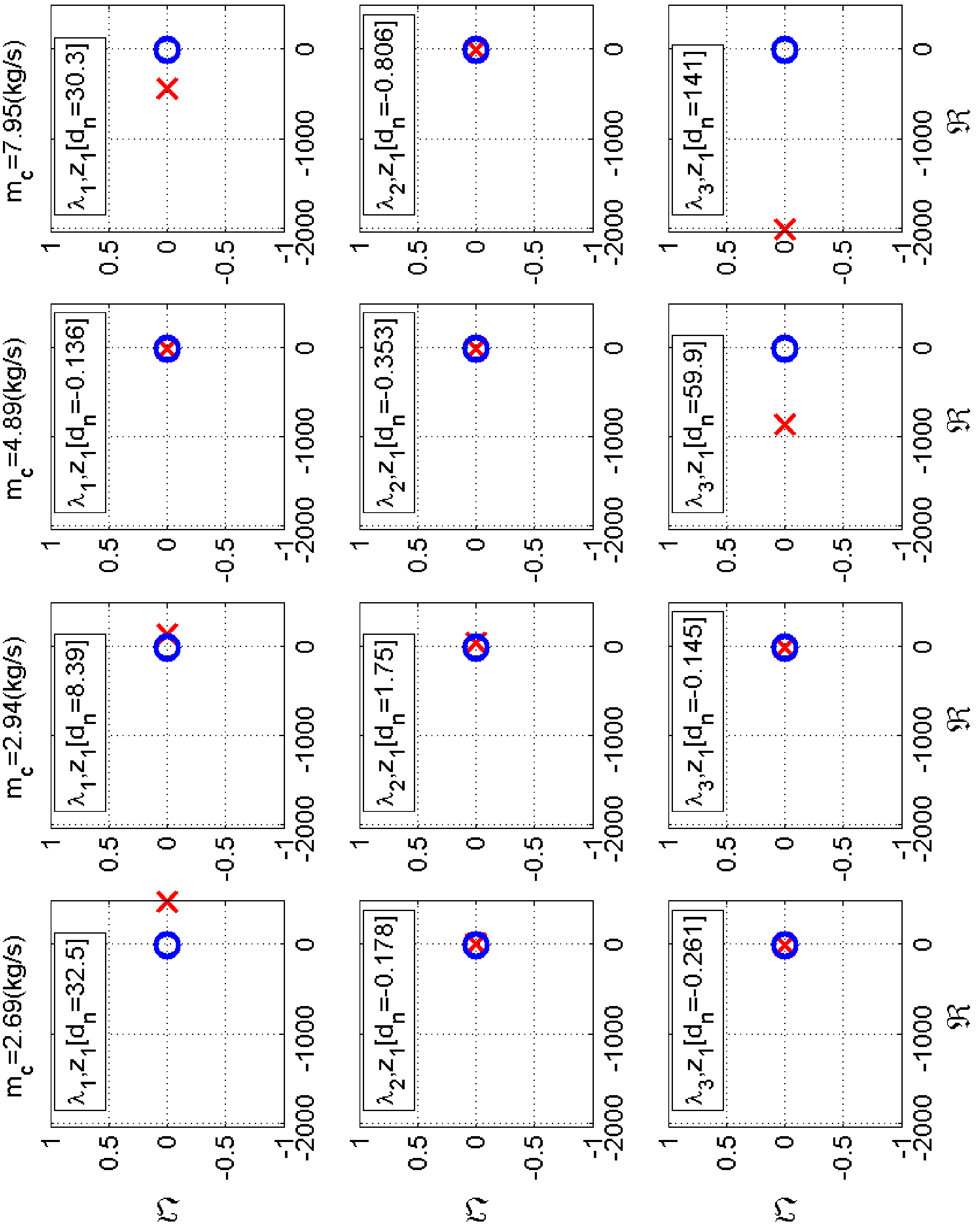

Figure D.1: Normalized distances pole1,pole2,pole3 and zero1

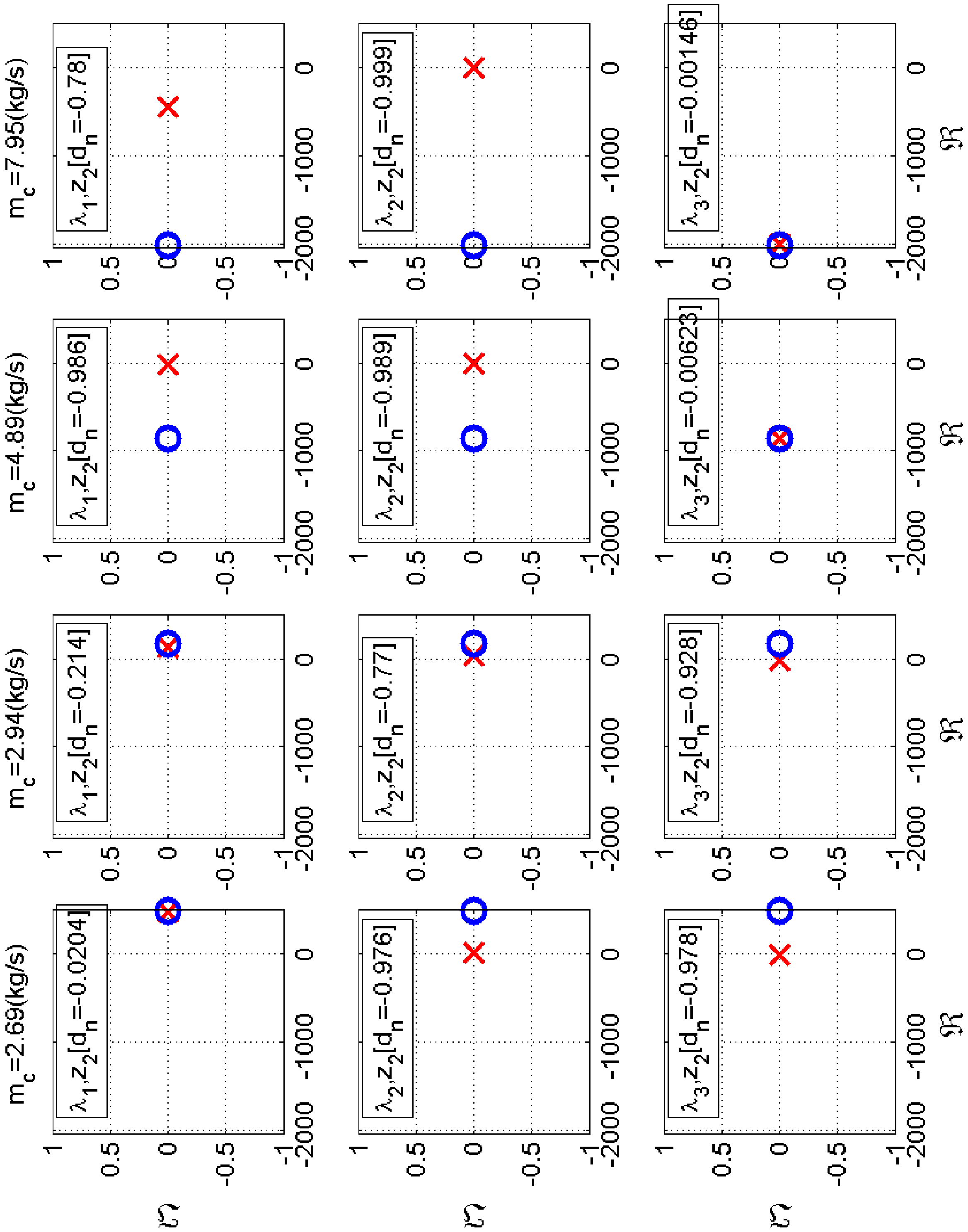

Figure D.2: Normalized distances pole1,pole2,pole3 and zero2

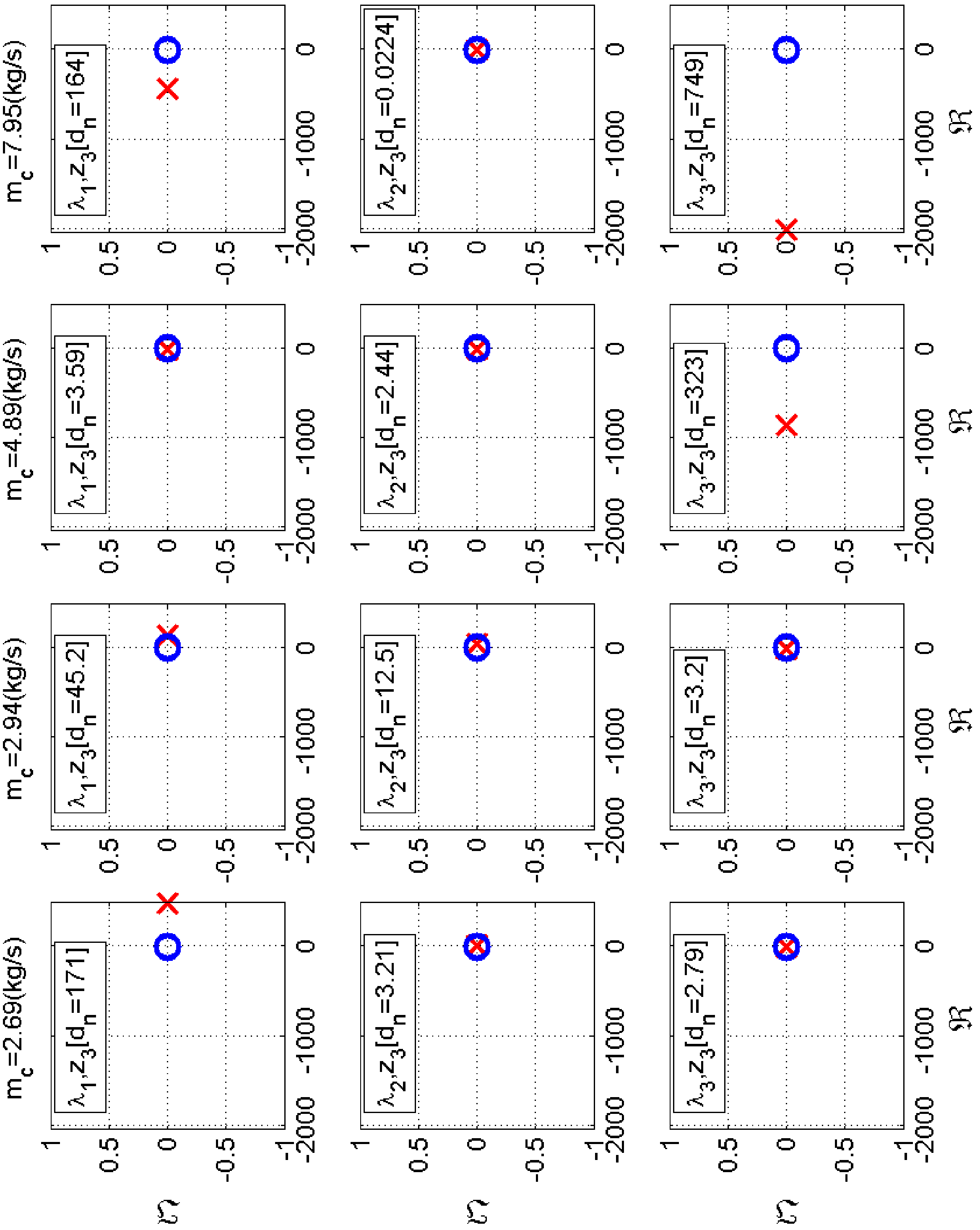

Figure D.3: Normalized distances pole1,pole2,pole3 and zero3

Appendix E

Model validation

In this appendix some data of simulations and experiments (2,3 and 4) as described in Chapter 4 are presented.

E.1 Simulation and experiment 2

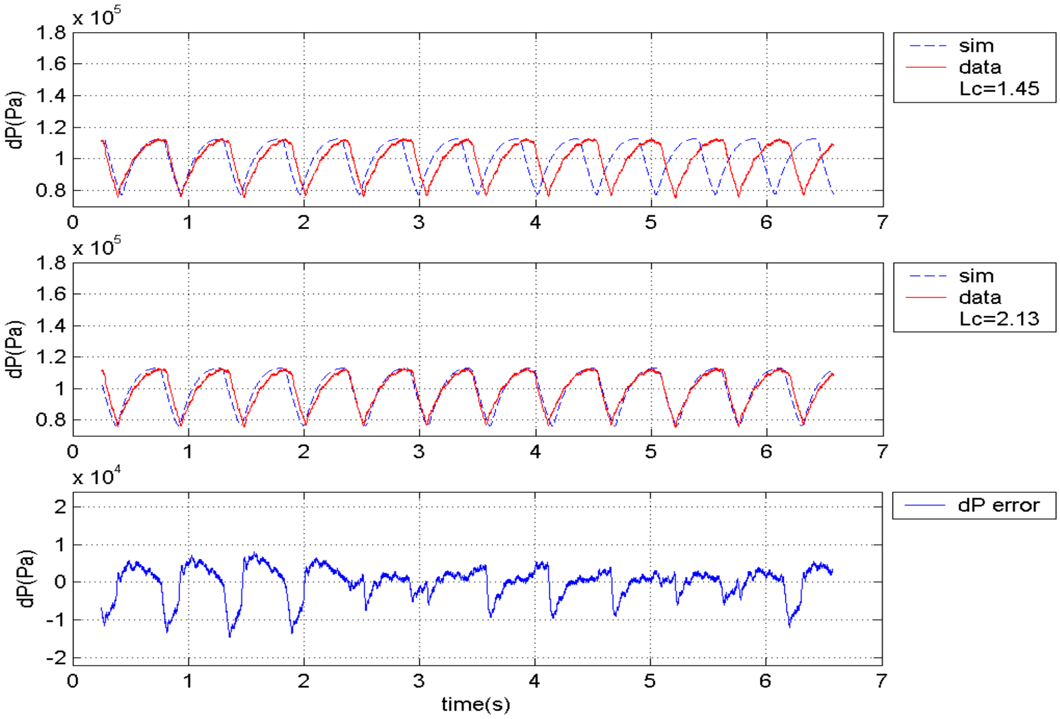

Figure E.1: Simulated and experimental results, experiment 2

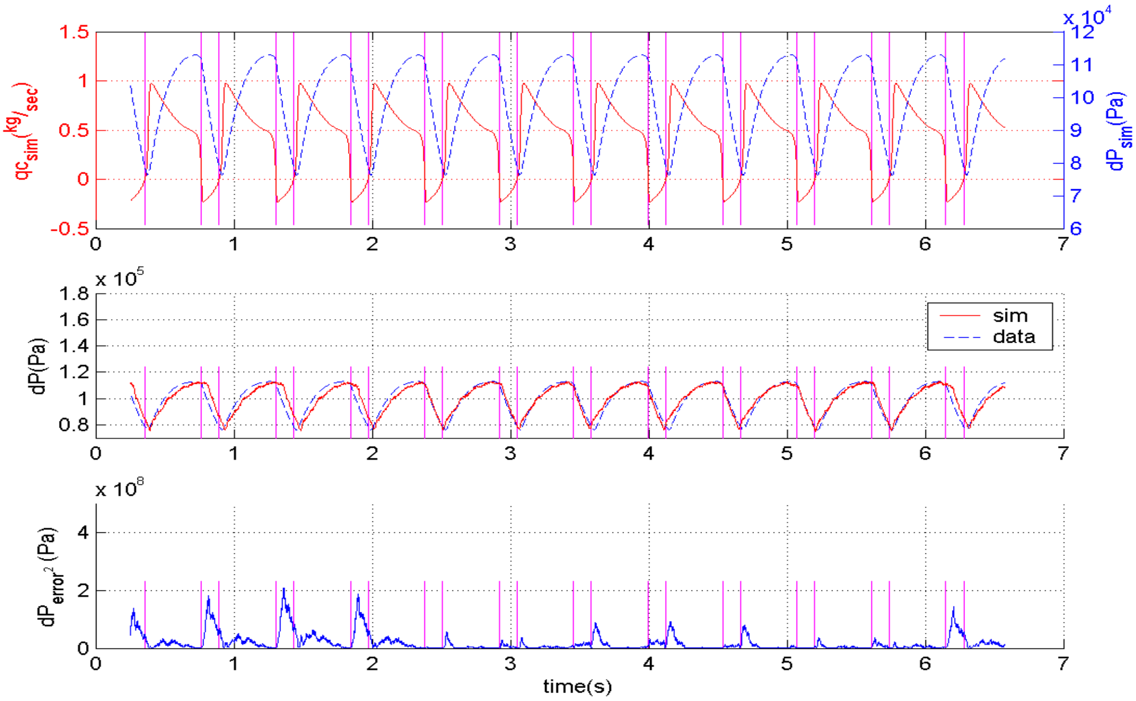

Figure E.2: Simulated and experimental results ($L_c = 2.134$)

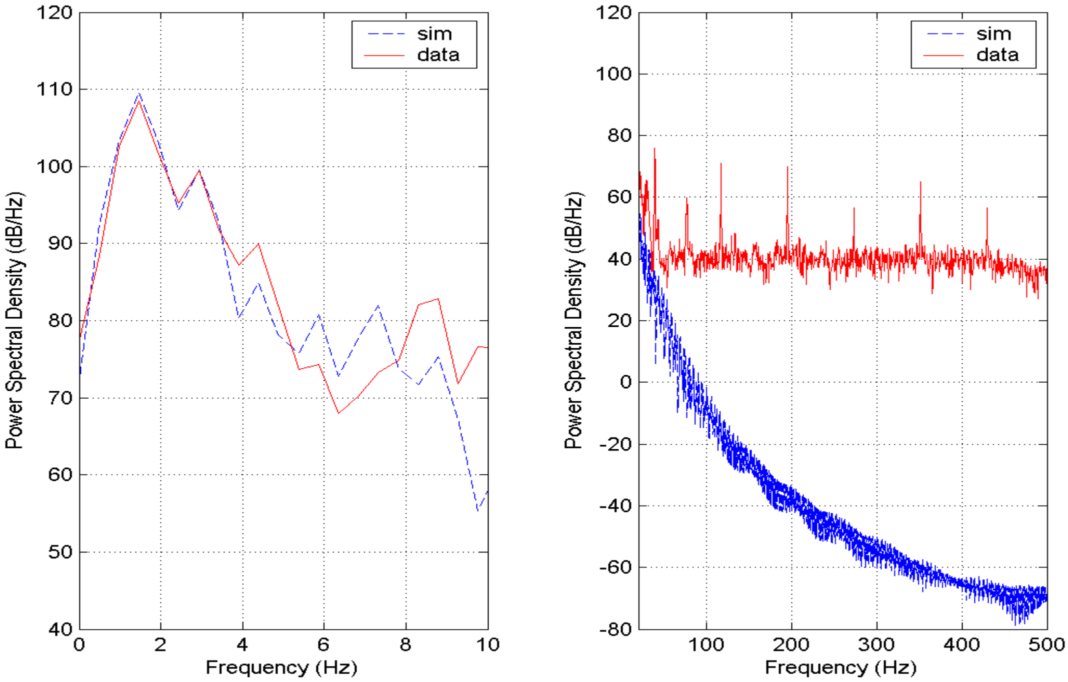

Figure E.3: Power Spectrum analysis, experiment 2

E.2 Simulation and experiment 3

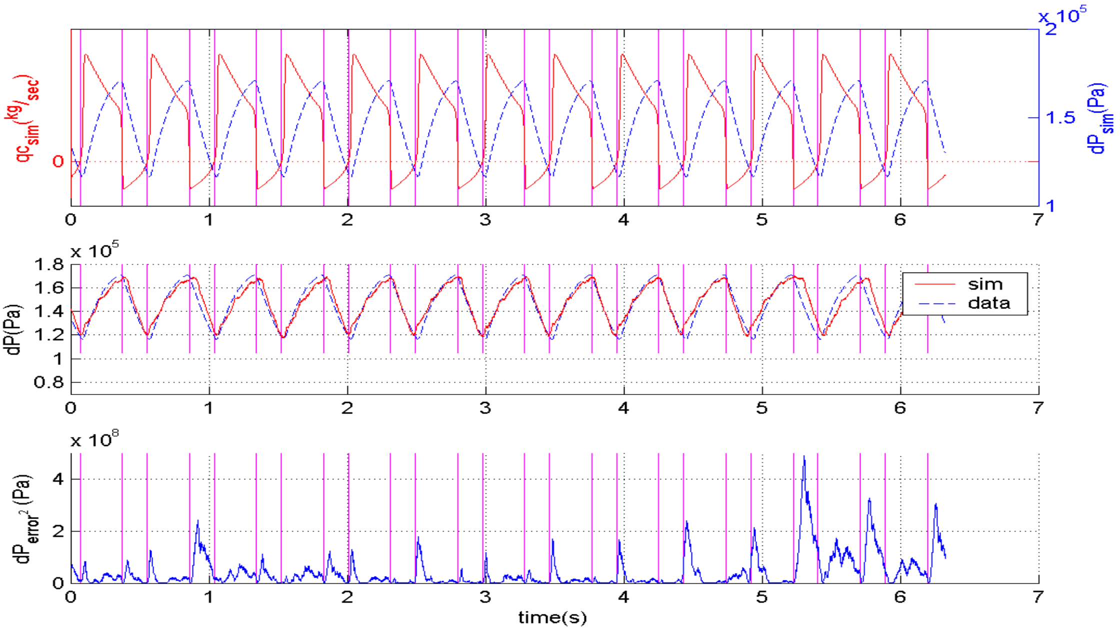

Figure E.4: Simulated and experimental results ($L_c = 1.755$)

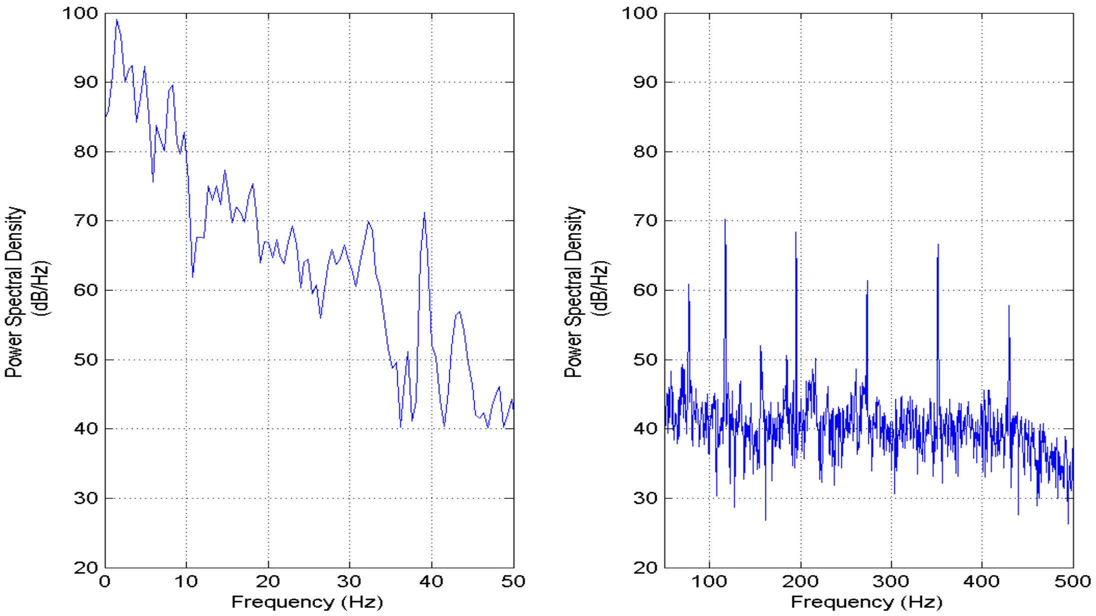

Figure E.5: Residu Power Spectrum analysis, experiment 3

E.3 Simulation and experiment 4

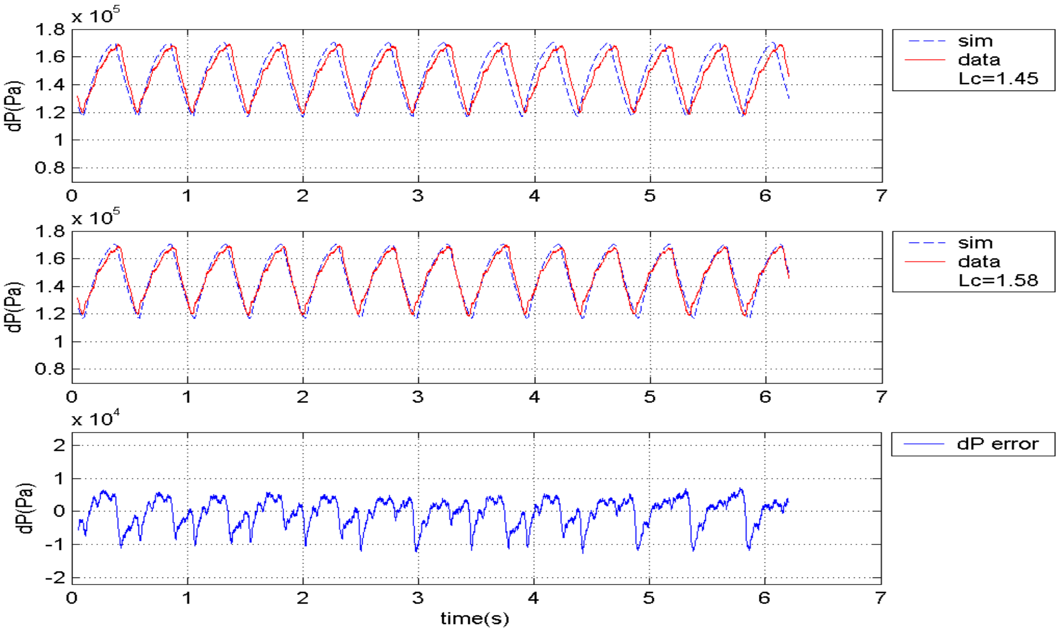

Figure E.6: Simulated and experimental results, experiment 4

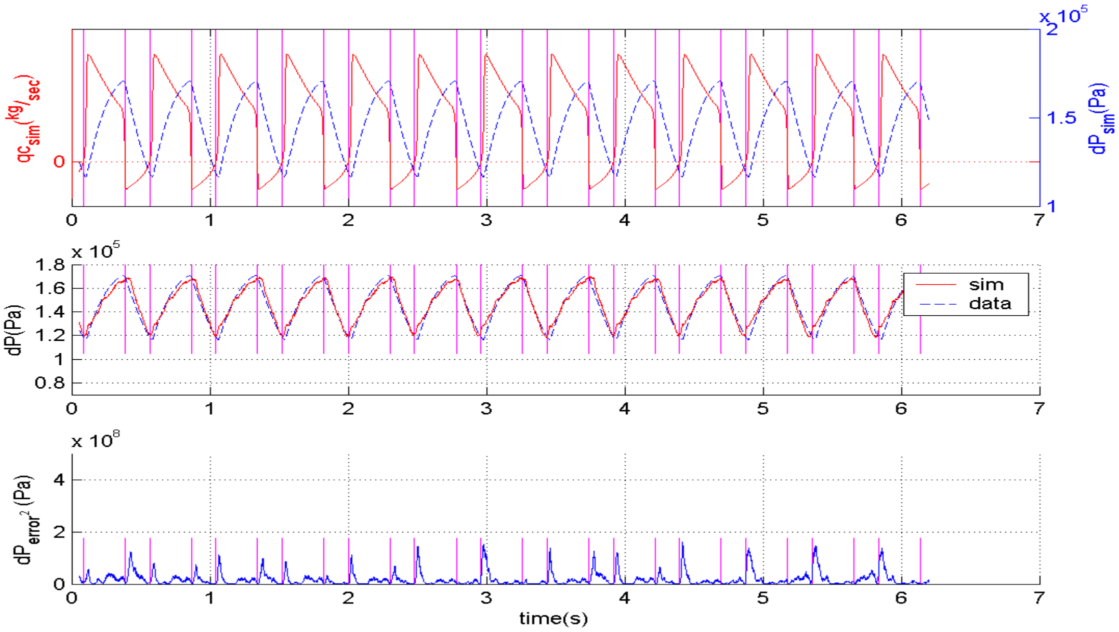

Figure E.7: Simulated and experimental results ($L_c = 1.585$)

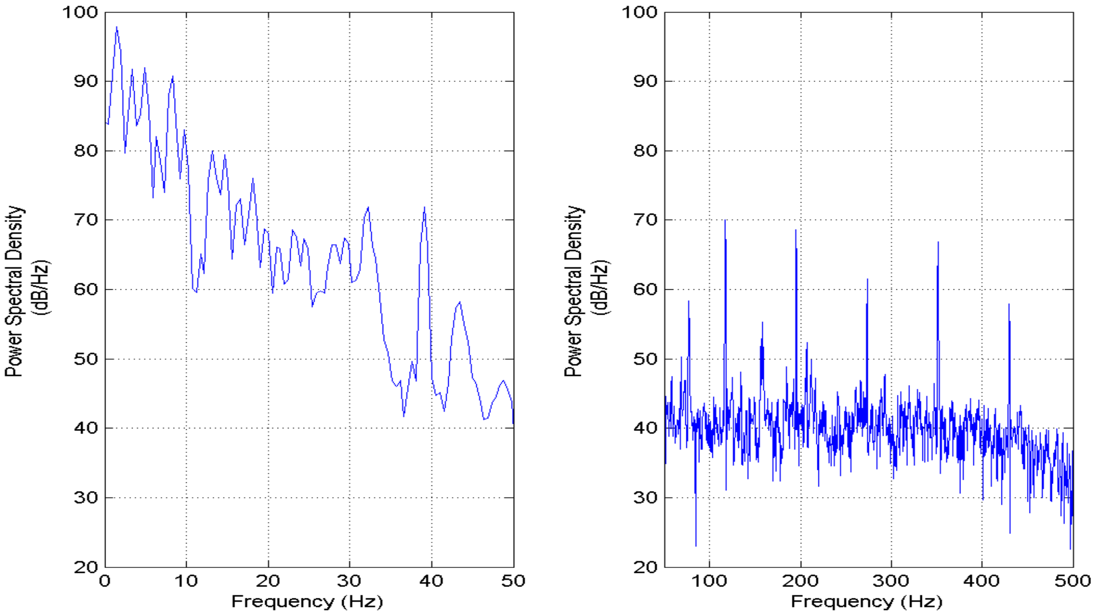

Figure E.8: Residu Power Spectrum analysis, experiment 4

Samenvatting

Het werkgebied van de centrifugaal compressor is gelimiteerd door the aërodynamische stroming instabiliteiten rotation stall en surge, beide instabiliteiten kunnen schade aan de compressor veroorzaken (door mechanische en thermische belastingen). Voor het ontwerp van active surge control strategieën is het wenselijk om een adequaat model te hebben van het dynamisch gedrag van de compressor. Het doel van dit project was het onderzoeken welk model het meest geschikt was voor het beschrijven van de compressor dynamica die relevant is voor active surge control.

In deze scriptie wordt vooral gekeken naar surge en meer specifiek naar het voorkomen van surge door middel van active surge control. Een aantal surge control technieken in de literatuur worden besproken. De conclusie van het literatuuronderzoek is dat voor het ontwerpen van active surge control strategieën het wenselijk is om een adequaat model te hebben van het dynamische gedrag van het compressie systeem. Het doel van dit project was om te onderzoeken welk model het meest geschikt was voor het beschrijven van deze dynamica van een centrifugaal compressie systeem die relevant zijn voor active surge control.

Een kort overzicht is gegeven van de beschikbare compressor modellen en vier compressor modellen zijn nader bekeken. De vier compressor modellen van welke de verschillende aannamen, voor-, en nadelen zijn besproken zijn: het Greitzer model, het extended Greitzer model opgesteld door Meuleman en de modellen opgesteld door Spakovszky (Spakovszky model I and Spakovszky model II). Uiteindelijk word een onderbouwde keus gegeven voor het verder onderzoeken van het Greitzer model en het extended Greitzer model.

Vervolgens is de analyze van de numerieke modellen opgesplitst in een analyze van het Greitzer model en een analyze van het extended Greitzer model. Beide model analyzes startten met een werkpunt analyze: het werkpunt is veranderd om eigenwaarde veranderingen te observeren van het gelineariseerde model. De werkpunt analyze wordt gevolgd door een eigenwaarde analyze waarin wordt gekeken naar bepaalde eigenschappen van eigenwaarden (stabiel/instabiel, reëel/complex). De eigenwaarde analyze verschilt per model: voor het Greitzer model is een analytische eigenwaarde analyze gedaan terwijl voor het extended Greitzer model een numerieke eigenwaarde analyze gedaan is. Om te kijken wat de invloed is van model parameters op de eigenwaarden zijn model specifiek parameters (Greitzer: ratio $\frac{A_c}{L_c}$, extended Greitzer: γ) veranderd. uiteindelijk is gekeken naar de genormaliseerde afstand tussen de pool (polen) en nulpunt(en). Op basis van de model aannamen en de normalized distances voor het extended Greitzer model is geconcludeerd dat het extended Greitzer model geen verbetering is voor compressor modelvorming, in vergelijk met het Greitzer model.

Om de conclusies van het eigenwaarde en het parameter onderzoek te ondersteunen is het Greitzer model gevalideerd met gemeten data van een experimentele opstelling. De totale overeenkomst van het Greitzer model met de gemeten data is goed maar er waren enige opmerkelijke verschillen te zien, in het bijzonder voor en na de punten van omkeer van stroming. Ondanks de geobserveerde verschillen is het Greitzer model bruikbaar voor het beschrijven van het totaal gedrag van de compressor. Daarom is, op basis van alle onderzoeksresultaten, geconcludeerd dat het onderzochte Greitzer model het meest geschikt is voor de relevante dynamica van een centrifugaal compressie systeem.

Dankwoord

Bij deze wil ik graag iedereen bedanken voor de hulp bij mijn afstuderen, maar in het bijzonder de volgende personen.

Mijn ouders die de eerste (en laatste) docenten zijn waar ik ooit onderricht van heb genoten en hun steun op een diversiteit aan vlakken tijdens mijn leven en tijdens deze en andere opleidingen. Tevens maak ik van de gelegenheid gebruik om mijn tweelingbroer en broer te bedanken voor hun γ-visie op de β-wereld. Verder wil ik graag mijn vriendin bedanken voor de steun die zij mij gaf tijdens de minder makkelijke perioden van mijn opleiding en afstuderen.

Op het professionele vlak wil ik graag mijn begeleider, Jan van Helvoirt, bedanken voor de duidelijke en gestructureerde begeleiding. Vervolgens wil ik ook vermelden dat, ondanks het feit dat Huub Giesen geen actieve participatie in mijn afstuderen heeft gehad, hij een aanzienlijke bijdrage heeft geleverd voor mij persoonlijk en voor een aantal collega studenten.
Tevens wil ik van deze gelegenheid gebruik maken om mijn kamergenoten en ex-kamergenoten te bedanken voor de nodige hulp tijdens het afstuderen maar ook zeker voor de broodnodige afleiding.

Bedankt ook Hermes Groep NV en de Gemeente Roermond voor de financiële steun tijdens mijn opleiding en afstuderen in de vorm van leuke part-time banen waarbij ik de sores van de TU/e even kon relativeren.

Ondanks een moeizame start met organisatorische tegenwerking, heb ik toch de studie met voldoening afgerond. Naar men zegt heeft de TU/e mij een stuk basiskennis verschaft voor de rest van mijn (werkzame) leven, doch was het niet de Duitse filosoof Arthur Schopenhauer die zei:

"KENNIS IS NOG GEEN WIJSHEID."

Na alle opleidingen in mijn leven kan ik mijzelf niet geheel onttrekken aan het idee dat ik de wijsheid nog niet in pacht heb. Dit kan onderbouwd worden door een duaal argument, ten eerste is het uitermate arrogant om dergelijke gedachten uit te spreken en getuigt dit van een egocentrische persoonlijkheid, ten tweede is er het gevoel dat mijn educatie nog niet ten einde is. Een spreekwoordelijke mijlpaal in mijn leven is bereikt en wederom schrijdt de levensloop voort in al haar onzekerheden.